Iowa State University
Digital Repository

Retrospective Theses and Dissertations

Iowa State University Capstones, Theses and Dissertations

2008

# Mechanics of wire saw machining process: experimental analyses and modeling

Egemen Teomete
*Iowa State University*

Follow this and additional works at: https://lib.dr.iastate.edu/rtd

Part of the Mechanical Engineering Commons

## Recommended Citation

Teomete, Egemen, "Mechanics of wire saw machining process: experimental analyses and modeling" (2008). *Retrospective Theses and Dissertations*. 15818.
https://lib.dr.iastate.edu/rtd/15818

This Dissertation is brought to you for free and open access by the Iowa State University Capstones, Theses and Dissertations at Iowa State University Digital Repository. It has been accepted for inclusion in Retrospective Theses and Dissertations by an authorized administrator of Iowa State University Digital Repository. For more information, please contact digirep@iastate.edu.

**Mechanics of wire saw machining process: Experimental analyses and modeling**

by

**Egemen Teomete**

A dissertation submitted to the graduate faculty

in partial fulfillment of the requirements for the degree of

DOCTOR OF PHILOSOPHY

Major: Engineering Mechanics

Program of Study Committee:
Ashraf Bastawros, Co-Major Professor
Abhijit Chandra, Co-Major Professor
Ersan Ustundag
Thomas Rudolphi
Pranav Shrotriya

Iowa State University

Ames, Iowa

2008

Copyright © Egemen Teomete, 2008. All rights reserved.

UMI Number: 3316174

INFORMATION TO USERS

The quality of this reproduction is dependent upon the quality of the copy submitted. Broken or indistinct print, colored or poor quality illustrations and photographs, print bleed-through, substandard margins, and improper alignment can adversely affect reproduction.

In the unlikely event that the author did not send a complete manuscript and there are missing pages, these will be noted. Also, if unauthorized copyright material had to be removed, a note will indicate the deletion.

UMI Microform 3316174
Copyright 2008 by ProQuest LLC
All rights reserved. This microform edition is protected against unauthorized copying under Title 17, United States Code.

ProQuest LLC
789 East Eisenhower Parkway
P.O. Box 1346
Ann Arbor, MI 48106-1346

***To my wife Eda, for her love, patience and encouragements…***

# TABLE OF CONTENTS

LIST OF FIGURES vii

LIST OF TABLES xii

ACKNOWLEDGEMENTS xiii

ABSTRACT xv

CHAPTER 1. INTRODUCTION AND LITERATURE REVIEW 1

1.1. Literature Review on Wire Saw Process 2

1.1.1. Material Removal Models 3

1.1.2. Wire Vibration 5

1.1.3. Parametric Studies on Wire Saw Process 7

1.1.4. Other Research Work on Wire Saw Process 9

1.2. Damage Models for Brittle Materials 12

1.3. The Machining of Brittle Materials 17

1.4. Ductile Mode Material Removal and Wear Models 19

1.5. Motivation and Proposed Work 21

1.6. Dissertation Organization 23

1.7. References 23

CHAPTER 2. EXPERIMENTAL PROCEDURE AND PRELIMINARY RESULTS 33

2.1. Wire Saw Process, Wire Speed and Feed Speed Measurements 33

2.2. Diamond Grit Coated Steel Wires 34

2.3. Wire Bow Angle Measurements 35

2.4. Dynamic Force Measurements 35

2.4.1. Calibration of Load Cell Setup 36

2.5. Surface Roughness Measurements and SEM Imaging 38

2.6. Sample Preparation 38

2.7. Preliminary Results 39

2.7.1. The Effect of Wire Speed 39

2.7.2. The Effect of Feed Speed 40

2.7.3. The Effect of Wire Tension 40

2.7.4. The SEM Imaging Results 40

2.8. References 40

CHAPTER 3. ROUGHNESS AND DAMAGE EVOLUTION DUE TO WIRE SAW PROCESS 55

3.1. Introduction 55

3.2. Experimental Process 58

3.2.1. Wire Saw Cutting and Wire Bow Angle Measurement 58

3.2.2. Surface Roughness Measurements and SEM imaging 60

3.3. Roughness Model Derivation 61

3.4. Results and Discussion 63

3.5. Conclusion 65

3.6. Acknowledgement 65

3.7. References 65

CHAPTER 4. WIRE SAW PROCESS INDUCED LONG WAVINESS INVESTIGATION 75

4.1. Introduction 75

4.2. Experimental Design 77

4.2.1 Wire Saw Process and Wire Bow Angle Measurement 77

4.2.2. Surface Waviness Measurements 78

4.3. Wire Saw Process Induced Waviness Model 78

4.3.1. The String Deflection Model 79

4.3.2. The Lateral Deflection Model in (X-Y) Plane 81

4.3.2.1. The Energy Terms for Surface Waviness Generation 82

4.3.2.1.1. Work Done by Free Standing Wire 82

4.3.2.1.2. Work Done by Oblique Cutting Forces 82

4.3.2.1.3. Work Done by Wire Tension 83

4.3.2.2. The Mechanisms Effecting Long Waviness 83

4.3.2.2.1. Mechanism 1 84

4.3.2.2.2. Mechanism 2 84

4.4. Results and Discussion 85

4.5. Conclusion 87

4.6. Acknowledgement 88

4.7. References 88

CHAPTER 5. WIRE SAW CUTTING INDUCED SURFACE DAMAGE AND DESIGN SPACE EXPLORATION 102

5.1. Wire Saw Process Induced Surface Damage Depth Investigation 102

5.1.1. Experimental Setup 103

5.1.2. Results and Discussion 104

5.1.2.1. Variation of the Intrinsic Process Parameters 104

5.1.2.2. Variation of the Surface Damage Depth 104

5.1.3. General Trend 105

5.2. Design Space Exploration 106

5.3. References 107

CHAPTER 6. CONCLUSIONS and FUTURE WORK 118

6.1 Conclusions 118

6.2. Future Work 120

## LIST OF FIGURES

Fig. 1.1. Industrial wire saw process (Bhagavat et al. 2000). 29

Fig. 1.2. Rolling indenting material removal in wire saw process (Bhagavat et al. 2000). 29

Fig. 1.3. Free abrasive wire saw process a) The slurry pressure profile b) Slurry film thickness profile (Bhagavat et al. 2000). 30

Fig. 1.4. Surfaces of a) Wire saw sliced wafer with free abrasive machining b) Polished wafer (Bhagavat et al.2000). 30

Fig. 1.5. Indentation damage in brittle materials. 31

Fig. 1.6. Indentation cracks in brittle materials A) Cone crack, B) Radial crack, C) Median crack, D) Half- penny crack E) Lateral crack (Cook and Pharr 1990). 31

Fig. 1.7. Damage due to scratching of brittle materials (Ahn et al.1998). 32

Fig. 2.1. Single wire, spool-to-spool wire saw machine (DWT Inc., Millennium Model). The wire track is marked by the dashed line. 42

Fig. 2.2. SEM images of diamond impregnated wires a) DWS2 old wire b) DWS3 from Well Inc. c) DWS4 from Saint-Gobain Abrasives Inc. d) DWS5 from Saint-Gobain Abrasives Inc. 43

Fig. 2.3. Cross section of a typical diamond impregnated wire [1]. 43

Fig. 2.4. Optical image showing the wire inclination angle with the cutting direction at the entrance and exit from the specimen. 44

Fig. 2.5. Wire bow angle and wire curvature. 44

Fig. 2.6. Dynamic load cell configuration. 45

Fig. 2.7. Load cell calibration for the cross sensitivity matrix coefficients Szz and Szx. 45

Fig. 2.8. Load cell calibration for the cross sensitivity matrix coefficients Sxx and Sxz. 46

Fig. 2.9. Sample anchoring for a waviness test setup. 46

Fig. 2.10. Surface profile measurements of wire saw induced waviness. 47

Fig. 2.11. 3D surface reconstruction showing wire saw induced roughness as measured by surface profilometer ($Vx$ =2m/s, $Vz$= 6.4 μm/sec, $T$=26.7 N). 47

Fig. 2.12. Variation of wire bow angle per unit cut length *α/Lo* as a function of wire speed *Vx* (*Vz*= 5 µm/sec, *T*=13 N). 48
Fig. 2.13. Variation of distributed load, *w* as a function of *Vx* (*Vz*= 5 µm/sec, *T*=13 N). 48
Fig. 2.14. Variation of surface roughness as a function of wire speed *Vx* (*Vz*= 5 µm/sec, *T*=13N). 49
Fig. 2.15. Variation of wire bow angle per unit cut length *α/Lo* as a function of feed speed *Vz* (*Vx* =1.8 m/sec, *T*=13 N). 49
Fig. 2.16. Variation of distributed load *w* as a function of feed speed *Vz* (*Vx* =1.8 m/sec, *T*=13N). 50
Fig. 2.17. Variation of surface roughness as a function of feed speed *Vz* (*Vx* =1.8 m/sec, *T*=13N). 50
Fig. 2.18. Variation of wire bow angle per unit cut length *α/Lo* as a function of wire tension *T* (*Vx*=1.8 m/sec, *Vz*= 5 µm/sec). 51
Fig. 2.19. Variation of distributed load *w* as a function of wire tension *T* (*Vx*=1.8 m/sec, *Vz*= 5 µm/sec). 51
Fig. 2.20. Variation of surface roughness as a function of wire tension *T* (*Vx*=1.8 m/sec, *Vz*= 5 µm/sec). 52
Fig. 2.21. The SEM image of a cut surface (*Vx*=1.3 m/sec, *Vz*= 5 µm/sec, *T*=13 N). 52
Fig. 3.1. Single wire, spool-to-spool wire saw machine (DWT Inc., Millennium Model). The wire track is marked by the dashed line. 68
Fig. 3.2. SEM images of diamond impregnated wires a) DWS2 old wire b) DWS3 from Well Inc. c) DWS4 from Saint-Gobain Abrasives Inc. d) DWS5 from Saint-Gobain Abrasives Inc. 69
Fig. 3.3. Wire bow angle and wire curvature in wire saw tests. 69
Fig. 3.4. The SEM image of a wire saw cut surface (*Vx*=1.3 m/sec, *Vz*= 5 µm/sec, *T*=13 N). 70
Fig. 3.5. Wire saw roughness damage model showing ductile material removal and brittle fracture. 70

Fig. 3.6. Comparison of wire saw roughness damage models
with respect to experimental results. 71
Fig. 3.7. The variation of wire bow angle per unit cut length
$\alpha/Lo$ as a function of wire tension $T$ ($Vx$=1.8 m/sec, $Vz$= 5 μm/sec). 71
Fig. 3.8. The variation of distributed load $w$ as a function of wire tension $T$
($Vx$=1.8 m/sec, $Vz$= 5 μm/sec). 72
Fig. 3.9. The variation of surface roughness as a function of wire tension $T$
($Vx$=1.8 m/sec, $Vz$= 5 μm/sec). 72
Fig. 3.10. The variation of surface roughness as a function of $Vx$
($Vz$= 6.35 μm/sec, T=13N). The tests are done with different wires. 73
Fig. 4.1. Single wire, spool-to-spool wire saw machine
(DWT Inc., Millennium Model) used in waviness tests.
The wire track is marked by the dashed line. 90
Fig. 4.2. SEM images of diamond impregnated wire. 91
Fig. 4.3. Optical image showing the wire inclination angle with the
cutting direction at the entrance and exit from the specimen for a waviness test. 91
Fig. 4.4. Wire marks on a wire saw cut surface
(TC22 Vx=2 m/s, Vz=12.7 μm/s, T=26.7 N). 92
Fig. 4.5. The coordinate system defined for analyses of wire saw process. 92
Fig. 4.6. The model of a wire under tension and distributed load. 93
Fig. 4.7. The forces acting on an infinitesimal string element. 93
Fig. 4.8. Variation of lateral reaction with cut depth. 94
Fig. 4.9. Mechanism 1 energy plots. 94
Fig. 4.10. Surface profile due to mechanism 1. 95
Fig. 4.11. Mechanism 2 energy plots. 95
Fig. 4.12. Surface profile due to mechanism 2. 96
Fig. 4.13. Variation of wire bow as a function of wire tension and
feed speed in cut plane XZ. 96
Fig. 4.14. Surface long waviness profile of TC20 test. 97
Fig. 4.15. Surface long waviness profile of TC21 test. 97

Fig. 4.16. Surface long waviness profile of TC22 test. 98
Fig. 4.17. Energy plots of TC20 test. 98
Fig. 4.18. Energy plots of TC21 test. 99
Fig. 4.19. Energy plots of TC22 test. 99
Fig. 4.20. Domains for long waviness mechanisms. 100
Fig. 5.1. Bonded-interface section wire saw test setup. 108
Fig. 5.2. Bonded-interface section test samples coated with gold sputtering for SEM imaging. 108
Fig. 5.3. SEM image showing surface damage depth of bonded-interface section (BIS) wire saw test (*Vx* = 2 m/s, *Vz*= 6.4 µm/sec, *T*=18 N). 109
Fig. 5.4. Variation of wire (a) bow angle (*α/Lo*) and (b) wire loading *w,* as a function of wire speed *Vx* for BIS tests (*Vz*= 6.4 µm/sec, *T*=13 N). 110
Fig. 5.5. Variation of wire (a) bow angle (*α/Lo*) and (b) wire loading *w,* as a function of feed speed *Vz* for BIS tests (*Vx*= 2 m/sec, *T*=13 N). 111
Fig. 5.6. Variation of wire (a) bow angle (*α/Lo*) and (b) wire loading *w,* as a function of wire tension *T* for BIS tests (*Vx*= 2 m/sec, *Vz*= 6.4 µm/sec). 112
Fig. 5.7. Variation of surface damage depth $D_d$ as a function of wire speed *Vx* for BIS tests (*Vz*= 6.4 µm/sec, *T*=13 N). 113
Fig. 5.8. The surface damage depth $D_d$ as a function of feed speed *Vz* for BIS tests (*Vx*= 2 m/sec, *T*=13 N). 113
Fig. 5.9. Variation of surface damage depth $D_d$ as a function of wire tension *T* for BIS tests (*Vx*= 2 m/sec, *Vz*= 6.4 µm/sec). 114
Fig. 5.10. The variation of damage index $I_d$ as a function of *Vz/Vx* for BIS tests (T= 13 N). 114
Fig. 5.11. The variation of surface roughness as a function of feed speed to wire speed ratio. 115
Fig. 5.12. The variation of long waviness amplitude as a function of feed speed and wire tension. 115

Fig. 5.13. Design space for wire saw process: Effects of wire speed, feed speed and wire tension on surface roughness *Ra*, surface damage depth $D_d$ and long waviness amplitude *A*. 116

# LIST OF TABLES

Table 2.1. Diamond impregnated wire properties. 53

Table 2.2. The cross calibration $S_{xx}$ and $S_{xz}$ values. 54

Table 3.1. Diamond wire properties. 73

Table 4.1. The long waviness experiments parameters. 101

Table 5.1. Bonded-interface section wire saw tests parameters and measured surface damage depth. 117

## ACKNOWLEDGEMENTS

This work is achieved by the support of Iowa State University, Aerospace Engineering Department and the NSF through grant No.DMII-0355536.

I am grateful to my major professor, Dr. Ashraf Bastawros for his endless support during my studies. We had fruitful discussions which taught me how to do research. His advisory on my experimental work has been invaluable, teaching me how to design experiments, controlling the parameters, identifying the key issues, obtaining the results and analyzing them to get a conclusion. It has been a great experience working with him in the lab that taught me how to use simple objects to put up a totally new experimental setup. I am delighted with his enthusiasm and excitement in experimental work which I wish to have during the rest of my life. I have taken courses from Dr. Bastawros including Dislocation Mechanics, Plasticity, Fracture and Fatigue. In all of these fundamental courses and in the discussions during research, Dr. Bastawros opened a whole new world of mechanics of materials in front of me. He taught me how to solve an engineering problem starting from basic principles of mechanics, identifying fundamentals and constructing a new phenomenological model. Dr. Bastawros has always been concerned with our well being in our academic and private life, giving invaluable advices on life. He has been more than an academic advisor. I wish to carry his enthusiasm and excitement in research work to future generations. I hope I will have the chance to repay him all the values he has added to my life.

I am grateful to Dr. Abhijit Chandra for his efforts in teaching me a whole new world, machining and process engineering. We had invaluable discussions during the research and courses that taught me the principles of machining. Our discussions on applying solid mechanics on modeling machining processes opened my mind, while teaching me how to solve a specific problem in process engineering. We had great many discussions during the research that has splendid contributions in my modeling efforts. Dr. Chandra gave me his invaluable journal papers which I discovered ways to many aspects of my current work. I have taken three courses from Dr. Chandra on process engineering which covered many aspects of machining and contributed a new research area in my future life. Dr. Chandra has been beyond an academic advisor, caring my well being in my marriage and private life and

in reaching my future career goals. I wish I will have the chance to repay him all the goodness he had done.

I wish to thank to Dr. Ersan Ustundag for his advisory in our discussions during the course Mechanical Behavior of Materials. Dr. Ustundag introduced mechanics of various materials and models during this fundamental course. I am grateful to him for his efforts in editing my thesis and giving advices how to proceed in my work.

I would like to thank Dr. Thomas Rudolphi for his great contributions to my education during the Continuum Mechanics and Finite Elements courses. We had great many discussions during the course work that enlightened my view. I am grateful for his revising this dissertation.

I would like to thank to Dr. Pranav Shrotriya for revising my thesis.

The helps of Thomas Elliott and Kevin Brownfield during my experimental work are unforgettable.

I would like to thank to my friends in the micromechanics group for their support and discussions that gave me courage and strength. I am also grateful to my many friends in Ames that made life lovelier.

I am grateful to my parents Nermin and Erdogan Teomete and my brothers Uygar and Baris for their love, encouragements and support for whole my life.

I am grateful to my wife, Eda Teomete for her love, patience, understanding, encouragements and endless supports during my studies.

# ABSTRACT

The silicon wafers in the photovoltaic and microelectronics industries are sliced using the wire saw process. The process has a higher yield, lower kerf loss, and lower surface damage with respect to inner diameter saw. Higher diameter and thinner wafers can be obtained using the wire saw process. Almost all kinds of brittle materials, including high density or foam ceramics, glasses, sapphire, and rocks, can be cut by wire saw.

The early slurry-based wire saw process consisted of a bare steel wire and abrasive carrying slurry, which leads to a rolling and indenting materials removal mechanism. Fixed-abrasive wire saw process, consisting of diamond grit impregnated steel wire leads to fixed-abrasive machining, was developed. The fixed-abrasive wire saw process is more efficient in comparison to the slurry-based wire saw process. The fixed-abrasive wire saw process is the subject of this study and is referred to as “the wire saw process” hereafter.

Although it offers many advantages, the wire-saw process induces roughness and waviness damages on the cut surface. Post processes including grinding and polishing are used to remove these damages, which increases manufacturing costs. Roughness and waviness damage models relating the process parameters to the damage are needed to minimize the damage. The scope of this work is to develop roughness and waviness damage models that relate the process parameters to these damages.

An experimental parametric study is conducted for surface roughness, varying the feed speed, wire speed, wire tension, and wire properties using different wires. The parametric study shows that the surface roughness decreases with wire speed, increases with feed speed, and is independent of wire tension. The SEM images of the cut surface reveal that the material removal is in ductile mode while there is brittle fracture in the form of grain removal, which leads to roughness damage. The material removal mechanism is the same as the ductile-regime machining of brittle materials reported in the literature.

Stress based and fracture mechanics based damage models are derived for roughness damage induced by wire saw cutting. The models have a good performance in predicting the roughness damage obtained from experimental work. Both models show that if the feed

speed-to-wire speed ratio increases, roughness will increase, while if this ratio is kept constant, the roughness will be constant. In order to increase the efficiency of the wire saw process by increasing feed speed, the wire speed should be increased proportionally to the feed speed so that the roughness will be kept constant.

Both of the roughness models state that if abrasive grit radius and spacing increases, roughness damage will increase. An experimental parametric study including tests done with three different wires is conducted. The parametric study shows that the roughness damage increases with increasing grit radius and spacing. Wires having high grit density and smaller grits are beneficial for surface quality.

The amount of material that has to be removed by post processes is governed by the surface-damage depth. The bonded-interface sectioning technique (BIS) is employed with wire saw tests. An experimental parametric study relating process parameters to surface damage depth is conducted. The surface-damage depth is measured using SEM imaging. The SEM images show that the surface damage is occurring due to grain removal by brittle fracture. The fracture-damage model captures the variation of surface-damage depth well. The surface-damage depth increases with increasing ratio of feed speed to wire speed. The average surface damage depth is 15 μm. An average depth of 15 μm should be removed in order to remove the process-induced damage totally.

Long waviness induced by the wire-saw process is the most detrimental surface damage. Long waviness formation is investigated by experimental parametric study and analytical modeling. A string model is used to model the bow of the wire marks on the cut surface. The string model is capable of predicting the bow of the wire marks obtained by experimental study. The increase of tension decreases the wire bow amplitude, while increase in feed speed increases the wire bow amplitude, which is predicted by the string model and observed in the experiments.

The work done by free-standing wire, work done by oblique cutting forces and work done by wire tension on the wire, governs the long waviness formation. The equivalence of these energetic terms leads to two mechanisms. These mechanisms are used to explain the

evolution of the long waviness profile and peak-to-valley value with respect to process parameters. The increase of wire tension leads to a wavy surface with a lower peak-to-valley value, while decreasing wire tension will lead to a step like surface with a high peak-to-valley value. The peak-to-valley value increases with increasing feed speed. The amount of post processes increases with an increasing peak-to-valley value, which will increase costs. In order to increase the efficiency without increasing the peak-to-valley value, the wire tension can be increased with increasing feed speed.

# CHAPTER 1. INTRODUCTION AND LITERATURE REVIEW

Machining of brittle single crystals has gained serious attention to minimize subsurface machining induced damage to improve reliability as well as reduction of kerf loss and wasted scraps. The wide utilization of silicon wafers in photovoltaic solar cell and in microelectronics industries requires parallel processes for the wafer cutting process. Commonly, inner diameter (ID) saws and parallel wire saws are utilized in the wafer cutting process. Wire saws enjoy several advantages over ID saws. These advantages include higher productivity, less wafer-surface damage, and lower kerf loss (Zhu and Kao 2005). Moreover, there is no limitation on the ingot diameter that can be cut. Recently, wire saws have been used to cut sapphire, silicon carbide, lithium niobate, wood, rock, and almost all kinds of ceramics including foam ceramics (Zhu and Kao 2005; Clark et al. 2003b; Ge et al. 2004). The wire saw process represents 30% of the total silicon wafer production cost, which directly affects the industry. There is a need to optimize the process by developing models relating process parameters to the outputs (Moller 2004).

In multi-wire technology, a single wire is winded to a tension control unit and four (or more) guide pulley webs, grooved with constant pitch. Several hundreds of parallel wires are run together and collected at an up-take spool as seen in Fig. 1.1. A slurry filled with abrasive grits is supplied by a slurry manifold while the wire is oscillating between the supply and take-up spools. The ingot is sliced into hundreds of wafers as it is fed into the wire web. The wafers in the solar cell industry are cut by running the wire in only one direction at a high speed between 5 to 20 m/s, while the wafers in the micro-electronics industry are cut by running the wire in both directions with a lower speed (oscillating the wire from one spool to another). Wafers obtained by oscillating wire have a smoother and more even surface compared to wafers obtained by running the wire in only one direction (Moller 2004).

The early wire saw process for wafer production, developed in the 1990s, consisted of a bare steel wire and abrasive carrying slurry, resulting in free abrasive machining using elasto-hydrodynamic forces (Clark et al. 2003a; Bhagavat et al. 2000). In general, wire speed is between 5 to 15 m/s and wire tension is 20 to 30 N. The feed into the ingot results in a wire bow so that the wire makes $2^o$ to $6^o$ bow angle with the horizontal (Bhagavat et al. 2000).

The abrasive particles can be SiC or diamond. The mean grain size of abrasive particles can be 5 to 30 μm with a 30 to 60% volume fraction in the slurry. Average wire diameter is 180 μm, leading to a kerf loss of 200 to 250 μm (Moller 2004). The bow and tension of the wire are balanced with hydrodynamic pressure of the slurry which is trapped between the wire and work piece. The axial speed of the wire creates a velocity profile in the slurry. The hydrodynamic pressure and velocity profile of the slurry causes the abrasive particles to indent into the work piece and roll, which is called a rolling-indenting process as seen in Fig. 1.2**.** The rolling-indenting material removal mode is also called free abrasive machining (FAM), (Bhagavat et al. 2000)**.** Wafer thicknesses are around 250 and 350 μm while a thickness of 100 μm can be obtained. The slurry can be water-based or oil-based. Oil-based slurry causes the wafers to stick to each other, and it is hard to separate them, while removal of the oil from the wafer surface is another problem. Disposal of the oil-based slurry after use is also a problem. Hydrogen gas is produced due to interaction of water-based slurry and silicon, which may cause an explosion. However, from an environmental point of view, considering the high amount of slurry disposed during the process, water-based slurries can be a choice for the future of the wire saw process (Moller 2004).

In order to increase the productivity and to be able to cut harder ceramics, diamond impregnated wire, which leads to fixed abrasive machining, was developed (Clark et al. 2003a).

Literature on wire saw research has addressed three main topics: material removal mechanisms, kinematics of wire and slurry hydrodynamics, and parametric studies between the process parameters and the quality of the resulting surface. A literature review of wire-saw research is presented in the next section.

### 1.1. Literature Review on the Wire Saw Process

There are several material removal models based on how the abrasive particle interacts with the surface. These models include i) free abrasive machining and ii) fixed abrasive machining. These models are presented in the following section.

### 1.1.1. Material Removal Models

Moller (2004) developed material removal mechanisms for free abrasive machining using fracture mechanics and hydrodynamic behavior of slurry. The contact modes of wire-abrasive grit-work pieces are defined as semi-contact and non-contact case. If the slurry film thickness between the wire and work piece is smaller than the average abrasive grit size, the grit is in contact with both wire and abrasive, which is named the semi-contact case. If the grit is rolling freely between the wire and work piece and in contact only with either wire or work piece at a time, it is called a non-contact case. The material removal correlations for semi-contact and non-contact cases were developed. If the elastic displacement of the wire is significant and slurry viscosity changes are negligible, this regime is defined as isoviscous-elastic regime (IE). If the slurry film thickness is much more than the elastic displacement of the wire, it is called isoviscous-rigid regime (IR). The slurry film thickness and shear stress are defined for both regimes. The increase of abrasive grit size increases the material removal rate (MRR) while also increasing surface roughness of the final product. The grain shape is also important in wire saw MRR. If the grains have a high aspect ratio (elongated grains), they will not rotate in the laminar flow of slurry, which will decrease MRR, while grains having an aspect ratio close to one will rotate more. New grits with sharp corners will increase MRR. The increase of viscosity of slurry due to debris from the work piece may cause agglomeration and reduce MRR. The wire saw process induces a wavy topology on the mm length scale, waviness on the 100 μm length scale, and roughness in the μm length scale. The origin of such large-scale defects, grooves and wavy topology are not yet well understood (Moller 2004).

Bhagavat et al. (2000) defined the material removal rate as a function of the imparted energy to the abrasive by hydrodynamic forces. The hydrodynamic film characteristics are calculated using the finite element method, which couples Reynold's equation of hydrodynamics with the elasticity equation of wire. Such analysis provides the pressure distribution and film thickness profiles of slurry film within the cut trench. For a 100 mm ingot length, the pressure starts from zero at the inlet and gradually increases to a maximum value, where it starts to decrease towards the downstream exit region as seen in Fig. 1.3(a).

The gradual decrease of pressure near the exit is disturbed by a stage in the pressure profile that is due to the continuity of slurry flow. The pressure profile is almost constant in the transverse direction except near the entrance and exits where it decays to zero. The thickness profile of the slurry film shows that the film thickness is large at the inlet, where it starts to decrease gradually towards the exit as seen in Fig. 1.3(b). The high slurry film thickness at the inlet is due to high wire compliance at the inlet, while the low slurry film thickness at the middle is explained due to low wire compliance in this region. The minimum slurry film thickness at the exit is explained by low slurry pressure. The increase of slurry viscosity and wire speed $V_x$ increases the slurry film thickness, while the increase of the wire bow angle decreases the film thickness due to an increase in stiffness of the wire and load on the film. The obtained minimum film thickness for a 50 mm ingot was approximately 130 μm, which is much greater than abrasive grit size. Thus, the mode of cutting is free abrasive machining in which the grits roll and indent the work piece to induce material removal. This is also validated by the microscopic images of a wire saw sliced wafer which has equal-sized pits due to single material removal of floating abrasives as in Fig. 1.4(a). The polished surface of a wafer shows scratches due to direct contact of abrasive pressed by the tool onto ingot as presented in Fig. 1.4(b). Due to the decrease of slurry film thickness towards the exit, the cutting conditions may change for large diameter ingots and poor surface finish occurs. Oscillating wire saw machining is necessary for uniform and efficient cutting of large diameter ingots. The wire saw machining is taking place in a isoviscous-elastic regime (IE). The material removal is proportional to slurry viscosity μ, size of abrasive $D_g$, slurry pressure $p_s$, square of wire speed $V_x$, and inversely proportional to square of slurry thickness $h_s$ as presented in Eq. 1.1 (Bhagavat et al. 2000, Bhagavat and Kao 1999).

$$MRR \approx \mu D_g p_s \left( \frac{V_x}{h_s} \right)^2 \qquad (1.1)$$

Models for the material removal rate for rolling-indenting and scratch-indenting cases were developed for free abrasive wire saw machining by Yang and Kao (2001). The models are a function of process parameters and work piece mechanical properties. The models are just compared with respect to each other, while comparison to experimental data is not done (Yang and Kao 2001).

Liu et al. (2004) stated that the material removal mechanism of bead-impregnated wire saw cutting of rock is a Hertzian type fracture in which the fracture occurs due to the tensile field behind the sliding bead.

### 1.1.2. Wire Vibration

Wei and Kao (1998) conducted stiffness analyses of a straight and bowed wire. Flexibility influence function (which is inverse of stiffness) is derived for straight and bowed wires. The stiffness is a function of wire tension, the location at which stiffness is obtained, and the external force acting on the wire and the wire radius of curvature. Closed-form solution for vibration displacement of axially moving wire is presented. The closed-form solution is used to obtain the closed-form solution of wire vibration due to forces applied by abrasive grits, which are rolling and indenting into the work piece. A harmonic excitation of 100 grits is taken and normalized vibration amplitude with respect to time and cut length is presented. If the wire speed $V_x$ reaches a critical value $V_{xc}$ (for industrial applications the critical speed is $V_{xc}$=300 m/s), the natural frequencies vanish and divergence instability occurs. The industrial wire saw speeds are less than 30 m/s, and therefore divergence instability is not a problem (Wei and Kao 1998).

Closed-form solution and finite element results for wire vibration under single and multiple excitations were presented by Wei and Kao (2000). The multiple excitations were due to forces applied by abrasive grits on the wire. The finite element results were in agreement with closed-form solutions for wire vibration amplitudes. One hundred multiple excitations were applied to the wire in the contact span with a varying excitation frequency. When the excitation frequency is close or same as the first natural frequency of wire, the vibration amplitude is obtained as infinity. The vibration amplitude is the same for the speeds

below 25 m/s and increases very small amount for higher speeds. The vibration amplitude decreases considerably when the tension is over 10 N. Beyond this range, the vibration amplitude changes nonlinearly with tension, such that further increase of tension does not decrease vibration amplitude proportionally. Also, the wire tension is limited by the wire yield strength. The increase of damping decreases vibration amplitude of the wire (Wei and Kao 2000).

Zhu and Kao (2005) modeled wire vibration in the wire saw process by coupling the dynamic equation of a stationary wire with Reynold's equation for the incompressible flow of slurry. The linearization of the coupled equations is done over an equilibrium position of the wire in the contact span. A Galerkin-based model discretization, which minimizes the error between the actual and discretized field, was employed for modal analyses. The verification of Galerkin-based model was done by using a finite element model applying direct time integration, which uses Newmark's method. Parametric study was carried out for wire vibration on a contact span of wire with work piece $L_o$, wire axial speed $V_x$, wire tension $T$, wire bow angle, and the dynamic viscosity of wire (Zhu and Kao 2005). The eigen values obtained by changing one parameter were used in a parametric study to determine the effect of this parameter on wire vibration. The model showed that as the contact span decreases, wire vibration amplitude increases. Also, the decrease of contact span may cause discontinuities in hydrodynamic film, which may lead to scratching of the wafer surface by the wire. The combination of the vibration and breakage of slurry film can cause scratches, especially at the entrance and exit sides of a circular wafer where contact spans at these sites are lowest. Poor surface finish and scratches were observed on entrance and exit sides of a circular wafer where contact span is small. The parametric study for speed of wire $V_x$ showed that the speed does not affect the vibration amplitude much. The practical speeds of wire saws in industry are well below the critical speed for instability. Reducing the speed to a very low value may cause interruption in the floating-machining environment and wire breakage may occur. Due to the parametric study, the increase of tension decreases wire vibration by a considerable amount. The total force acting on the sample by the wire is determined by the wire tension and the bow angle. The increase of the bow angle decreases the wire vibration. However, if the bow angle is increased over a critical value, slurry film may break down,

which may lead to wire-work piece direct contact and wire breakage and scratches on the wafer. Slurry viscosity does not affect the vibration amplitude of the wire (Zhu and Kao 2005).

### 1.1.3. Parametric Studies on the Wire Saw Process

Process monitoring of the wire saw process for forces, wire speed, feed rate, wire bow, and wire tension was developed by Clark et al. (2003a). The wire tension on both sides of the work piece is derived as a function of wire bow angles on both sides of the work piece and horizontal and vertical cutting forces. The developed process monitoring was used as part of a parametric study on the wire saw process (Clark et al. 2003a).

Clark et al. (2003b) conducted the parametric study relating process parameters with forces, surface roughness, and wire wear for cutting foam ceramics and wood. Three types of wood (pine, oak, and fir) and three types of foam ceramics (SiC, transformation toughened zirconia (TTZ), and zirconia toughened alumina (ZTA)) were cut with a fixed a diamond wire. Wire endurance tests were then done by cutting pine wood sixteen times with the same wire. The first three cuts with a new diamond wire had approximately the same amplitude of vertical and horizontal cutting forces, while vertical cutting forces are always higher than the horizontal cutting forces. The first cut had a vertical cutting force of 2.4 N, while the sixteenth cut has 7.4 N, which shows an increase of three times in the vertical cutting force due to wire wear. The vertical-to-horizontal-force ratio remained between 1.8-2.8. The force ratios for cubic boron nitride (CBN) grinding of zirconia are between 3-15, for CBN grinding of tool steel are 3-10, for CBN grinding of silicon nitride are 4-9, and for diamond grinding of silicon nitride are 5-5.5. The low force ratio obtained in wire saw cutting means an efficient cutting condition for wire saw cutting of wood. In the endurance tests of wire while cutting pine, the cutting forces increase and surface roughness remains constant as the cut number increases. The increase of cutting speed for pine and oak cutting does not affect cutting forces and force ratio except increasing the cutting speed to $V_x$=9 m/s for pine. At $V_x$=9 m/s for pine cutting, the cutting forces and force ratio are smaller with respect to forces and force ratio obtained with lower speeds ($V_x$=4.5-6 m/s). The speed of the rocking motion of wire does not affect the cutting forces for pine and oak woods. The variation in cutting

conditions due to cutting a harder material were tested by cutting earlywood (softer) and latewood (harder) of Douglas fir wood. The horizontal cutting force does not change while the wire bow increases almost two times when cutting harder latewood. The increase of wire bow increases the vertical force two times, as the wire tension, feed, and wire speed are the same. Thus, the vertical-to-horizontal-force ratio is higher for cutting harder latewood. The surface roughness of pine cuts does not change with changing wire speed $V_x$ and wire rocking frequency. SEM micrographs of diamond wire used in cutting oak wood show that the metal bond holding the abrasive grits gets abraded and plastically deformed. For the same cutting conditions, the force ratio of SiC cutting is one order of magnitude higher than TTZ and ZTA cutting. Increasing the wire speed from 4.5 to 6 m/s decreases the cutting forces for TTZ and ZTA. The diamond wire saw cutting is found to be very suitable for cutting foam ceramics, while wire life for wood cutting is low. Using a mist of water during cutting wood improves wire life considerably (Clark et al. 2003b).

Hardin et al. (2004) conducted a parametric study for slicing single crystal SiC with a fixed abrasive diamond wire, relating wire speed, rocking frequency, and down feed rate with specific normal force and specific tangential force, normal-to-tangential-force ratio, surface roughness, and subsurface damage. Cutting forces were measured by a piezoelectric dynamometer and divided to wire diameter and cut length to get specific normal and horizontal forces. Hardin found that the increase of wire feed speed increases specific normal force, while it does not affect specific tangential force. The force ratio increases as feed speed increases while the surface roughness is independent of feed. The low force ratio shows that wire saw cutting of SiC is an efficient process. The increase of wire speed does not show a clear trend for tangential force and surface roughness. The surface roughness obtained without a rocking motion of the wire is higher than the roughness obtained by rocking the wire. The frequency of the rocking motion does not affect the tangential force and surface roughness.

Closed-loop diamond impregnated wire saw cutting of $Al_2O_3$ and TiC ceramics showed that cutting forces, surface roughness, and wire wear decrease as the wire speed is increased while a higher feed rate increases the cutting forces, surface roughness, and wire wear (Meng et al. 2006).

Critical load and indentation hardness for ductile regime material removal for brittle materials were presented by Meng et al. (2004). The depth of cut for a wire saw as a function of wire speed, feed speed, density of grains on the wire saw per area, radius of wire, and included angle of grains was derived. It is stated that, theoretically, increasing wire speed and density of grains on the wire and decreasing the feed rate will allow ductile regime cutting. A ductile regime cutting of granite is presented, which complies with the derived theory (Meng et al. 2004).

An endless diamond wire saw with electroplated diamond is used to cut granite by Ge et al. (2004). The feed is applied as a constant weight load. Cutting forces are measured by a dynamometer. As grain size of diamond increased cutting forces increased, efficiency increased. The increase of wire speed increases efficiency and decreases cutting forces. The increase of feed load increases efficiency and cutting forces. The increase of hardness of material decreases efficiency and increases cutting forces. Use of coolant increases efficiency while cut forces decreases (Ge et al. 2004).

Effects of different process parameters on the performance of the diamond wire sawing processes are investigated by using the Taguchi method applied on a set of tests by Pei-Lum et al. (2006). Use of small grain size (20-30 μm), high wire speed (5 m/sec), and low feed rate (2 μm/sec) yields better surface roughness. Large grain size (30-40 μm), high wire speed (5 m/sec), and feed rate (10 μm/sec) with water slurry lead to higher value of MRR. Feed rate is dominant on MRR. Fast wire speed, high feed rate, and slurry (water) lead to increased wear of wire. Using slurry causes larger removal rate and larger wear of wire. Wire tension does not affect the performance (Pei-Lum et al. 2006).

### 1.1.4. Other Research Work on the Wire Saw Process

Li et al. (1998) proposed a contact stress model of an abrasive indenter on a surface. The rolling-indenting process of an abrasive on a surface is considered in modeling the stresses. The stresses were expressed with dimensionless stress measures as functions of normalized geometric parameters. The stresses arising from normal and tangential forces were superposed. The maximum normal stress occurs at the contact point where an irreversible deformation zone is formed. The maximum shear stress occurs under the

indentation point and causes a peeling effect. The optimal abrasive geometry is defined as a cube (Li et al. 1998).

Kim and Kim (2005) stated that if mechanical damage exceeds a critical value, dislocation loops are formed, and if it is below the critical value, stacking faults are formed during oxidation at the surface of silicon. Small mechanical damage induced by scratching with sand paper or silica wet blasting induces stacking faults during oxidation of the silicon crystal. Severe mechanical damage produced by heavy scratching with sand paper and by the wire cutting process creates dislocation loops in the silicon crystal during oxidation treatment (Kim and Kim 2005).

The shadow Moiré technique was used to get wafer surface topology by Kao et al. (1998). He-Ne laser was used to make a shadow using fine grating on the wafer surface. The fringe patterns occur due to interference between the grating and its shadow is formulated. This is a non-contact technique which allows getting the entire wafer surface topology without moving the wafer (Kao et al. 1998).

Experiments have been conducted in dry and wet, muddy conditions to determine the friction coefficient between a rubber-coated drive pulley and the diamond wire. The average friction coefficient in wet and muddy conditions is $\mu=0.32$ (Dunda 1998).

The effect of wire tension and feed rate on low frequency waviness was investigated in experimental and analytical work by Bastawros et al.(2006). An increase in wire tension decreases the amplitude of waviness, while an increase of feed rate increases the amplitude of waviness (Bastawros et al. 2006).

The multiple simultaneous indentation response of brittle materials was simulated using FEM by Bhagavat and Kao (2007). Abaqus software was used for analyses. As the spacing between the abrasives decreases, the load required to achieve a certain depth decreases, while the amount of elastic recovery increases causing more material removal due to increased formation of lateral crack. The decrease of abrasive spacing increases sink-in, which causes a decrease in the friction between the abrasive and the work piece. The load required to indent to a certain depth is higher for a tip having a radius with respect to a tip having an infinite sharpness. The indentation profiles are axisymmetric. The trend of change

of mean contact pressure with increasing depth is constant for all spacing (Bhagavat and Kao 2007).

The non-centrosymmetric nature of lithium niobate causes different hardness and fracture toughness on opposite faces of a wafer. Nano-indentation was used in three common directions to study hardness anisotropy by Bhagavat and Kao (2005). The opposite faces with same indentation directions have different hardness. Indentation size effect is seen such that as maximum load increases, hardness decreases. Lithium niobate has a pop-in phenomenon due to crystal orientation, while no-pop out is observed. The pop-in phenomenon is an abrupt increase in displacement with almost no change of applied force. The motion of dislocations is the reason of pop-in phenomenon (Bhagavat and Kao 2005).

The direction of approach (DOA) was determined for different surface normals of wafers maintaining surface quality, MRR, on both sides of wafers by Bhagavat and Kao (2006). When the DOA is perpendicular to a cleavage direction, then the longitudinal direction of the wafer aligns with the cleavage direction, which increases the tendency of wafer breakage, resulting in lower yield of wafers. If an appropriate DOA is chosen, this can be avoided. DOA recommendations are made for three most commonly sliced orientations of silicon: (110), (100), (111) (Bhagavat and Kao 2006).

The machining-induced temperature variation can cause warping of wafers in the wire saw process. The ingot's temperature variation during wire saw cutting was modeled using the finite element method by Bhagavat and Kao (2008). The model integrates heat flux and natural convection boundary conditions. Time-dependent boundary conditions and geometry are considered in the model. The model is compared to experimental results in the literature. A method which includes control of boundary conditions for reducing warping due to temperature variations was proposed (Bhagavat and Kao 2008).

In all of these efforts, analytical damage models relating roughness and waviness damage with process parameters for the wire saw process have not been studied. Also, the surface damage depth due to the wire saw process, which determines the amount of post processing to remove the damage, has not been investigated. These are the subjects of this study.

Damage to silicon wafers resulting from the wire saw process is important as the photovoltaic and semiconductor industry has strict tolerances for surface quality. The wire saw process induced damage is the main concern of this study. In modeling damage due to any machining process, the indentation and scratch damage models are the starting point. The damage mechanisms of brittle materials are presented in the following section.

## 1.2. Damage Models for Brittle Materials

Although the cracking sequence of brittle materials under indentation varies with material properties, load amplitude, and several different indentation parameters, a general cracking sequence can be defined using Yoffe's (1982) model as follows. The indentation is done in loading and unloading half cycles which drive different cracks. During the loading half cycle, a plastic zone under the indenter expands as the load increases as seen in Fig. 1.5. The horizontal tensile stresses under the plastic zone initiate and expand median cracks. The median crack extends vertically as the load increases. In some materials, dependent also on the load range, surface radials can initiate during the loading half cycle. During unloading, the elastic field recovers the displacements while the plastic field restraints the recovery, which causes lateral crack initiation and extension parallel to the surface. The lateral cracks may turn to surface and reach the free surface if enough crack driving force is available. The vertical extension of median crack stops during unloading and surface radials, and median cracks can unite to form a half-penny-shape crack at the end of unloading.

The threshold load below which plastic deformation and above which lateral cracking causes material removal is determined in terms of material parameters, hardness, fracture toughness and Young's modulus by Evans and Marshall (1980). If the applied load is smaller than the threshold load, the plastically deformed material is removed by plastic cutting so the residual forces due to the plastic zone diminish and, hence, lateral cracking does not occur (Evans and Marshall 1980). Over the fracture threshold load, the fracture can be suppressed by high hardness or high toughness. Below the fracture threshold load, where plastic deformation occurs, material removal depends on hardness. Materials having high hardness and high toughness are wear resistant. The threshold load decreases as hardness increases; thus, material fails in a brittle lateral crack mode. Loads very close to the threshold load may

cause higher wear for materials having high hardness (Evans and Marshall 1980). The lateral crack length in a brittle fracture is determined in terms of material parameters by Evans and Marshall (1980). The material removal volume of a sliding particle is developed using lateral crack length expressions. The comparison of the developed expressions to tests is successful. The average temperature rise due to indentation was modeled, and it was mentioned that the temperature increase has a minor importance unless the material has a large thermal expansion coefficient and a low specific heat (Evans and Marshall 1980).

A fracture-mechanics-based model relating radial and median cracks occurring in the far field of sharp indenter tip was developed by Lawn et al. (1980). The complex elastic/plastic field under the indenter is decomposed into elastic and plastic components. The elastic component drives the median crack during the loading half cycle while suppressing the development of radial crack. The residual component is mostly effective in the unloading half cycle where the median crack unites with the surface radials and reaches a half-penny crack shape. The effect of residual field is applied by considering an expanding plastic field. The obtained crack length has two fitting parameters that are calibrated using soda-lime glass. The calibrated model is capable of predicting the crack extension behavior of other brittle materials. The model is a function of hardness-to-modulus ratio along with toughness (Lawn et al. 1980).

A model for predicting lateral crack depth and extension was derived by Marshall et al. (1982). The residual forces due to plastic impression are the driving forces of lateral cracks during the unloading half cycle. The equilibrium lateral crack length was found to be a function of the hardness-to-modulus ratio, toughness, included angle of the indenter, and the load. The model has two fitting parameters which are used for verification. Verification of the model was done by comparing the model with experimental observations for different materials. The volume removed during erosion of brittle materials is derived using the lateral crack model (Marshall et al. 1982).

The volume of the plastic zone is related to the indentation volume and pressure. The Hill's solution of expanding spherical cavity in an infinite media is adjusted for the free surface of the indentation problem (Chiang et al. 1982a). The plastic zone dimension

predictions obtained from the derived model comply with the experimental observations. The tensile stress locations obtained from the model comply with the definitions of radial, median, and lateral cracks. The model predicts compressive stresses in the plastic zone, which terminates crack extension; peak tensile stress at the elastic-plastic interface, which is the point for crack initiation; and tensile stress fields in the elastic region, which is the source of crack extension (Chiang et al. 1982a). The fracture initiation for elastic/plastic indentations is investigated considering two sources of origination; preexisting flaws due to machining or stress singularities created by shear bands. Radial crack initiation is predicted from existing flaws (Chiang et al. 1982b). The model proposed by Chiang et al. (1982a, b) needs an iterative solution.

Yoffe (1982) has developed an elasto-plastic indentation damage model for brittle materials. The model defines the stresses in the plastic zone as $p$ and $q$, vertical and horizontal stress, respectively. These stresses are compressive in nature. The relation between $p$ and $q$ is derived using the minimum strain energy theorem as the equilibrium position will be a minimum energy state. The estimates of the $q$ are $q$=0.2$p$ for silica, 0.33$p$ for soda-lime glass, and 0.5$p$ for common metals. As the load increases, yielding takes place and the mean pressure remains the same. The yielding under the indenter is propagating as concentric hemispheres are yielding one after another and reaching the same stress state. The glasses yield step-by-step: at every step a new larger circular elastic/plastic boundary forms. For metals, the plastic zone may start outside the contact impression. During unloading and at a fully unloaded configuration, the plastic zone formed in glasses will tend to protect their shape while the surrounding elastic media will tend to recover the deformations, which will cause cracking. The stresses outside the plastic zone, in the elastic region, are a superposition of the Boussinesq solution and the Blister field. The Boussinesq solution gives the displacements and stresses due to a normal force on an elastic, isotropic half space. The Blister field is obtained by combining a symmetrical center of pressure with a double force in the $z$ direction (normal to the free surface). The strength of the Blister field is small for compressible material indented with a large-angle indenter. The corners of a Vickers indenter will increase the stresses that cause radial cracks even with a low Blister field strength. After fully unloading, tensile stresses that will cause lateral cracks parallel to that surface are

observed, while tensile stresses close to the surface will create new radials and connect the radial cracks with median cracks to form a half-penny shape (Yoffe 1982).

Cook and Pharr (1990) presented a detailed review of the literature on indentation crack systems of glasses and ceramics. Detailed indentation experiments on glasses and ceramics have been conducted to gather load-displacement data to capture the crack initiation and propagation during indentation cycles. The indentation crack system is classified into five categories. The cone cracks which initiate perpendicular to surface during loading are observed in anomalous amorphous glasses, as seen in Fig. 1.6. Radials and secondary radial cracks, which are perpendicular to the free surface, may initiate during loading or unloading depending on the material. Median cracks develop under the plastic zone during loading as seen in Fig. 1.6. Half-penny cracks are a combination of surface radials and median cracks. Lateral and shallow lateral cracks are parallel to the free surface as seen in Fig. 1.6. A stress-based indentation damage model for brittle materials was presented by Cook and Pharr (1990). The stress state during loading and unloading is a superposition of the Boussinesq solution and the Blister field. The Blister field was the one derived by Yoffe (1982). The crack initiation and propagation sequence of brittle materials are predicted by the model (Cook and Pharr 1990).

A stress-based damage model for sliding micro indentation was developed by Ahn et al. (1998). The stress state is derived as a superposition of the Boussinesq solution for a point normal load, the Cerruti solution for tangential load, and a sliding Blister field derived by Yoffe (1982). The model predicts that lateral cracking occurs due to the inelastic Blister field, while median cracking occurs due to applied forces as seen in Fig. 1.7. The crack-driving stresses are a function of applied load for both lateral and median cracks. Lateral cracks will grow only at loads higher than a threshold and after unloading from the peak load. When the load is removed, the lateral crack initiates just under the last position of the indenter and propagates backwards towards the starting point of sliding, where it stops (Ahn et al. 1998).

A stress-based damage model was developed for scratch-induced damage in brittle solids by Jing et al. (2007). The stress-based model combines the Sliding Blister Field Model

and the Expanding Cylindrical Cavity Model to predict the initiation and propagation of damage due to scratching of brittle materials. The strength of the Blister field and the inelastic zone size are obtained in terms of material properties, the geometry of the indenter, and the loading conditions. The maximum principal tensile stress direction is used to predict the crack initiation and propagation sites (Jing et al. 2007).

Micro-fracture and material removal due to scratching of alumina was studied experimentally by using a bonded-interface sectioning technique by Xu and Jahanmir (1995). The subsurface damage and material removal modes were investigated with respect to grain size, load, and number of passes in a single point scratching of alumina. A model relating material removal rate to applied load and material properties was derived (Xu and Jahanmir 1995).

The impact damage and erosion resistance of brittle materials was studied by Sheldon and Finnie (1966). The volume removed by impact to a brittle material is obtained as a function of material properties, average radius of impacting particle, and its velocity. The Weibull fracture strength distribution is used in the model. The model was compared with impact tests using both angular silicon carbide particles and steel balls. The model is capable of predicting trends for the effect of particle radius and velocities (Sheldon and Finnie 1966).

Impact damage of brittle materials by hard projectiles was studied by Evans et al. (1977). The damage is investigated by observing the extent of radial fracture and depth of lateral fracture. Dynamic stress analyses and fracture mechanics concepts are used to explain the damage. The toughness of the target, velocity, and radius of the projectile determine the extent of the radial crack, while lateral-crack depth is determined by the hardness of the target and velocity, and the radius and density of the projectile. The strength degradation and erosion was discussed using the models for impact damage (Evans et al. 1977).

The erosion of brittle materials was modeled using the Monte Carlo method by Verspui et al. (1999). The model relates the erosion rate and surface roughness to material properties of target and abrasive particles. Indentation fracture mechanics concepts are used to relate the damage to parameters, which were defined by Marshall et al. (1982). Particle

size and velocity distributions are assumed to be Gaussian. The assumption of a lateral crack starting at the bottom of the indentation gives better results. Impacting projectile radius and velocity are important parameters affecting the results. The erosion rate predicted complies with abrasive water jet machining of glass. The surface roughness predicted is larger than the experimental surface roughness, which may be due to the stylus radius used in roughness measurements (Verspui et al. 1999).

The damage models presented so far have been used to model material removal rate and damage in machining of brittle materials. Although the literature presented so far is also related to machining damage of brittle materials, it will be valuable to review this part in a more detailed approach. The review of literature on models about machining brittle materials is presented in the next section.

## 1.3. The Machining of Brittle Materials

A stress-based damage model for grinding-induced damage was developed and verified by experimental observations by Chandra et al. (2000). The model is used in exploring the applicability of intermittent unloading in grinding of brittle materials. Intermittent unloading develops by vibrating the work piece by a magnetostrictive actuator. This unloading is used to develop a lateral crack that will terminate the extension of the median crack deep into the work piece during engagement of later grits with higher forces. The limiting of the median crack length reduces process-induced damage, while the lateral crack is involved in material removal (Chandra et al. 2000).

The grinding mechanisms and strength degradation is studied using two approaches by Malkin and Ritter (1989): the “machining” approach and “indentation fracture mechanics” approach. The machining approach is conducted with cutting-force measurements, specific energy considerations, surface morphology of the product, and grinding detritus. The indentation fracture mechanics approach is used to determine the volume of material removed, the threshold load for lateral cracking, and the radial crack size (Malkin and Ritter 1989).

Material removal and the roughness of the lapping process are modeled using the concept of lateral fracture and three-body abrasion via rolling and indenting of abrasives by Buijs and Korpel-van Houten (1993a). The models are a function of Young's modulus, hardness, toughness, lapping plate velocity, and total load applied on the plate. The model allows determination of an average normal force per abrasive that can be determined from Preston's coefficient and the characteristics of the work piece and abrasive (Buijs and Korpel-van Houten 1993a).

A model for lapping of glass, which relates material removal rate, surface roughness, subsurface damage, and load per particle to particle shape, size, material parameters of the work piece and lapping plate pressure and relative velocity between the plate and work piece, was developed by Buijs and Korpel-van Houten (1993b). The material removal rate and damage in the final product are modeled using the indentation fracture mechanics model of Lawn et al. (1980). If the removal rate, surface roughness, or damage penetration is known, the other two can be calculated (Buijs and Korpel-van Houten 1993b).

The oxide layer and water-based slurry produce a softer hydroxylated interface layer that is removed in the chemical mechanical polishing (CMP) process. The removal of the hydroxylated layer is a perfectly plastic material removal. The material removal rate (MRR) in the CMP process is modeled using spherical or sharp particle contact. Also, stiff pad and high abrasive concentration (wafer and pad are not in contact) and soft pad and low abrasive concentration (extended contact between pad and wafer) are considered. Comparison of the model to nano-indentation and CMP experiments on glass and other materials validate the model. The comparison with experimental data shows that most of the CMP operations are in the soft pad and low abrasive concentration mode (extended contact between pad and wafer) (Fu et al. 2001).

Reducing the in-feed rate below a limit in grinding of brittle materials causes a transition of material removal mode from brittle to ductile. The ductile mode of machining brittle materials is known as ductile regime grinding. The ductile regime grinding of brittle materials is defined as the final product will have less than 10% surface fracture, which means there is still brittle failure defined as a percent of surface area. The 10% surface

fracture is chosen by the author arbitrarily for brittle-to-ductile transition. The surface finishes obtained by ductile regime grinding are similar to polishing or lapping, while grinding is a deterministic process that allows contour accuracy and complex shapes. A stiff grinding machine is introduced by its working principals for ductile regime grinding. The critical in-feed rate, below which 10% of surface fracture can be obtained, is developed using critical depth of fracture equations. The derived equation is fit to experimental results and the trend is verified (Bifano et al. 1991).

Yoshioka et al. (1985) stated that a ductile regime grinding machine has been developed, which can be used for grinding brittle materials in a plastic deformation mode. The machine has high stiffness and high precision in truing and dressing the grinding wheel. The obtained surface roughness is 2 nm for quartz crystal (Yoshioka et al. 1985).

The availability of ductile-regime machining of brittle materials can be valid also for the wire saw process in which the wire, as a compliant tool, coupling with low feed rates may result in ductile-regime machining. The next section is devoted to machining of ductile materials and general wear models.

### 1.4. Ductile Mode Material Removal and Wear Models

The surface ploughing with a pyramidal indenter was studied using the upper bound method by Wathaire et al. (1981). The model determines the normal and tangential forces, the geometrical parameters of the track, and the strain and strain rate of the ploughed material. The model agrees with the experiments done with half-included-angle indenters between $35^o$-$70^o$. It is found that the chips are formed by indenters with small angles, while large-angle-indenters develop frontal ridges (Wathaire et al. 1981).

A model for three dimensional cutting using an irregular pyramidal abrasive was developed by Torrance (1987). The predictions of the model were compared with experimental results. The results obtained from the model are as follows: 1. A blunt abrasive that is held rigidly cuts more efficiently than a flexibly mounted abrasive; 2. The minimum

possible specific energy for the abrasion of a metal with conventional abrasives is 4.5 times the shear yield strength of work piece.; and 3. In order to reduce the specific energy for cutting, abrasive shape can be modified (Torrance 1987).

The contact and rubbing of flat surfaces were studied by Archard (1953). The electrical conductance of two surfaces is obtained by considering single and multiple areas of contacts. The contact resistance of clean metals is determined by low frequency waviness of the surface. The nominally mating surfaces might have elastic deformations due to contact resistance measurements while the friction between the surfaces might be determined by the plastic deformation of the small asperities. A simple theory for wear was developed. The theory states that the wear rate is proportional to load while being independent of contact area. If yield strength of material and the probability of wear are constant, the wear rate is independent of contact area. The model used to represent the surfaces does not affect the wear rate (Archard 1953).

A new theory of elastic contact was established by Greenwood and Williamson (1966). Contact deformation depends on the surface topography. Separation depends on nominal pressure, number of micro-contacts, and total area of contact depend on load only. A plastic index is defined as hardness ratio (Plastic index=Elastic Hardness / Real Hardness). Contact between solids is controlled by two material properties—plane stress elastic modulus and hardness—and three topographic properties—surface density of asperities, standard deviation of height distribution, and mean radius of peaks. Gaussian distribution fits well for roughness. The plasticity index, and thus elastic or plastic contact, depends on surface topography, which depends on surface processing techniques. The contact between surfaces is generally plastic, while elastic contact can also be observed in engineering practice (Greenwood and Williamson 1966).

Wear maps, a function of nominal pressure and sliding velocity, were introduced by Williams (1999). The wear map for carbon steel shows that, at low speeds, the wear is mechanical and independent of speed; at high speeds, the wear is severe oxidational wear, which is a function of both speed and pressure. Mechanical wear processes are defined as abrasion due to polishing, ploughing, and micromachining; erosion due to cavitations and

liquid-solid impact; and adhesion and surface fatigue due to ratcheting, delamination, and pitting. Two and three dimensional abrasive wear models in the literature are discussed (Williams 1999).

A simulation model was developed to predict the friction and wear in rolling-sliding contact by Telliskivi (2004). Archard's law was used for wear prediction. Deformation and relative motion of every part is predicted during analysis. The disc-on-disc test for dry wear is simulated. The Winkler mattress method is used to solve the deformation field. The tangential stress field is calculated from the normal pressure field, the penetration, and the general rigid-body movement for every sub-region. Tangential reaction and the displacement field in contact are predicted by influence functions from the potential theory. Elastic displacements are subtracted from the relative motion of the body to find sliding distance. There are elastic deformations both in the sticking and sliding regions. The model predictions are satisfactory for wear and rolling friction when compared with disc-on-disc test (Telliskivi 2004).

### 1.5. Motivation and Proposed Work

The silicon wafers used in the photovoltaic and microelectronics industries are obtained using the wire saw process or the inner diameter (ID) saw. The wire saw process is advantageous over the ID saw because the wire-saw process has a higher yield, lower kerf loss, and lower surface damage. The wire saw process can be used to cut all kinds of brittle materials with low surface damage and higher yield.

In the 1990s, the wire saw process consisted of a bare steel wire and abrasive carrying slurry, which leads to rolling and indenting material removal. The bow and tension of the wire transfers a hydrodynamic pressure on the abrasive grits through the slurry. The velocity profile of the slurry trapped between the wire and sample, occurring due to wire speed, is providing the motion of the abrasive grits. The combination of hydrodynamic pressure and the motion of the grits results in rolling-indenting motion of grits, which causes material removal in free-abrasive machining. The increase of wire bow or tension may cause

disruptions in the hydrodynamic film, which leads to bare wire-sample direct contact. This direct contact creates scratches on the sample, while causing wire breakage. In order to keep the hydrodynamic film, the wire velocity in the abrasive-carrying wire-saw process is high.

Diamond-grit coated steel in the wire-saw process was developed due to the disadvantages of the abrasive-slurry wire-saw process. The diamond-grit coated wire-saw process leads to fixed abrasive machining. This process has a higher yield and less wire breakage in comparison to the abrasive-carrying slurry wire-saw process. In this work, the abrasive-grit coated wire-saw process is investigated.

The wire saw process induces roughness and long waviness damage on the cut surface. These damages decrease the quality of the wafers and have to be removed by post processes including grinding, lapping, and polishing. However, these post processes increase wafer manufacturing costs.

Although the wire-saw process has been used by the photovoltaic and semiconductor industries, a roughness damage model that relates process parameters to damage occurring on the cut surface has not been established in the literature. The reasons of the long waviness formation and mechanisms controlling the long waviness have also not been studied. In addition, the correlation of surface damage depth with process parameters has not been investigated elsewhere.

The overall goal of this study is to understand the surface roughness and long waviness damage for the abrasive wire cutting and to establish the role of the process parameters. Once these mechanisms are understood, a mechanistic framework will be established and calibrated to provide capabilities for predictive tools that can be used in design space exploration. In particular, the current efforts will focus on:

1. Understanding mechanisms of surface roughness damage.
2. Measurement and analyses of surface-damage depth with respect to process parameters.
3. Understanding mechanisms of long waviness formation.

The specific goals of this study is to conduct parametric studies on the process parameters, including the wire speed, down-feed speed, and wire tension, as well as the role of consumables on the quality of the cut surface. Thus, detailed analysis of the wire

properties including grit size, spacing, and wire diameter will be examined. The explored trends will be utilized to calibrate the developed model's surface roughness and long waviness damage.

Several tools will be utilized to achieve the above goal, including:

1. A lab-scale single wire-saw machine.
2. Dynamic load cells and data acquisition system.
3. Surface analysis using non-contact optical profilometer and scanning electron microscopy (SEM).
4. In situ digital imaging to monitor the evolution of wire bow angle.

**1.6. Dissertation Organization**

The remainder of the thesis is organized so that the goals listed above are addressed. The experimental setup and preliminary experimental results are presented in Chapter 2. The experimental parametric study relating wire characteristics with roughness damage is presented in Chapter 3. Chapter 3 also includes the roughness damage models and verification of the roughness damage models with experimental results. The experimental parametric study relating the wire tension and feed speed with long waviness formation is presented in Chapter 4. The analytical model enlightening the long waviness formation is also presented in Chapter 4. The experimental parametric study relating surface-damage depth with process parameters is presented in Chapter 5. The design space exploration, which includes the affect of different process parameters on different damage systems, is also presented in Chapter 5. Finally, overall conclusions of this work and future work are presented in Chapter 6.

**1.7. References**

Ahn. Y., Farris., T.N., Chandrasekar S., " Sliding Microindentation fracture of Brittle Materials: Role of Elastic Stress Fields" Mechanics of Materials V. 29 (1998) pp.143-152.

Archard J.F. "Contact and Rubbing of Flat Surfaces", Journal of Applied Physics, Vol. 24 No.8 (1953) pp.981-988.

Bastawros A.F., Chandra A., Shih A.J, “Analysis of Surface Waviness during Wire Saw Cutting of Ductile Materials” Proceedings of 2006 NSF Design, Service and Manufacturing Grantees and Research Conference, St. Louis, Missouri.

Bhagavat M., Kao I., “Computational Model for Free Abrasive Machining of Brittle Silicon Using a Wiresaw”, Electronics Manufacturing Issues ASME, DE-Vol. 104, (1999) pp21-30.

Bhagavat S., Kao I., “A Finite Element analysis of temperature variation in silicon wafers during wiresaw slicing”, International Journal of Machine Tools and Manufacture, Vol. 48 (2008) pp. 95-106.

Bhagavat S., Kao I., “Nano Indentation of Lithium Niobate : Hardness anisotropy and pop-in phenomenon” , Materials Science and Engineering A, V.393 (2005) pp.327-331.

Bhagavat S., Kao I., “Theoretical analysis on the effects of crystal anisotropy on wiresawing process and application to wafer slicing”, Machine Tool and Manufacture” V.46 (2006) pp.531-541.

Bhagavat S., Kao I., “Ultro Low Load Multiple Indentation Response of Materials: In purview of wire saw slicing and other free abrasive machining (FAM) processes”, Machine Tools and Manufacture, V.47 (2007) pp.666-672.

Bhagavat, M., Prasad, V., Kao, I. “Elasto-Hydrodynamic Interaction in the Free Abrasive Wafer Slicing Using a Wiresaw: Modeling and Finite Element Analysis” Transactions of ASME, Tribology Division, Vol.122 (April 2000) pp394-404.

Bifano, T.G., Dow T.A., Scattergood R.O., “Ductile-Regime Grinding : A New Technology for Machining Brittle Materials,” Journal of Engineering for Industry, Vol. 113 (1991) pp.184-189.

Buijs M., Korpel Van Houten K., “A model for lapping of glass”, Journal of Materials Science, Vol. 28 (1993a) pp.3014-3020.

Buijs M., Korpel Van Houten K.,” Three-body abrasion of brittle materials as studied by lapping”, Wear, V.166 (1993b) pp.237-245.

Chandra A., Wang, K., Huang, Y., Subhash, G., Miller, M.H., Qu, W., "Role of Unloading in Machining of Brittle Materials", Journal of Manufacturing Science and Engineering, Vol.122, (August 2000) pp.452-462.

Chiang S.S., Marshall D.B., Evans A.G., "The response of solids to elastic /plastic indetation. I. Stresses and Residual Stresses" Journal of Applied Physics, Vol. 53 No.1 (1982a) pp.298-311.

Chiang S.S., Marshall D.B., Evans A.G., "The response of solids to elastic /plastic indetation. II. Fracture Initiation" Journal of Applied Physics, Vol. 53, No.1., (1982b) pp.298-311.

Clark, W.I., Shih, A.J., Hardin, C.W., Lemaster, R.L., McSpadden, S.B., "Fixed abrasive diamond wire machining – Part I: process monitoring and wire tension force", International Journal of Machine Tools and Manufacture V.43 (2003a) 523-532.

Clark, W.I., Shih, A.J., Hardin, C.W., Lemaster, R.L., McSpadden, S.B., "Fixed abrasive diamond wire machining – Part II: experiment design and results", International Journal of Machine Tools and Manufacture V.43 (2003b) 533-542.

Cook R.F., Pharr G.M., " Direct Observation and Analysis of Indentation Cracking in Glasses and Ceramics" Journal of American Ceramic Society, V.73 No.4 (1990) pp.787-817.

Dunda S., "Friction Coefficient of Diamond Wiresaw" Rudarsko geolosko naftni zbornik, Vol. 10, Zagreb (1998) pp.59-61.

Evans A.G., Gulden M.E., Rosenblatt M., " Impact damage in brittle materials in the elastic-plastic response regime", Proceedings Royal Society of London A, V. 361, (1978) pp343-365.

Evans, A.G., Marshall , D.B., "Wear Mechanisms in Ceramics", Fundamentals of Friction and Wear of Materials, ASM Materials Science Seminar, Pennsylvania ,(1980) pp.439-449.

Fu., G., Chandra A., Guha S., Subhash G., "A plasticity Based Model of Material Removal in Chemical Mechanical Polishing (CMP)" IEEE Transaction on Semiconductor Manufacturing, Vol. 14 No: 4 (November 2001) pp.406-417.

Ge P.Q. , Zhang L., Gao W., Liu Z.C. “Development of Endless Diamond Wiresaw and Sawing Experiments” , Materials Science Forum Vols. V.471-472 ( 2004) pp.481-484.

Greenwood J.A., Williamson J.B.P “Contact of Nominally Flat Surfaces”, Proc. Royal Society of London, Ser.A, (1966) pp. 300-319.

Hardin C.W., Qu J., Shih A.J., “ Fixed Abrasive Diamond Wire Saw Slicing of Single-Crystal Silicon Carbide Wafers” , Materials and Manufacturing Processes Vol., 19, No. 2, (2004) pp. 355-367.

Jing, X., Maiti, S., Subhash, G., “A New Analytical Model for Estimation of Scratch-Induced Damage in Brittle Solids”, Journal of American Ceramic Society, V.90 No.3 (2007) pp.885-892.

Kao I, Prasad V., Chiang F.D., Bhagavat M., Wei S., “Modeling and Experiments on Wiresaw for Large Silicon Wafer Manufacturing” Electrochemical Society Proceeding Vol. 98-1 (1998) pp.607-619.

Kim J. M., Kim Y. K., “Saw-Damage –Induced structural defects on the surface of Silicon Crystals” , Journal of Electrochemical Society, V.152 No.(3) (2005) pp.189-192.

Lawn B.R., Evans A.G., Marshall D.B., “Elastic /Plastic Indentation Damage in Ceramics: The Median /Radial Crack System”, Journal of the American Ceramic Society, Vol. 63, No:9-10 (1980) pp.574-58.

Li, J., Kao., I., Prasad, V., “ Modelling Stresses of Contacts in Wiresaw Slicing of Ploycrysalline and Crystalline Ingots: Application to Silicon Wafer Production”, Journal of Electronic Packaging, ASME, Vol. 120 (June 1998) pp. 123-127.

Liu, B.C., Zhang, Z.P., Sun, Y.H., “Sawing Trajectory and Mechanism of Diamond Wiresaw”, Key Engineering Materials, Vols. 259-260 (2004) pp.395-400.

Malkin S., Ritter J.E., “Grinding Mechanisms and Strength Degradation for Ceramics”, Journal of Engineering for Industry, (May1989) Vol.111 pp.167-173.

Marshall D.B., Lawn B.R., Evans A.G., “Elastic /Plastic Indentation Damage in Ceramics: The Lateral Crack System”, Journal of the American Ceramic Society, Vol. 65 No:11 (1982) pp.561-566.

Meng J.F., Li, J.F., Ge, P.Q., Zhou R., “Research on Endless Wire Saw Cutting of $Al_2O_3$/TiC Ceramics” Key Engineering Materials V.315-316 (July 2006) pp.571-574.

Moller, J.H., “Basic Mechanisms and Models of Multi –Wire Sawing”, Advanced Enginering Materials V.6 No:7 (2004) 501-513.

Pei-Lum T., Bo-Huei Y., Hsing L.C., “Study on thin diamond wire slicing with Taguchi method” Materials Science Forum V.505-507 (2006) pp1219-1224.

Sheldon G.L., Finnie I., “The Mechanism of Material Removal in the Erosive Cutting of Brittle Materials” , Journal of Engineering for Industry , (Nov. 1966) pp393-400.

Telliskivi T. “Simulation of wear in a rolling –sliding contact by a semi-Winkler model and the Archard’s wear law”, Wear V.256 (2004) pp. 817-831.

Torrance, A.A., “An approximate Model of Abrasive Cutting” Wear, V.118 (1987) pp.217-232.

Verspui M.A. , With G.de, Corbijn A., Slikkerveer P.J., “ Simulation model for the erosion of brittle materials”, Wear V.233-235 (1999) pp. 436-443.

Wathaire M.D., Delaware F., Felder E., “An Upper Bound Model of Ploughing by a Pyramidal Indenter”, Wear V.616 (1981) pp.55-64.

Wei S, Kao I, “Vibration Analysis of Wire and frequency response in the modern wire saw manufacturing process”, Journal of Sound and Vibration, V. 231 No.5 (2000) pp.1383-1395.

Wei, S., Kao, I., “Analysis of Stiffness Control and Vibration of Wire in Wiresaw Manufacturing Process”, Proceeding of ASME, Manufacturing Science and Engineering Division, (1998) pp.813-818.

Williams J.A., “Wear Modelling: analytical, computatinal and mapping: a continuum mechanics approach” Wear, V.225-229 (1999) pp1-17.

Xu H.H.K., Jahanmir S., “ Microfracture and material removal in scratching of alumina”, Journal of Materials Science, Vol.30 (1995) pp.2235-2247.

Yang, F., Kao., I. “Free Abrasive Machining in slicing Brittle Materials With Wiresaw” Journal of Electronic Packaging, Vol.123 (2001) pp.254-259.

Yoffe E.H., “Elastic stress fields caused by indenting brittle materials”, Philosophical Magazine A, Vol. 46 No:4 (1982) pp.617-628.

Yoshioka, J., Hashimoto F., Miyashita , M. , Kanai, A., Abo, T., and Daito, M., “Ultra precision Grinding Technology for Brittle Materials :Application to Surface and Centerless Grinding Processes”, Milton C. Shaw Grinding Symposium, R. Komanduri , D. Maas, eds. ASME Production Engineering Division, Vol. 16 (1985) pp.209-227.

Zhu, L., Kao I, “Galerkin Based modal analysis on the vibration of wire slurry system in wafer slicing using a wiresaw”, Journal of Sound and Vibration V.283 (2005) 589-620.

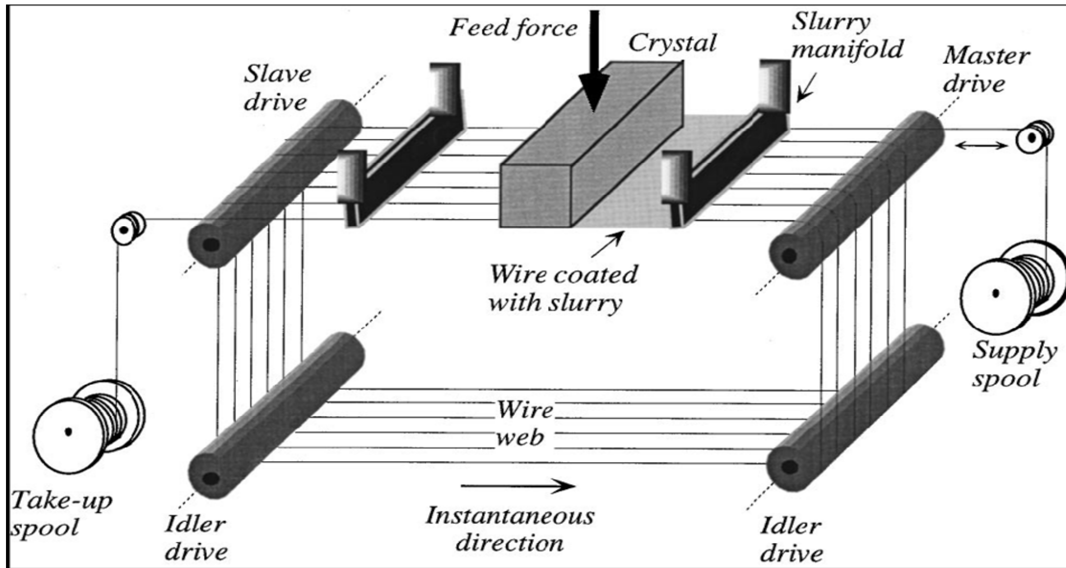


Fig. 1.1. Industrial wire saw process (Bhagavat et al. 2000).

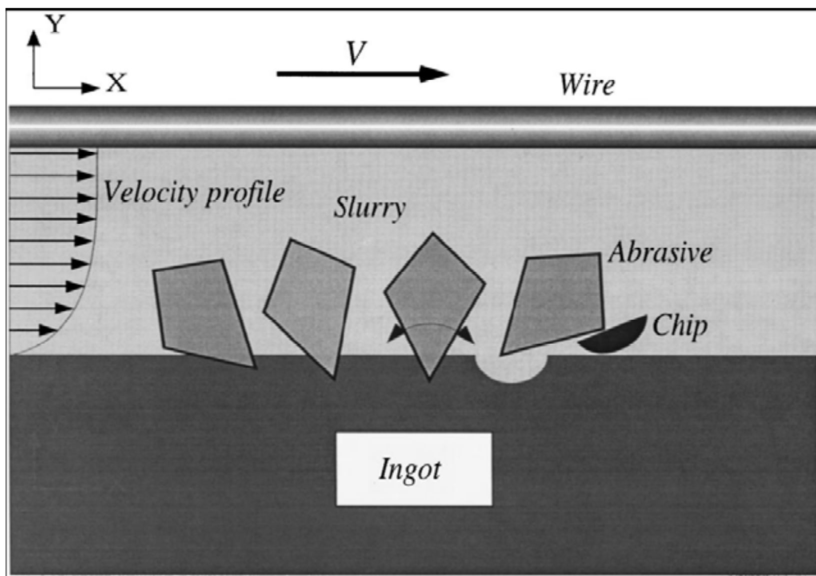


Fig. 1.2. Rolling indenting material removal in wire saw process (Bhagavat et al. 2000).

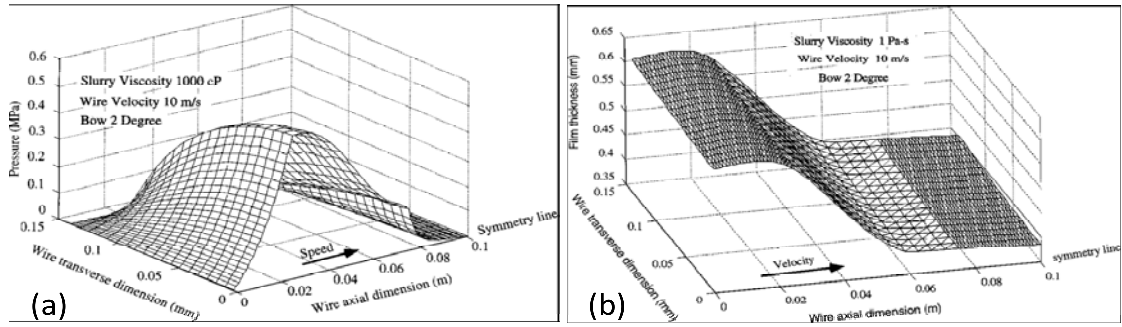


Fig. 1.3. Free abrasive wire saw process a) The slurry pressure profile b) Slurry film thickness profile (Bhagavat et al. 2000).

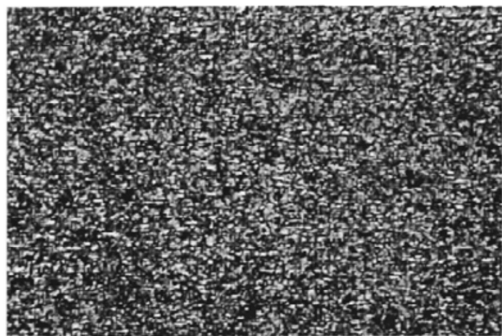

(a) surface of wiresaw sliced wafer

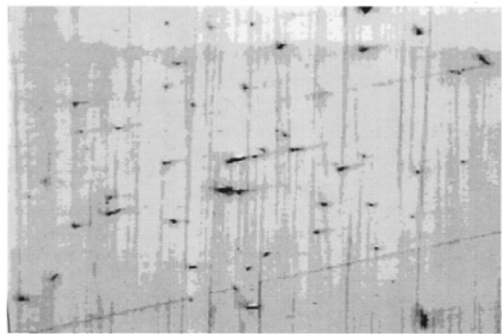

(b) surface of polished wafer

Fig. 1.4. Surfaces of a) Wire saw sliced wafer with free abrasive machining b) Polished wafer (Bhagavat et al.2000).

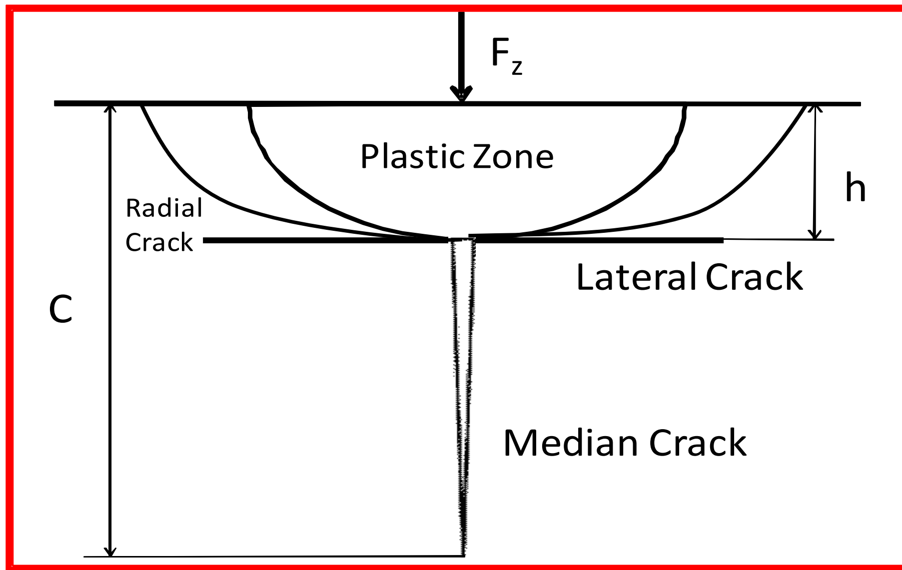


Fig. 1.5. Indentation damage in brittle materials.

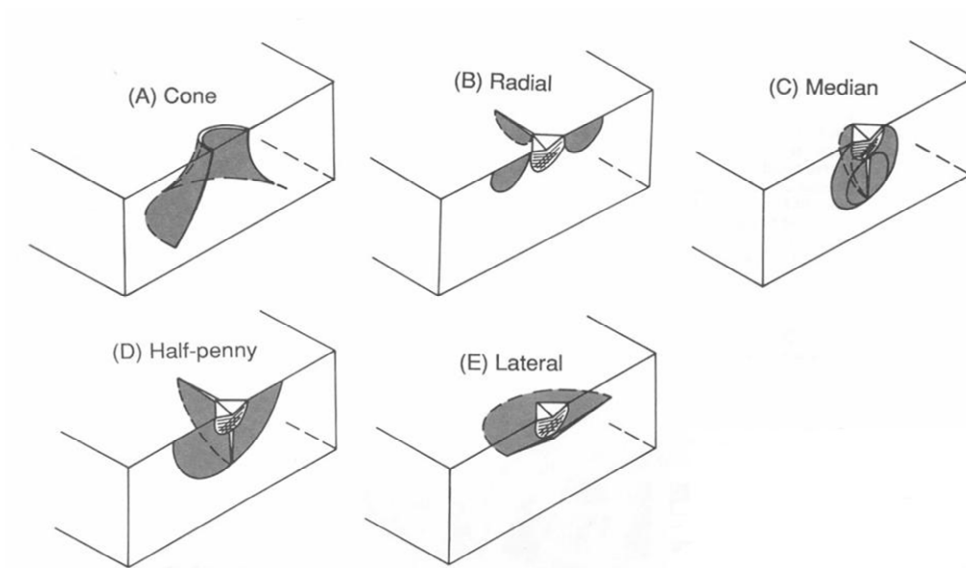


Fig. 1.6. Indentation cracks in brittle materials A) Cone crack, B) Radial crack, C) Median crack, D) Half- penny crack E) Lateral crack (Cook and Pharr 1990).

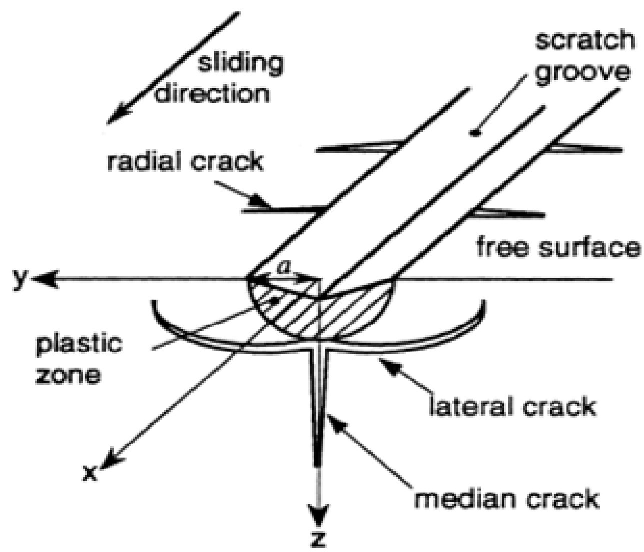


Fig. 1.7. Damage due to scratching of brittle materials (Ahn et al.1998).

# CHAPTER 2. EXPERIMENTAL PROCEDURE AND PRELIMINARY RESULTS

Wire saw experiments are conducted on alumina blocks, as a representative brittle ceramic material. The dynamic cutting forces, wire curvature, wire axial speed, $V_x$, and feed rate, $V_z$, are measured during the wire saw cutting tests. The cutting-induced surface waviness and roughness are analyzed for each combination of process parameters. Detailed scanning electron microscope (SEM) analyses are carried out to understand the variation of the machining-induced surface and sub-surface damage with the process parameters. Details of the experimental setup and the corresponding measurements for the range of the investigated process parameters are presented in this chapter.

## 2.1. Wire Saw Process, Wire Speed, and Feed Speed Measurements

A single spool to spool the wire-saw machine[1] is used in the experiments. The wire is advanced in one direction and then reversed back to 95% of its length, and this allows a 5% refresh rate of the wire per each reversal cycle. The process parameters that can be controlled are the wire-rocking angle, the wire speed, $V_x$, down feed speed, $V_z$, wire tension, $T$, and the length of wire used in one reversal of wire, $L_w$. The tension is controlled by wire tension pulleys powered by air pressure while the rocking motion is controlled by wire guide pulleys as can be seen in Fig. 2.1.

In all experiments, the following parameters have been held constant. A fixed wire length/cut cycle of 300 ft is utilized. Thus, in every forward advance of the wire, a length of $L_w$=300 ft (91.4 m) is transferred from one spool to the other. A water-based coolant (Sawzit)[2] at a ratio of 50:1 is used during cutting.

The wire axial speed is a function of spool diameter as the machine controls the speed via the angular speed of the spool. The average wire speed is calibrated via the rotational speed of the guide pulley. The rotational speed is measured by a stroboscope (model Strobex 236)[3].

[1] Millennium model wire saw machine produced by Diamond Wire Technology in Colorado, Springs.

[2] Product of Synthetic Lubricants, Inc.

[3] Product of Chadwick-Helmuth Inc., California.

For every test, twenty stroboscope measurements of the wire guide-pulley rotational speed are acquired in rev/min. The average of these measurements is multiplied by a conversion factor to obtain the speed in meters per second (m/s) as presented in Eq. 2.1. The factor in Eq. 2.1 is obtained using the diameter of the guide pulley.

$$V_x(m/s) = 0.0053 \times V_x(rev/\min) \qquad (2.1)$$

The down-feed rate $V_z$ is calibrated by tracking the position of the machine yoke relative to a stationary reference on the machine frame. As the yoke goes down, the relative position changes. The time for the yoke to travel 5 mm is measured during each test.

## 2.2. Diamond Grit-Coated Steel Wires

Four different diamond-grit-coated steel wires are used in this study. The wire diameter, $D_w$, grit size, $D_g$, and grit spacing, $L_g$, of the wires are obtained from the SEM images, utilizing the Matlab image-processing toolbox. The measured values of $D_w$, $D_g$, and $L_g$ for each wire are listed in Table 2.1. Typical SEM images of the utilized wires are presented in Fig. 2.2.

Diamond-grit-coated steel wire DWS2 has an average diameter of $D_w$=296 µm. The average abrasive diamond size is $D_g$=66 µm. The average spacing of abrasive grits is $L_g$=215 µm. The DWS2 is an old wire used in the wire-saw process. The empty places of pulled-out diamond grits can be seen in Fig. 2.2(a).

Diamond-grit-coated steel wire DWS3 is a product of Well Diamond Wire Saws Inc. The DWS3 has an average diameter of $D_w$=304 µm. The average abrasive diamond size is $D_g$=78 µm. The average spacing of abrasive grits is $L_g$=280 µm. The DWS3 is manufactured by mechanically impregnating the diamonds into the wire. The impregnation process might be successful for some grits, while others just leave an indentation mark on the wire and could not be affixed as seen in Fig. 2.2(b).

Diamond-grit-coated steel wires DWS4 and DWS5 are products of Saint-Gobain Abrasives Inc. The DWS4 and DWS5 are manufactured by nickel electroplating on steel. The grits are affixed into the electroplated nickel layer while the core remains intact as seen

in Fig. 2.3 [1]. The DWS4 and DWS5 have average diameters of $D_w$=204 μm and $D_w$=252 μm; average grit sizes of $D_g$=23 μm and $D_g$=27 μm; and average grit spacing of $L_g$=177 μm and $L_g$=69 μm, respectively. The grit spacing is higher in DWS4 than DWS5 as seen in Fig. 2.2(c)-(d).

## 2.3. Wire Bow Angle Measurements

A megapixel digital camera (Kodak Easy Share DX 7630) of 2856 × 2142 pixels is used to measure the wire bow angle. The images of the wire and sample are collected during the test and analyzed using the Matlab image-processing toolbox to obtain the wire bow angle, $\alpha$, between the wire and the effective cutting direction. A typical image obtained during a test is presented in Fig. 2.4, for the analysis of $\alpha$. The slope is at the inlet and exit of the wire; $\alpha_1$ and $\alpha_2$ are obtained. For the effective wire bow angle, $\alpha$ is their average. A total of 10 to 15 images are collected in each test, after attaining a steady state wire bow. The average of these measurements represents an average value for $\alpha$ for such test conditions. The wire bow angle $\alpha$ reaches its steady state value after a certain depth of cut and stays constant for the rest of the cut if all of the cutting parameters, including cut length, are constant. Fig. 2.5 shows a sketch of the wire inclination angles and their correlations to the wire curvature.

## 2.4. Dynamic Force Measurements

Two piezoelectric dynamic load cells (PCB- 208C01 ICP) are used to measure the dynamic cutting forces. The force sensor has a piezoelectric quartz element that converts force to electric charge. The electric charge is regulated to a current with the built-in electronics of the force sensor. The force sensors have a measurement range of 44 N for tension and compression. The force sensor's output is amplified by a two-channel-step-Amp (PCB- 482 A05 ICP) and signal conditioner. The resulting combination of force sensor and step-Amp would provide a sensitivity of 112.4 mV/N.

Two force sensors are installed orthogonal to each other using a load case. Forces in two orthogonal directions can be measured using the setup presented in Fig. 2.6. The load setup is calibrated for each direction and a calibration matrix is obtained, which is used to

convert the signal in mV to the corresponding force in N. The calibration procedure followed here is proposed by [2].

A Toshiba Tecra 700CT laptop computer is used as data logger. A dynamic data acquisition card (Data Physics: ACE FFT PC)[1] and the corresponding dynamic signal analyzer software are used to record the force signals. The system has a 50 kHz bandwidth/channel.

The forces are saved in 160 msec windows with resolution of 19.5 μsec. Multiple saves are acquired during each test and the best saves are selected for further spectral analysis by Matlab.

### 2.4.1. Calibration of Load Cell Setup

The two dimensional load cell setup calibration is presented in this section, following the procedure established by [2]**.** The aim of the calibration is to find the cross-sensitivity matrix, *S*, which relates forces to voltage as seen in Eq. 2.2. Using the inverse of *S* matrix the voltage can be related to forces as seen in Eq. 2.3. The terms of the *S* matrix can be determined as in Eqs. 2.4-7.

$$\begin{bmatrix} v_z \\ v_x \end{bmatrix} = \begin{bmatrix} S_{zz} & S_{xz} \\ S_{zx} & S_{xx} \end{bmatrix} \begin{bmatrix} Fz \\ Fx \end{bmatrix} \tag{2.2}$$

$$\begin{bmatrix} Fz \\ Fx \end{bmatrix} = \begin{bmatrix} S_{zz} & S_{xz} \\ S_{zx} & S_{xx} \end{bmatrix}^{-1} \begin{bmatrix} v_z \\ v_x \end{bmatrix} \tag{2.3}$$

$$S_{zz} = \frac{v_z(mV)}{Fz(N)} \tag{2.4}$$

[1]Produced by Data Physics Inc., (San Jose, California).

$$S_{zx} = \frac{v_x(mV)}{Fz(N)} \tag{2.5}$$

$$S_{xx} = \frac{v_x(mV)}{Fx(N)} \tag{2.6}$$

$$S_{xz} = \frac{v_z(mV)}{Fx(N)} \tag{2.7}$$

$S_{zx}$ is calculated by applying the load in the direction of vertical load cell while the voltage is measured in the horizontal load cell (LCX). In order to determine the terms of $S_{zz}$ and $S_{zx}$**,** the following procedure is applied.

Adjusting the vertical load cell (Load Cell Z, LCZ) downward, and hanging 50, 90, 130, 170, and 210 grams, the calibration test was conducted by suddenly lifting the weights, thus imposing compression to the vertical load cell (LCZ), which is vertical as seen in Fig. 2.7. Three tests are done with each weight. The $S_{zz}$ and $S_{zx}$ values for each test are calculated using Eqs.2.4-2.5. The average of the $S_{zz}$ =111 mV/N and $S_{zx}$ =1.76 mV/N are obtained.

Similar measurements are done for the horizontal load cell. The distance between the line of action of the horizontal cutting force and the axes of the horizontal load cell (LCX) is continually changing as the cut is advancing. In order to measure the variation of the cross sensitivity coefficients due to this change in distance, different calibration tests are conducted at different distances $h_w$ which is the distance between the bottom of the sample in a regular cutting test and the point of application of load. The calibration configuration is shown in Fig. 2.8. The average of $S_{xx}$ and $S_{xz}$ are presented in Table 2.2 for each $h_w$. The overall average values are $S_{xx}$=29.89 mV/N and $S_{xz}$=-129.9 mV/N. As the variation of calibration coefficients is small for different $h_w$ as seen in Table 2.2, the calibrations coefficients are taken constant.

The $S_{ij}$ values determined in Eq.2.3. can be used in obtaining dynamic forces in vertical ($F_{zd}$) and horizontal ($F_{xd}$) directions.

## 2.5. Surface Roughness Measurements and SEM Imaging

The surface roughness of the cut surfaces are measured using an optical non-contact profilometer, Zygo New View 6000, manufactured by Zygo Corporation. A 10x lens is used for the measurements. The profilometer has a resolution of depth on the order of three nanometer; the resolution in the horizontal plane is 1.1 μm, while the field of view used is 0.7x0.53 mm.

The profilometer takes continuous measurements, each having a dimension of 0.7x0.53 mm, and stitches them together into one data set. Three stitch measurements, each of 0.7x3 mm dimensions, are applied in the direction of cutting for each sample on the left–middle-right of cut surface. After the measurements are taken, the data is processed using the software MetroPro Version 8.1.5 developed by Zygo Co. A high-pass filtering is applied to remove the surface waviness. Arithmetic average deviation from the centerline (best fit plane) is obtained. The average of three measurements is taken as surface roughness, *Ra*.

A Scanning Electron Microscope (SEM) JEOL JSM-606LV is used to analyze the cutting-induced surface damage. The SEM images are taken from the lower half of the sample, on the center line of the cut surface.

## 2.6. Sample Preparation

Alumina ceramic samples having tensile strength of $\sigma_{fr}$=300 MPa, Poisson's ratio of $v$=0.22, and fracture toughness $K_{IC}$ =4 MPam$^{1/2}$ [3] are used in both roughness and waviness tests. The roughness tests are on samples with cut length $L_o$ =15~20 mm and cut height $H_s$ =7.1 mm. These samples are cut from long bars using a low-speed ceramic cutter. The samples are then cleaned with acetone and dried with air. A double-sided adhesive tape is used to affix the sample onto the load-cell assembly as shown in Fig. 2.6. The load-cell setup is covered with latex and protective materials to protect it from slurry.

The waviness tests are done with cut length, $L_o$=25 mm, and cut height, $H_s$=100 mm. The samples are affixed to an aluminum bar using crystal bond along the cut direction to reduce system vibration, as shown in Fig. 2.9.

### 2.7. Preliminary Results

The scope of this study is to investigate the role of the wire saw process parameters on the quality of the produced surfaces, as measured by the resultant surface roughness and waviness. Some typical measurements are given in this section along with the acquired experimental trends with the process parameters. The surface waviness has a wavelength of $\lambda$=20-30 mm and amplitude of 20-60 μm as seen in Fig. 2.10. The surface roughness is presented in Fig. 2.11.

The experimental results obtained from wire saw cutting of ceramics are presented in this section. Each section presents the variation of output with respect to one process parameter.

#### 2.7.1. The Effect of Wire Speed

The variation of process output with wire speed $V_x$ is presented in this section. The increase of $V_x$ decreases the wire bow angle per unit cut length, $\alpha/L_o$ as seen in Fig. 2.12. From equilibrium, the total force acting on the sample, $F_{zs}$, the corresponding average distributed load, *w,* and the average force/grit, $F_{zg}$, are given by Eqs. 2.8-10, respectively.

$$F_{zs} = 2T\sin\alpha \tag{2.8}$$

$$w = \frac{2T\sin\alpha}{L_o} \tag{2.9}$$

$$F_{zg} = \frac{2T\sin\alpha}{N} = \frac{2T\sin\alpha}{L_o} L_g \tag{2.10}$$

Here N is the number of active cutting particles within the cut length, $N=L_o/L_g$. $L_o$ is the cut length and $L_g$ is the distance between cutting grits. As $V_x$ increases, $\alpha$ decreases and thereby $w$ decreases as shown in Fig. 2.13. As $V_x$ increases, the wire bow $\alpha$ decreases and the cutting force on a single grit $F_{zg}$ decreases as in Eq. 2.10; thus, the surface roughness decreases as seen in Fig. 2.14.

### 2.7.2. The Effect of Feed Speed

The increase of feed speed $V_z$ increases wire bow $\alpha$ and the distributed load on the sample $w$ (Eq. 2.9). Experimental trends are summarized on Figs. 2.15-17. As the feed speed $V_z$ increases, the wire bow $\alpha$ increases, the total force on the sample $F_{zs}$ increases (Eq. 2.8), and the cutting force on a single grit $F_{zg}$ increases (Eq. 2.10). As a result, the surface roughness increases as seen in Fig. 2.17.

### 2.7.3. The Effect of Wire Tension

The increase of wire tension $T$ decreases the wire bow $\alpha$ as seen in Fig. 2.18. As tension $T$ increases, the wire bow $\alpha$ decreases and the distributed load on the sample $w$ remains constant due to Eq. 2.9 as seen in Fig. 2.19. The increase of tension $T$ decreases the bow angle $\alpha$ and the force on a single grit $F_{zg}$ remains constant due to Eq. 2.10; thus, the surface roughness does not change with respect to tension $T$ as seen in Fig. 2.20. The surface roughness is independent of tension.

### 2.7.4. The SEM Imaging Results

The SEM imaging showed that the dominant material removal mechanism is the trans-granular failure in which grains are cut through. Inter-granular brittle fracture is also observed. Both failure mechanisms can be seen in Fig. 2.21.

## 2.8. References

[1] Saint-Gobain Abrasives Inc., Fixed-Diamond Wire, Brochure, Form #7877, 2004.

[2] W. Che, A Study on material detachment mechanism in CMP process, M.Sc. Thesis, Iowa State University, 2002.

[3] Material Property Data, http://www.matweb.com/index.aspx, (accessed March 2008).

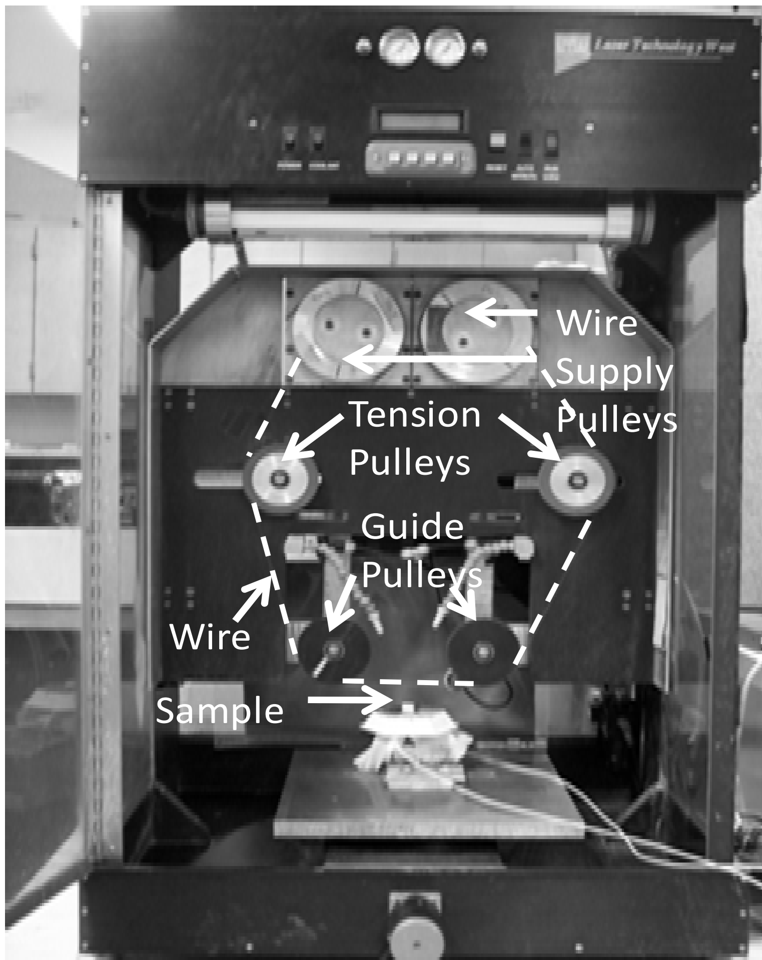


Fig. 2.1. Single wire, spool-to-spool wire saw machine (DWT Inc., Millennium Model). The wire track is marked by the dashed line.

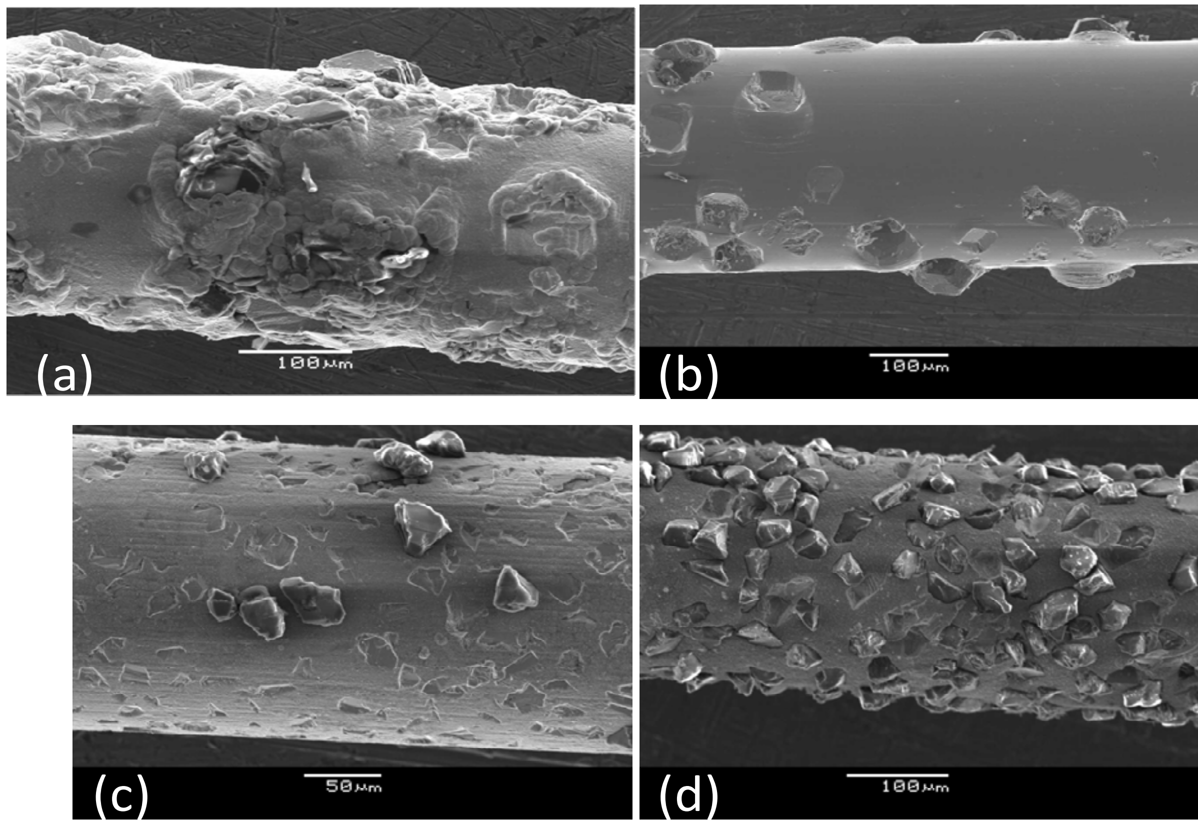


Fig. 2.2. SEM images of diamond impregnated wires a) DWS2 old wire b) DWS3 from Well Inc. c) DWS4 from Saint-Gobain Abrasives Inc. d) DWS5 from Saint-Gobain Abrasives Inc.

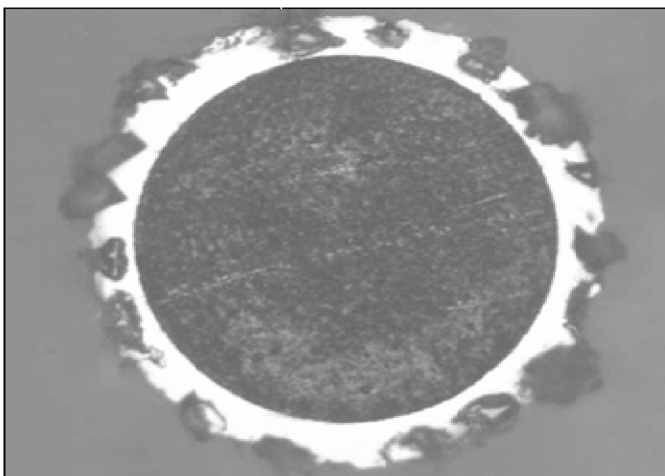

Fig. 2.3. Cross section of a typical diamond impregnated wire [1].

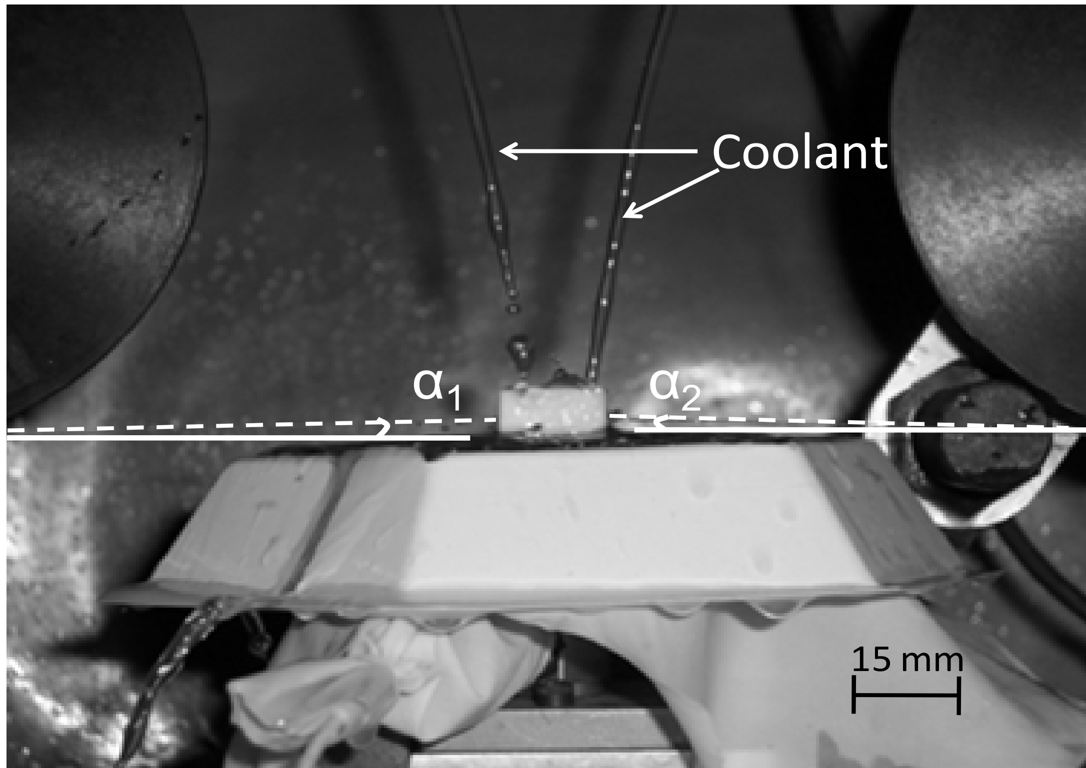


Fig. 2.4. Optical image showing the wire inclination angle with the cutting direction at the entrance and exit from the specimen.

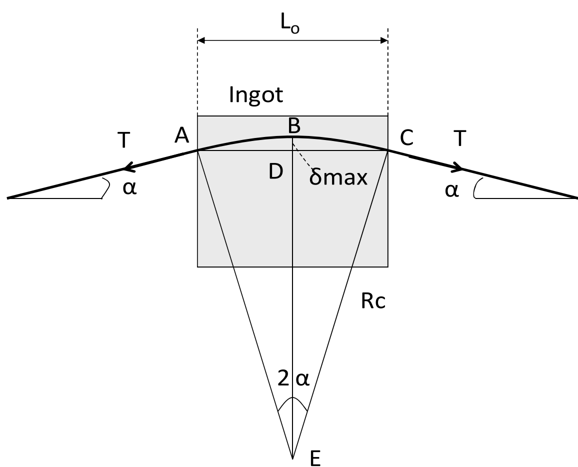


Fig. 2.5. Wire bow angle and wire curvature.

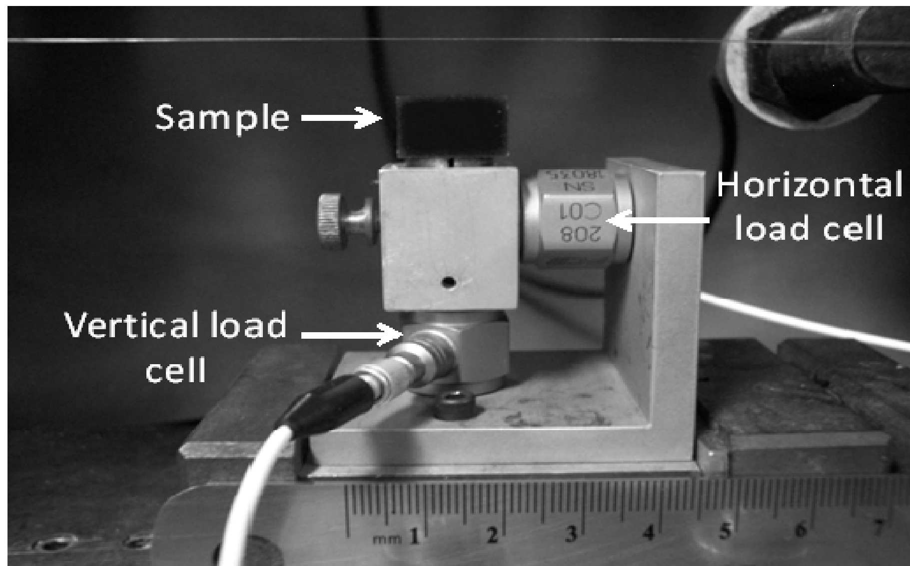


Fig. 2.6. Dynamic load cell configuration.

Fig. 2.7. Load cell calibration for the cross sensitivity matrix coefficients $S_{zz}$ and $S_{zx}$.

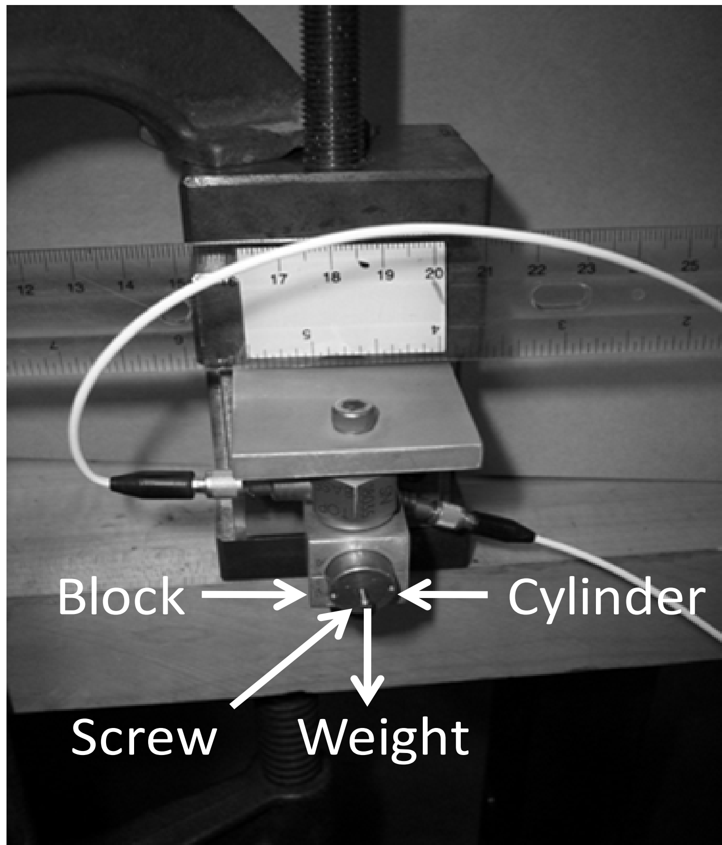


Fig. 2.8. Load cell calibration for the cross sensitivity matrix coefficients $S_{xx}$ and $S_{xz}$.

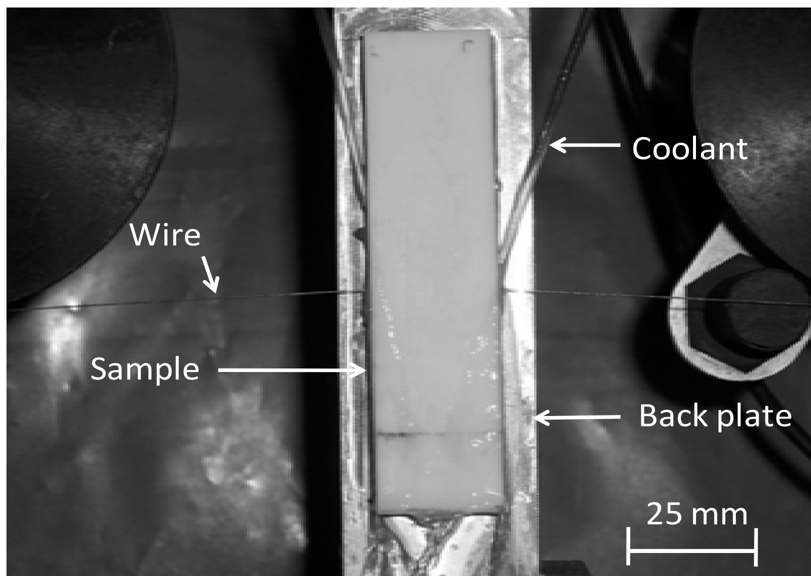


Fig. 2.9. Sample anchoring for a waviness test setup.

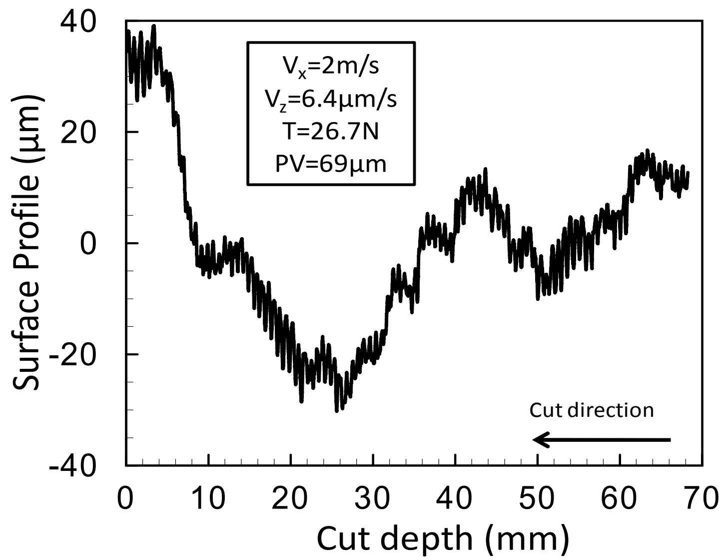


Fig. 2.10. Surface profile measurements of wire saw induced waviness.

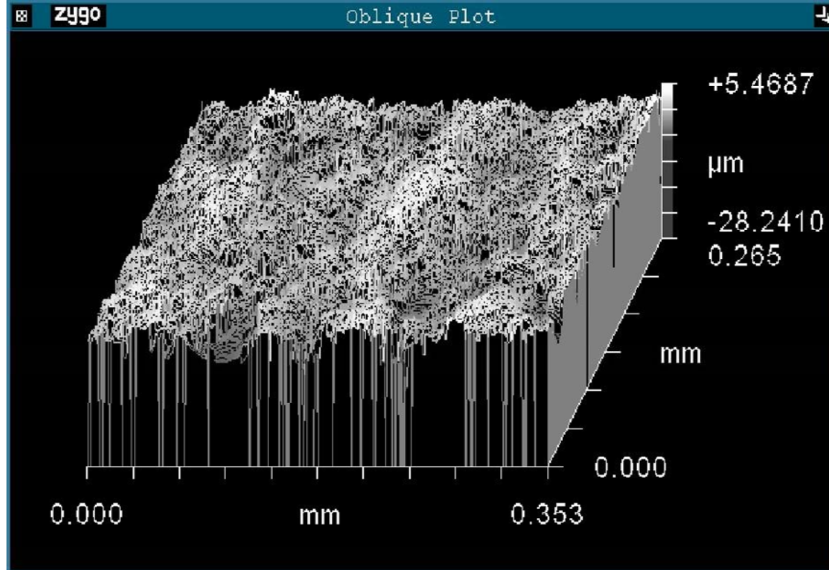


Fig. 2.11. 3D surface reconstruction showing wire saw induced roughness as measured by surface profilometer ($V_x$ =2m/s, $V_z$= 6.4 μm/sec, $T$=26.7 N).

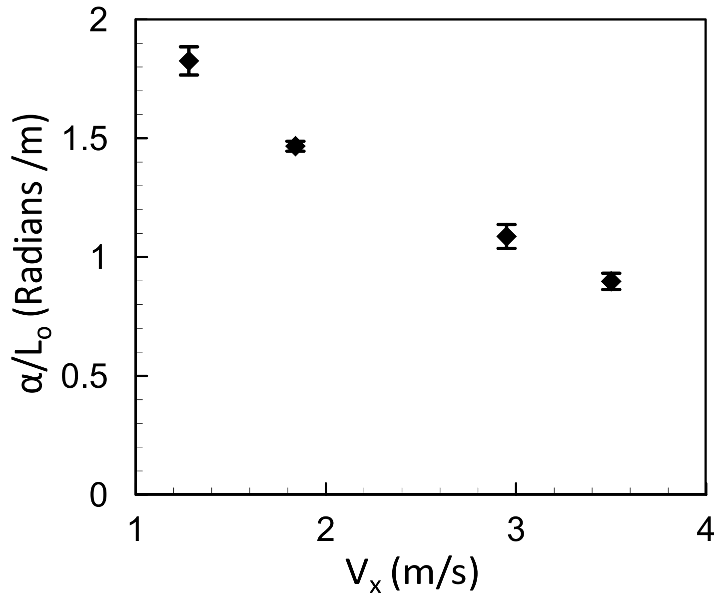


Fig. 2.12. Variation of wire bow angle per unit cut length $\alpha/L_o$ as a function of wire speed $V_x$ ($V_z$= 5 μm/sec, $T$=13 N).

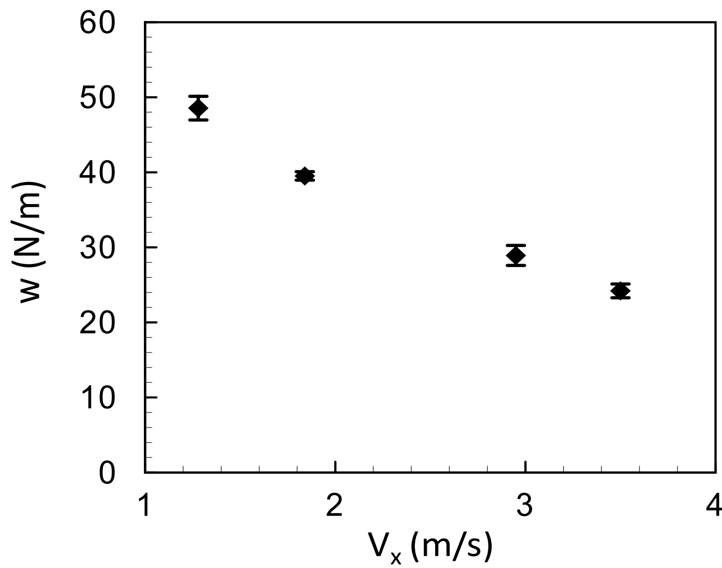


Fig. 2.13. Variation of distributed load, $w$ as a function of $V_x$ ($V_z$= 5 μm/sec, $T$=13 N).

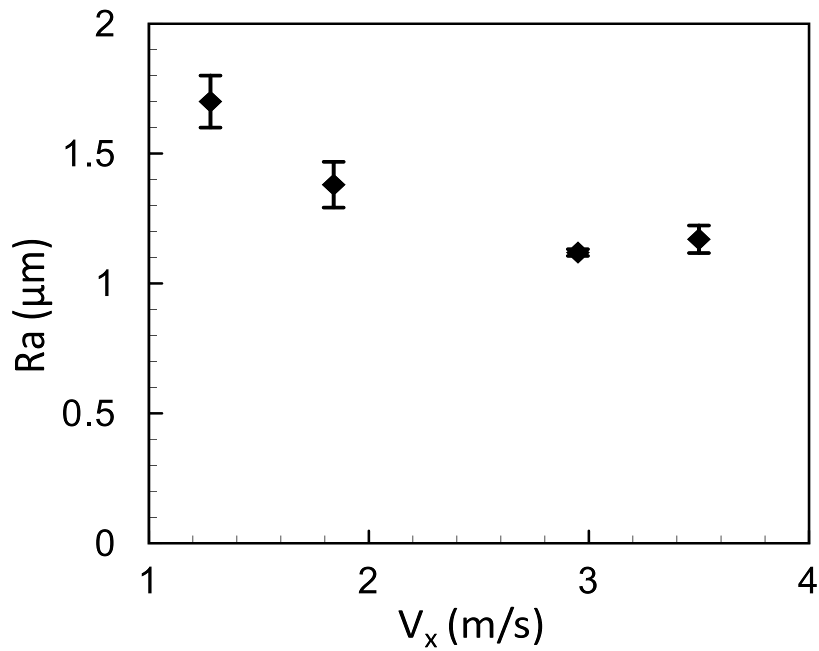


Fig. 2.14. Variation of surface roughness as a function of wire speed $V_x$ ($V_z$= 5 µm/sec, $T$=13 N).

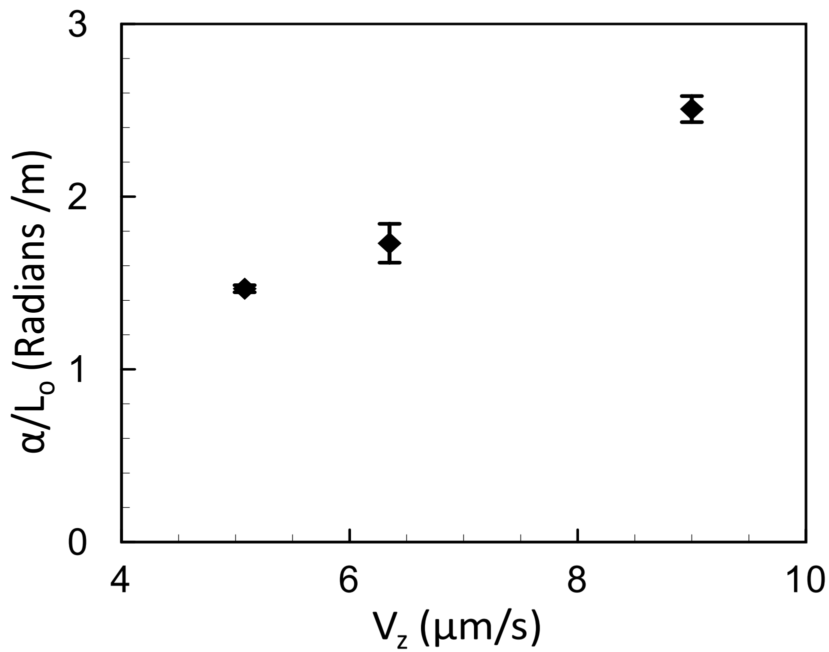


Fig. 2.15. Variation of wire bow angle per unit cut length $\alpha/L_o$ as a function of feed speed $V_z$ ($V_x$ =1.8 m/sec, $T$=13 N).

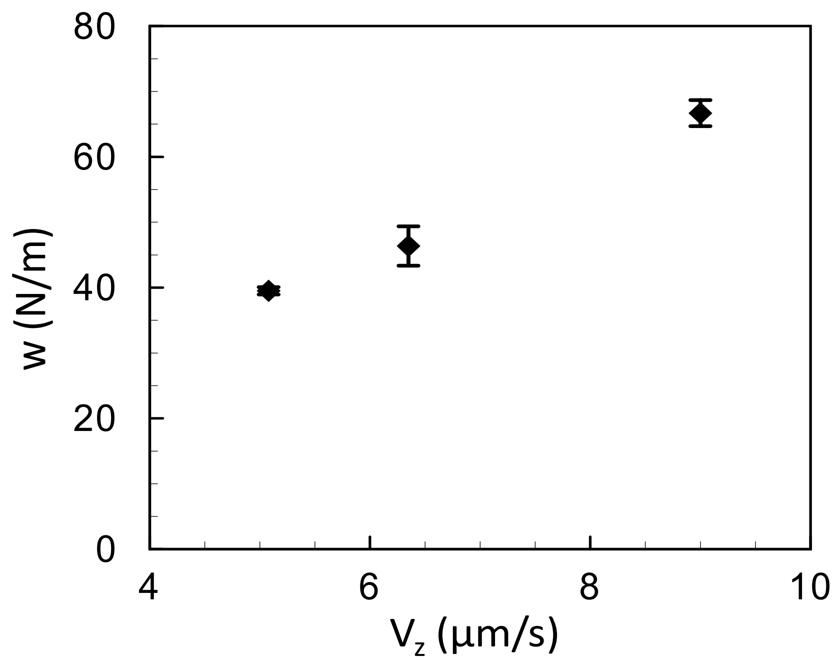


Fig. 2.16. Variation of distributed load *w* as a function of feed speed $V_z$ ($V_x$ =1.8 m/sec, *T*=13 N).

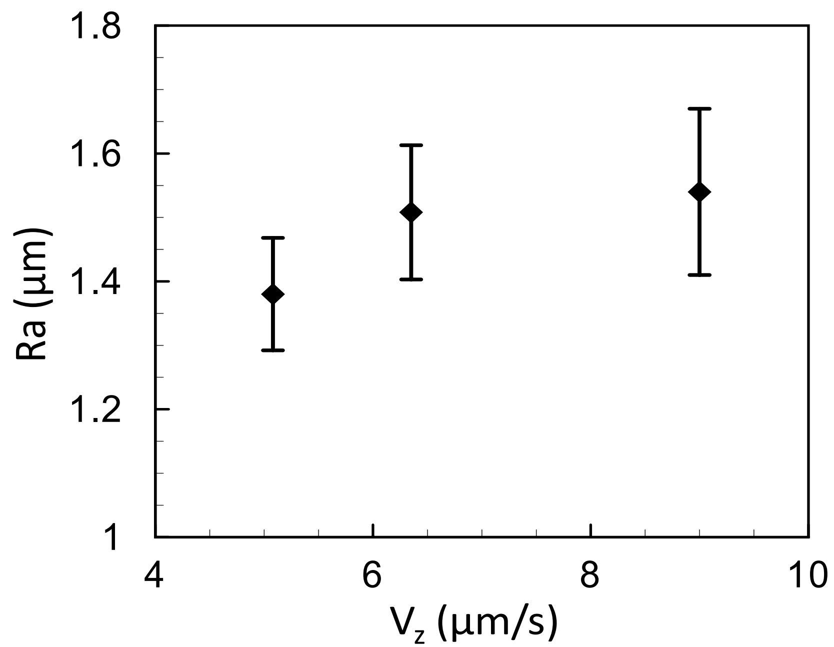


Fig. 2.17. Variation of surface roughness as a function of feed speed $V_z$ ($V_x$ =1.8 m/sec, *T*=13 N).

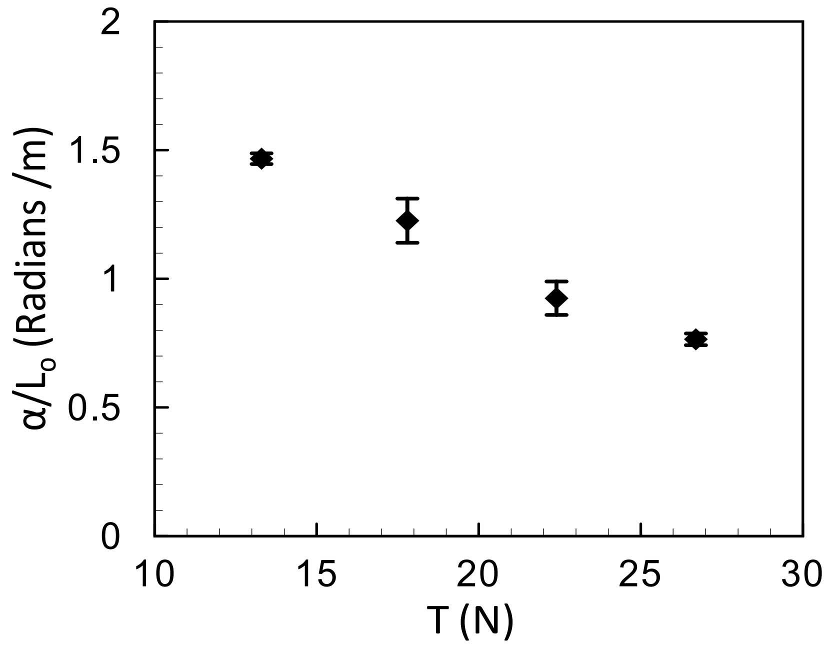


Fig. 2.18. Variation of wire bow angle per unit cut length $\alpha/L_o$ as a function of wire tension $T$ ($V_x$=1.8 m/sec, $V_z$= 5 μm/sec).

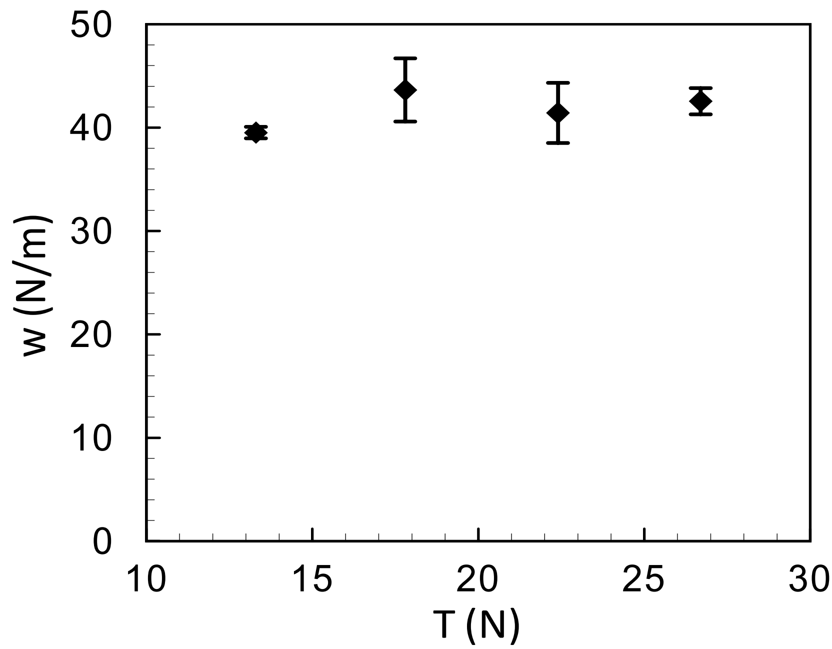


Fig. 2.19. Variation of distributed load $w$ as a function of wire tension $T$ ($V_x$=1.8 m/sec, $V_z$= 5 μm/sec).

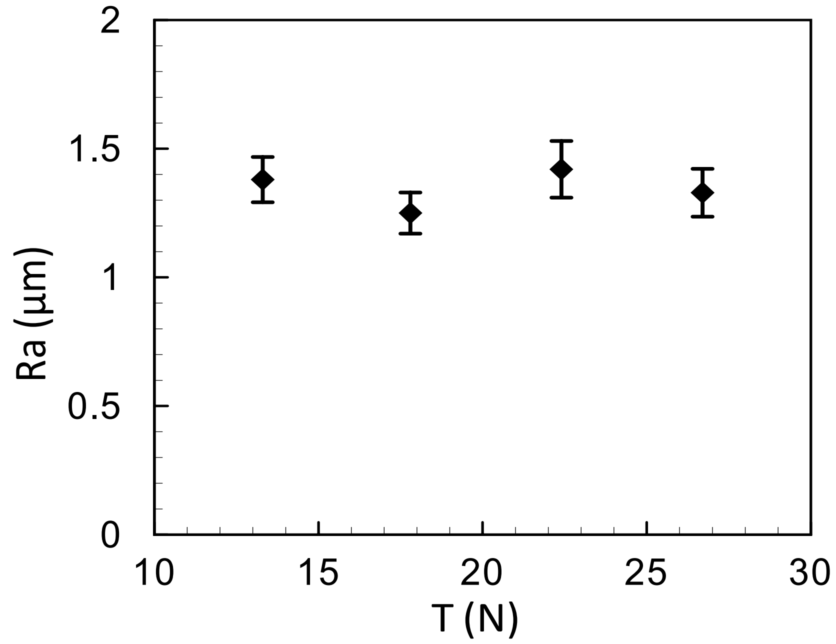


Fig. 2.20. Variation of surface roughness as a function of wire tension $T$ ($V_x$=1.8 m/sec, $V_z$= 5 μm/sec).

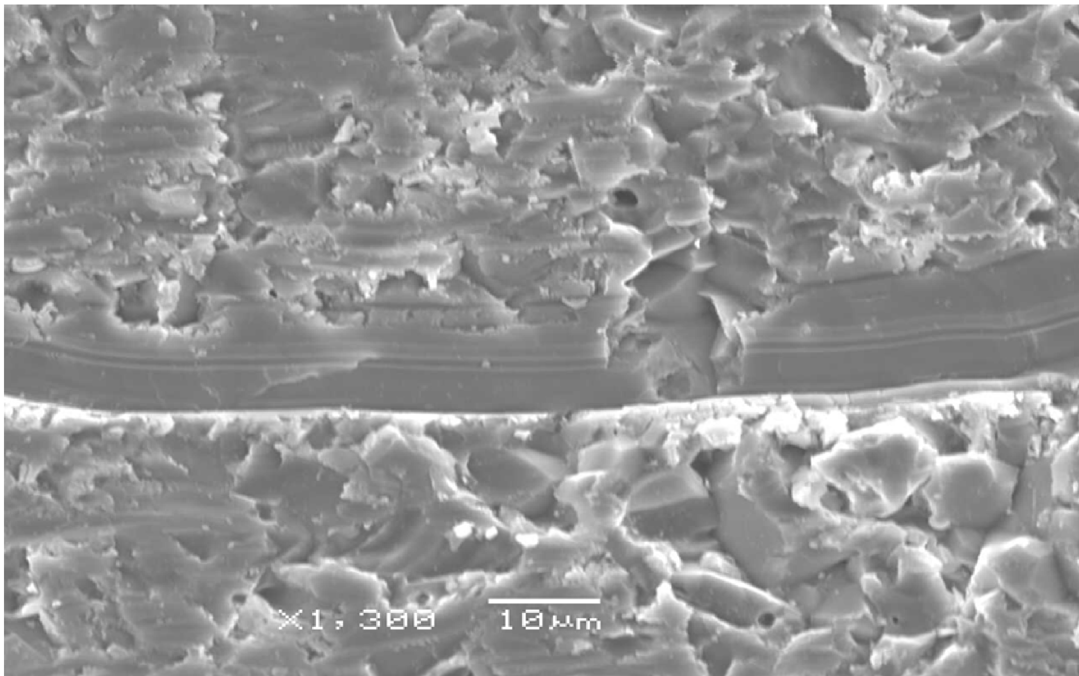


Fig. 2.21. The SEM image of a cut surface ($V_x$=1.3 m/sec, $V_z$= 5 μm/sec, $T$=13 N).

Table 2.1. Diamond impregnated wire properties.

| Wire Name | Diameter $D_w$ (µm) | STD $D_w$ (µm) | Grit Size $D_g$ (µm) | STD $D_g$ (µm) | Grit Radius R (µm) | $L_g$ Grit Spacing (µm) | STD $L_g$ (µm) | sqrt(R*$L_g$) (µm) |
|---|---|---|---|---|---|---|---|---|
| DWS2 | 296 | 10 | 66 | 21 | 33 | 215 | 69 | 84 |
| DWS3 | 304 | 3 | 78 | 9 | 39 | 280 | 117 | 104 |
| DWS4 | 204 | 1 | 23 | 3 | 11.5 | 177 | 46 | 45 |
| DWS5 | 252 | 3 | 27 | 5 | 13.5 | 69 | 18 | 31 |

Table 2.2. The cross calibration $S_{xx}$ and $S_{xz}$ values.

| hw (mm) | Averages $S_{xz}$ (mV/N) | $S_{xx}$ (mV/N) |
|---|---|---|
| 3.6 | -122.07 | 29.96 |
| 5.12 | -124.22 | 28.28 |
| 7.83 | -136.69 | 30.28 |
| 8.9 | -136.61 | 31.04 |
| average | -129.90 | 29.89 |

# CHAPTER 3. ROUGHNESS AND DAMAGE EVOLUTION DUE TO WIRE SAW PROCESS

A paper to be submitted to *The International Journal of Machine Tools & Manufacture*

**Egemen Teomete[1], Ashraf F. Bastawros[1,2], Abhijit Chandra[2,1]**
[1]Department of Aerospace Eng., [2]Department of Mechanical Eng., Iowa State University

**Abstract**

The wire saw is widely used for silicon wafer production with high yield and low surface damage. The wire saw can be used to machine brittle materials in the ductile regime where a high yield and low surface damage is desired. In this study, a damage model for the wire saw process-induced roughness damage is developed. The model is capable of predicting the damage observed in experimental work. Wire saw process design recommendations are presented for increasing the surface quality.

## 3.1. Introduction

Silicon wafers used in the solar cell and microelectronics industries can be cut from silicon crystals using inner diameter (ID) saws or wire saws. Wire saws have advantages over ID saws. These advantages are higher productivity, less wafer-surface damage, and lower kerf loss [1]. Moreover, the diameter of wafer that can be sliced by a wire saw is higher than that obtainable by an ID saw.

Wire saws are used to cut sapphire, silicon carbide, lithium niobate, wood, rock, and almost all kinds of ceramics, including foam ceramics [1, 2, 3].

Moller [4] stated that the wire saw process is responsible for 30% of the total silicon wafer-production cost, which directly affects industry. There is a need to optimize the process by developing models relating process parameters to product quality and process efficiency measures [4].

Early wire saw processes for wafer production developed in the 1990s consisted of a bare steel wire and abrasive-carrying slurry, resulting in free-abrasive machining using elasto-hydrodynamic forces [5, 6]. The abrasive particles can be SiC or diamond. The mean grit size of abrasive particles can be 5 to 30μm with a 30% to 60% volume fraction in the slurry. Average wire diameter is 180 μm, leading to a kerf loss of 200 to 250 μm. The slurry can be water based or oil based. Oil-based slurry causes the wafers to stick to each other, and it is hard to separate them, while removal of the oil from the wafer surface is another problem. Disposal of the oil-based slurry after use is also a problem. Hydrogen gas produced from the interaction of water-based slurry and silicon may cause explosions. However, from an environmental point of view, considering the high amount of slurry disposed of during the process, water-based slurries are generally preferred [4].

Clark et al. [5] stated that in order to increase the productivity and to be able to cut harder ceramics, diamond-impregnated wire, which leads to fixed-abrasive machining, was developed [5].

In wire sawing with free abrasives, wire speed is between 5 to 15 m/s and wire tension is 20 to 30 N. The feed into the ingot results in a wire bow so that the wire makes $2^o$ to $6^o$ with the horizontal [6]. In the fixed-abrasive machining wire-saw process, the wire speed is lower as material removal is not occurring by hydrodynamic action.

In multi-wire technology, a single wire is winded to a tension control unit and four guide pulleys, which are grooved with constant pitch. Five to seven hundred parallel wires run together and are collected at a take-up spool. The ingot is sliced into hundreds of wafers as it is fed into the wire web. The wafers in solar-cell industry are cut by running the wire in only one direction at a high speed between 5 to 20 m/s, while the wafers in the micro electronics industry are cut by running the wire in both directions with a lower speed (oscillating the wire from one spool to another) [4].

Literature on wire saw research has been ongoing in three main areas: material removal mechanisms, kinematics of wire, and parametric studies between the process inputs and outputs.

Li et al. [7] presented the stresses under an abrasive particle, which is rolling and indenting in a wire saw process. Material removal mechanisms for free-abrasive machining

were developed using fracture mechanics and hydrodynamic behavior of slurry by Moller [4]. The material removal rate is defined as a function of power supplied to the abrasive by hydrodynamic effect and the hydrodynamic film properties are calculated using the finite element method which couples Reynold's equation of hydrodynamics with the elasticity equation of wire [6]. Liu et al. [8] stated that the material removal mechanism of bead-impregnated wire-saw cutting of rock is a Hertzian type fracture in which the fracture occurs due to the tensile field behind the sliding bead.

Wei and Kao [9] worked on stiffness analyses of straight and bowed wires under tension. Vibration characteristics of wire with respect to wire speed, tension, and slurry viscosity was investigated. The increase of wire tension and slurry viscosity decreases vibration amplitude and kerf loss, while the wire speed has almost no affect when it is below 25 m/s, [1, 10].

Process monitoring of the wire saw process for forces, wire speed, feed rate, wire bow, and wire tension was developed by Clark et al. [5]. Parametric studies relating process parameters to forces, and surface roughness and wire wear for cutting foam ceramics and wood were conducted by Clark et al. [2]. Hardin et al. [11] conducted a parametric study for slicing single crystal SiC with a fixed-abrasive diamond wire, relating wire speed, rocking frequency, and down-feed rate with surface and subsurface damage. Closed-loop diamond-impregnated wire saw cutting of $Al_2O_3$ and TiC ceramics showed that cutting forces, surface roughness, and wire wear decreases as the wire speed is increased, while higher feed rate increases the cutting forces, surface roughness, and wire wear [12].

Hardness anisotropy of Lithium Niobate wafers has been investigated using nano-indentation [13]. Bhagavat and Kao [14] determined the direction of approach for three most commonly sliced orientations of silicon considering crystal anisotropy.

Damage evolution due to wire sawing of silicon wafers is of significant interest as the photovoltaic and semiconductor industries have strict tolerances for surface quality. The process-induced damage on brittle materials can be modeled starting with existing damage models of indentation of brittle materials. There exist several models for the failure mechanisms in brittle materials due to indentation [15-20].

Ductile regime grinding of brittle materials has been investigated experimentally by different researchers [21-26]. Bifano et al. [22] stated that when the feed is decreased below a certain amount in grinding, a transition of wear mechanism from brittle to ductile mode can be achieved.

In this study, a damage model for wire saw process induced roughness damage is developed. The damage model is based on ductile mode material removal and brittle mode damage, as observed in SEM images of cut surfaces. The damage model predicts the experimentally measured damage successfully. The experimental work is presented in section 3.2. The model is presented in section 3.3. The results and discussion of the study are presented in section 3.4. The conclusions are presented in section 3.5.

### 3.2. Experimental Process

Wire saw experiments are conducted on alumina ceramic. The wire bow angle, wire axial speed, $V_x$ and feed rate, $V_z$ are measured during the wire saw cutting tests. The surface roughness of cut surfaces is also measured. The SEM imaging of cut surfaces is obtained. The equipment used in these measurements and the process parameters are presented in this section.

#### 3.2.1. Wire Saw Cutting and Wire Bow Angle Measurement

A wire saw machine[1] is used in the experiments. This spool-to-spool wire saw machine with rocking motion of the wire can be controlled by the wire speed, $V_x$, down-feed speed, $V_z$, and wire tension, $T$. The tension is controlled by wire tension pulleys powered by air pressure, while the rocking motion is controlled by wire guide pulleys as can be seen in Fig. 3.1. The cut length of wire, which is used during the cutting, is 300 ft (91.4 m). Thus, at every direction reversal, 300 ft of wire is transferred from one spool to the other.

The wire speed is a function of spool diameter as the machine controls the speed via the angular frequency of the spool.

[1] Millennium model wire saw machine produced by Diamond Wire Technology in Colorado, Springs.

In order to get the actual average speeds, a Strobex Systems 236 model stroboscope[2] is used. The down-feed speed, $V_z$, is measured by tracking the position of a grid, which is on the yoke of the machine, with respect to a stationary point on the frame of the machine. As the yoke goes down, the grid moves relative to the fixed point on the frame of the machine. The time to travel 5 mm grids is measured during the tests.

A water-based coolant-to-lubricant Sawzit[3] ratio of 50/1 is used during cutting tests.

Four different diamond grit coated steel wires are used in the wire saw experiments. The wire diameter ($D_w$), grit size ($D_g$), and grit spacing ($L_g$) information is obtained from SEM images of the wires and the average values are presented at Table. 3.1. The DWS2 is an old wire, which was used in the wire-saw process. The empty places of pulled-out diamond grits can be seen in Fig. 3.2 (a). The average half-included angle of the grits on DWS2 is $\psi$=71$^o$. The diamond-grit-coated steel wire DWS3 is a product of Well Diamond Wire Saws Inc. The DWS3 is manufactured by mechanically impregnating the diamonds into the steel wire. The impregnation process might be successful for some grits, while others just leave an indentation mark on the wire and could not be affixed as seen in Fig. 3.2 (b). Diamond-grit-coated steel wires DWS4 and DWS5 are products of Saint-Gobain Abrasives Inc. The DWS4 and DWS5 are manufactured by nickel electroplating on steel. The grits are affixed into the electroplated nickel layer, while the core remains intact. The grit spacing is higher in DWS4 than in DWS5 as seen in Fig. 3.2 (c)-(d).

Alumina ceramic samples having tensile strength of $\sigma_{fr}$=300 MPa, Poisson's ratio of $v$=0.22, fracture toughness $K_{IC}$ =4 MPam$^{1/2}$, Young's modulus of $E$=370 GPa [27], and hardness of $H$=22 GPa [20] are used in the cutting tests. The cut length of the samples is between $L_o$ =15~20 mm and the height is $H_s$ =7.1 mm. A group of tests are done with DWS2 with the wire speed varied over $V_x$=1.3, 1.8, 2.95, 3.5 m/s, the wire tension varied over $T$=13.3, 17.8, 22.4, 26.7 N, and the down feed varied over $V_z$=5, 6.35, 10.16 µm/sec. In order to explore the effect of different wires' characteristics on surface quality, twelve tests are done with process parameters $V_x$=1.35, 2, 3, 4 m/s, $V_z$=6.35 µm/sec, and T=13.3 N using the wires DWS3, DWS4, and DWS5; four tests are conducted with each wire.

[2] Product of Chadwick-Helmuth Inc., California.

[3] Product of Synthetic Lubricants, Inc.

A megapixel digital camera (Kodak Easy Share DX 7630) of 2856 × 2142 pixels is used to measure the wire bow angle seen in Fig. 3.3. The images of the wire and sample are collected during the test and analyzed using Matlab (Mathworks) to obtain the angle $\alpha$ between the wire and the horizontal. The average of the steady state wire bow angles, $\alpha$, is attained to the test as the steady state wire bow angle of that test.

### 3.2.2. Surface Roughness Measurements and SEM imaging

The surface roughness of the cut surfaces are measured by using an optical non-contact profilometer, Zygo New View 6000, manufactured by Zygo Corporation. A 10x lens is used for the measurements. The profilometer has a vertical resolution on the order of 3 nanometer; the resolution in the horizontal plane is 1.1 μm, while the field of view used is 0.7×0.53 mm.

In a stitch measurement, the profilometer takes continuous measurements each 0.7×0.53 mm and stitches them together into one data set. Three stitch measurements, each of 0.7×3 mm dimensions, are applied in the direction of cutting for each sample on the left-middle-right of the cut surface. After the measurements are taken, the data is processed using the software MetroPro Version 8.1.5 developed by Zygo Co. A high pass filtering is applied to remove the surface waviness. Arithmetic average deviation from the centerline (best fit plane) is obtained. The average of three measurements is taken as surface roughness (*Ra*) of the test.

A Scanning Electron Microscope (SEM), JEOL JSM-606LV, is used to image the cut-surface topology. The SEM images are taken from the lower half of the sample, on the center line of the cut surface. It is seen from the images that there are two material removal mechanisms in affect. The dominant mechanism is the trans-granular failure in which grains are cut through. Inter-granular failure, in which grain boundary failure results in grain dislodgement in a brittle mode, is also observed. Both failure mechanisms can be seen in Fig. 3.4.

### 3.3. Roughness Model Derivation

Ductile material removal and brittle fracture is observed in SEM images. The proposed model is shown in Fig. 3.5. The material removal occurs in a ductile mode as seen in SEM images, while the damage occurs due to median cracking as in Fig. 3.5. As discussed by Evans and Marshall [15], removal of plastically deformed material in the cutting zone reduces residual stress. This reduces the tendency of lateral crack formation in brittle materials. The median crack depth, *c*, can be compared to measured roughness.

Fu et al. [28] derived the force on a single grit in ductile mode material removal as presented in Eq. 3.1**,** where $\sigma_y$ is yield stress, *R* is cutting particle radius, and *h* is cut depth for a single particle.

$$F_z = F_{zg} = \pi \sigma_y R h \qquad (3.1)$$

The mass continuity of the cutting process gives us Eq. 3.2.

$$V_z = \frac{d}{dt}\left(\frac{Volume}{A_p}\right) = \frac{d}{dt}\left(\frac{\frac{L_o}{L_g} \times D \times h \times S}{L_o \times D}\right) = \frac{dS}{dt}\left(\frac{h}{L_g}\right) = V_x\left(\frac{h}{L_g}\right) \qquad (3.2)$$

Volume is the total amount of material removed, $A_p$ is the projected area of the cut trench, $L_o$ is the cut length of sample, $L_g$ is the distance between cutting particles, *D* is width of cut trench that can be taken as diameter of wire, *S* is sliding distance, $V_x$ is the axial speed of wire, and $V_z$ is the feed of wire. Solving the cut depth *h* from Eq. 3.2 yields Eq. 3.3.

$$h = L_g \times \frac{V_z}{V_x} \quad (3.3)$$

The force on a single grit, $F_{zg}$, can be obtained in terms of process parameters by inserting Eq. 3.3 into Eq. 3.1 and Eq. 3.4 is obtained.

$$F_{zg} = \pi \sigma_y R L_g \times \frac{V_z}{V_x} \quad (3.4)$$

The damage resulting from wire saw cutting is correlated with median crack depth. Lawn et al. [16] derived the median crack length using fracture mechanics principles. The median crack length is presented in Eq. 3.5. Lawn et al. [16] calibrated the indentation coefficients 0.032 and 0.017 in Eq. 3.5 using indentation data of soda-lime glass and noted that they are applicable to all brittle materials.

$$c = \left[ \left[ 0.032 + 0.017 \times (\cot\psi)^{\frac{2}{3}} \left( \frac{E}{H} \right)^{\frac{1}{2}} \right] \frac{P}{K_c} \right]^{\frac{2}{3}} \quad (3.5)$$

Inserting Eq. 3.4 in place of $P = F_{zg}$ in Eq. 3.5 gives us Eq. 3.6.

$$c = \left[ \left[ 0.032 + 0.017 \times (\cot\psi)^{\frac{2}{3}} \left( \frac{E}{H} \right)^{\frac{1}{2}} \right] \frac{\pi \sigma_y R L_g}{K_c} \right]^{\frac{2}{3}} \left[ \frac{V_z}{V_x} \right]^{\frac{2}{3}} \qquad (3.6)$$

The median crack depth, which is the damage due to the wire saw process, is presented in terms of the process parameters in Eq. 3.6. The damage is a function of the half of the included angle of the grits, $\psi$; the modulus of elasticity of ingot, $E$; the hardness of the ingot, $H$; the fracture toughness of the ingot, $K_c$; and wire properties, feed speed, and wire speed.

### 3.4. Results and Discussion

Decreasing feed rate in grinding below a threshold yields ductile regime grinding of brittle materials [21-26]. In ductile regime machining of brittle materials, the material removal takes place with plastic deformation of the grains [21, 22, 24-26]. While the material removal is in ductile mode, brittle fracture is still observed in ductile regime grinding [22, 26]. The material removal and damage formation in the wire saw process is analogous to ductile regime grinding as seen from SEM images of wire saw processed surfaces. A damage model is derived for roughness damage induced by wire saw process. The model is compared to experimental data in Fig. 3.6. The model has a good performance in predicting roughness damage due to the wire saw process.

The damage model states that if the feed-speed-to-wire-speed ratio ($V_z/V_x$) is increased, the roughness damage will increase, while if this ratio is kept constant, roughness damage will be constant. The two experiments marked in Fig. 3.6 have different feed speeds and wire speeds but a very close ($V_z/V_x$) ratio, and their roughnesses are also very close to each other. In a wire saw process, if efficiency should be increased by increasing the feed speed, in order to keep the level of damage constant, the wire speed should be increased proportionally to the feed speed.

In order to explain the effect of wire tension on roughness damage, the change of forces with wire tension should be considered. The total force and distributed force acting on the sample by the wire due to wire bow and tension is presented in Eq. 3.7 and Eq. 3.8, respectively. The total force, $F_{zs}$, is distributed on the cutting grits as cutting forces per grit, $F_{zg}$, by Eq. 3.9. The $N=L_o/L_g$ is the number of cutting particles in the cut length, $L_o$, and, $L_g$, is the distance between cutting grits.

$$F_{zs} = 2T\sin\alpha \tag{3.7}$$

$$w = \frac{2T\sin\alpha}{L_o} \tag{3.8}$$

$$F_{zg} = \frac{2T\sin\alpha}{N} = \frac{2T\sin\alpha}{L_o} L_g \tag{3.9}$$

The increase of wire tension, $T$, decreases the wire bow $\alpha$ as seen in Fig. 3.7. As tension, $T$, increases, the wire bow $\alpha$ decreases and the distributed load on the sample $w$, remains constant due to Eq. 3.8, as seen in Fig. 3.8. The increase of tension, $T$, decreases the bow angle $\alpha$ and the force on a single grit, $F_{zg}$, remains constant due to Eq. 3.9; thus, the surface roughness does not change with respect to tension, $T$, as seen in Fig. 3.9. The surface roughness damage is independent of tension.

The damage model relates the roughness damage with wire properties approximately, as in Eq. 3.10. The roughness is expected to increase with the increase in the radius, $R$, of abrasive grits and the spacing between the abrasive grits, $L_g$.

$$c \sim \left(R \times L_g\right)^{\frac{2}{3}} \tag{3.10}$$

Four roughness tests with different wire speeds but the same feed speeds and tensions are done with each of the last three wires in Table 3.1. The roughness versus wire speed for

each wire is presented in Fig. 3.10. For the same wire speed, the increase of $(R.L_g)^{0.6}$ yields a higher roughness as seen in Fig. 3.10. Thus, the prediction of the model about the increase of roughness with grit radius and spacing is verified experimentally.

### 3.5. Conclusion

Experimental work on the wire saw process has been conducted with different process parameters. The SEM images of the cut surfaces showed that the materials removal is in ductile mode, while there is brittle fracture, which is analogous to ductile regime grinding of brittle materials. A roughness damage model is derived. The derived model is validated with experimental study. The model states that the roughness damage is proportional to feed speed to wire speed ratio. If the efficiency of the process should be increased without increasing the roughness damage, the feed speed should be increased proportionally with respect to wire speed. The wire properties have a marked effect on the roughness damage. Wires with smaller grit radius and spacing will lead to smaller roughness damage. High grit density wires with small grits are beneficial for surface quality.

### 3.6. Acknowledgement

This work is supported by US-National Science Foundation NSF through grant No. DMII-0355536.

### 3.7. References

[1] L. Zhu, I. Kao, Galerkin Based modal analysis on the vibration of wire-slurry system in wafer slicing using a wiresaw, Journal of Sound and Vibration 283 (2005) 589-620.

[2] W.I. Clark, A.J. Shih, C.W. Hardin, R.L. Lemaster, S.B. McSpadden, Fixed abrasive diamond wire machining – Part II: experiment design and results, International Journal of Machine Tools and Manufacture 43 (2003) 533-542.

[3] P.Q. Ge, L. Zhang, W. Gao, Z.C. Liu, Development of endless diamond wiresaw and sawing experiments, Materials Science Forum 471-472 (2004) 481-484.

[4] J.H. Moller, Basic mechanisms and models of multi–wire sawing, Advanced Engineering Materials 6 7 (2004) 501-513.

[5] W.I. Clark, A.J. Shih, C.W. Hardin, R.L. Lemaster, S.B. McSpadden, Fixed abrasive diamond wire machining – Part I: process monitoring and wire tension force, International Journal of Machine Tools and Manufacture, 43 (2003) 523-532.

[6] M. Bhagavat,V. Prasad, I. Kao, Elasto-hydrodynamic interaction in the free abrasive wafer slicing using a wiresaw: modeling and finite element analysis, Transactions of ASME, Tribology Division, 122 (April 2000) 394-404.

[7] J. Li, I. Kao., V. Prasad, Modeling stresses of contacts in wiresaw slicing of polycrystalline and crystalline ingots: application to silicon wafer production, Journal of Electronic Packaging, ASME, 120 (June 1998) 123-127.

[8] B.C. Liu, Z.P. Zhang, Y.H. Sun, Sawing trajectory and mechanism of diamond wire saw, Key Engineering Materials, 259-260 (2004) 395-400.

[9] S. Wei, I. Kao, Analysis of stiffness control and vibration of wire in wiresaw manufacturing process, Proceeding of ASME, Manufacturing Science and Engineering Division, (1998) 813-818.

[10] S. Wei, I. Kao, Vibration analysis of wire and frequency response in the modern wire saw manufacturing process, Journal of Sound and Vibration, 231 (5) (2000) 1383-1395.

[11] C.W. Hardin, J. Qu, A.J. Shih, Fixed abrasive diamond wire saw slicing of single-crystal silicon carbide wafers, Materials and Manufacturing Processes, 19 (2) (2004) 355-367.

[12] J.F. Meng, J.F. Li, P.Q. Ge, R. Zhou, Research on endless wire saw cutting of $Al_2O_3$/TiC Ceramics, Key Engineering Materials 315-316 (July 2006) 571-574.

[13] S. Bhagavat, I. Kao, Nano indentation of lithium niobate : hardness anisotropy and pop-in phenomenon, Materials Science and Engineering A 393 (2005) 327-331.

[14] S. Bhagavat, I. Kao, Theoretical analysis on the effects of crystal anisotropy on wiresawing process and application to wafer slicing, Machine Tool and Manufacture 46 (2006) 531-541.

[15] A.G. Evans, D.B. Marshall, Wear mechanisms in ceramics, Fundamentals of Friction and Wear of Materials, ASM Materials Science Seminar, Pennsylvania , 1980, pp.439-449.

[16] B.R. Lawn, A.G. Evans, D.B. Marshall, Elastic/plastic indentation damage in ceramics: the median/radial crack system, Journal of the American Ceramic Society, 63 (9-10) (1980) 574-581.

[17] D.B. Marshall, B.R. Lawn, A.G. Evans, Elastic/plastic indentation damage in ceramics: the lateral crack system, Journal of the American Ceramic Society, 65 (11) (1982) 561-566.

[18] S.S. Chiang, D.B. Marshall, A.G. Evans, The response of solids to elastic /plastic indentation. I. Stresses and residual stresses, Journal of Applied Physics, 53 (1) (1982) 298-311.

[19] S.S. Chiang, D.B. Marshall, A.G. Evans, The response of solids to elastic /plastic indentation. II. Fracture initiation, Journal of Applied Physics, 53 (1) (1982) 312-317.

[20] R.F. Cook, G.M. Pharr, Direct observation and analysis of indentation cracking in glasses and ceramics, Journal of American Ceramic Society, 73 (4) (1990) 787-817.

[21] J. Yoshioka, F. Hashimoto, M. Miyashita, A. Kanai, T. Abo, M. Daito, Ultraprecision grinding technology for brittle materials: application to surface and centerless grinding processes, Milton C. Shaw Grinding Symposium, R. Komanduri, D. Maas, eds. ASME Production Engineering Division, 16 (1985) pp.209-227.

[22] T.G. Bifano, T.A. Dow, R.O. Scattergood, Ductile-regime grinding: a new technology for machining brittle materials, Journal of Engineering for Industry, 113 (1991) 184-189.

[23] H.T. Young, H.T. Liao, H.Y. Huang, Novel method to investigate the critical depth of cut of ground silicon wafer, Journal of Materials Processing Technology 182 (2007) 157–162.

[24] B. K. A. Ngoi, P. S. Sreejith, Ductile regime finish machining – a review, International Journal of Advanced Manufacturing Technology 16 (2000) 547–550.

[25] L. Yin, A.C. Spowage, K. Ramesh, H. Huang, J.P. Pickering, E.Y.J. Vancoille, Influence of microstructure on ultraprecision grinding of cemented carbides, International Journal of Machine Tools & Manufacture 44 (2004) 533–543.

[26] J.D. Kim, S.R. Nam, Ductile regime grinding of ferrite with variation of grain size by a piezoelectric-driven micropositioning grinding table, Proc. Instn Mech Engrs Part B, 211 (1997) 487-493.

[27] Material Property Data, http://www.matweb.com/index.aspx, (accessed March 2008).

[28] G. Fu, A. Chandra, S. Guha, G. Subhash, A plasticity based model of material removal in chemical-mechanical polishing (CMP), IEEE Transactions on Semiconductor Manufacturing, 14 (4) (2001) 406-417.

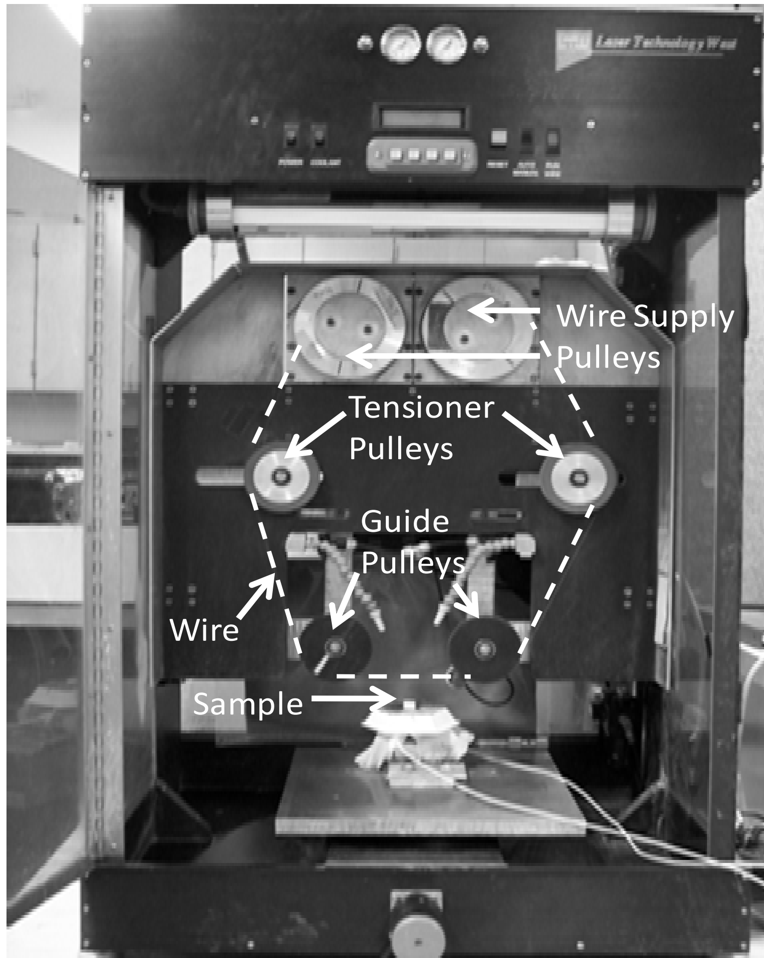


Fig. 3.1. Single wire, spool-to-spool wire saw machine (DWT Inc., Millennium Model). The wire track is marked by the dashed line.

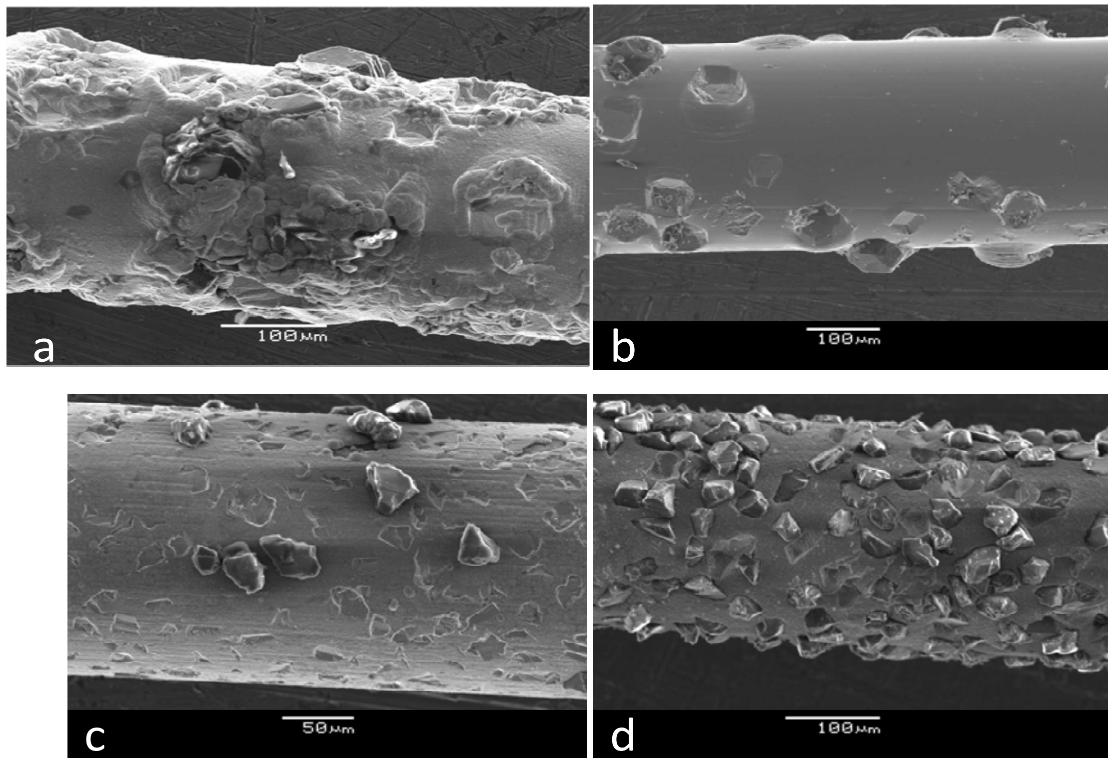


Fig. 3.2. SEM images of diamond impregnated wires a) DWS2 old wire b) DWS3 from Well Inc. c) DWS4 from Saint-Gobain Abrasives Inc. d) DWS5 from Saint-Gobain Abrasives Inc.

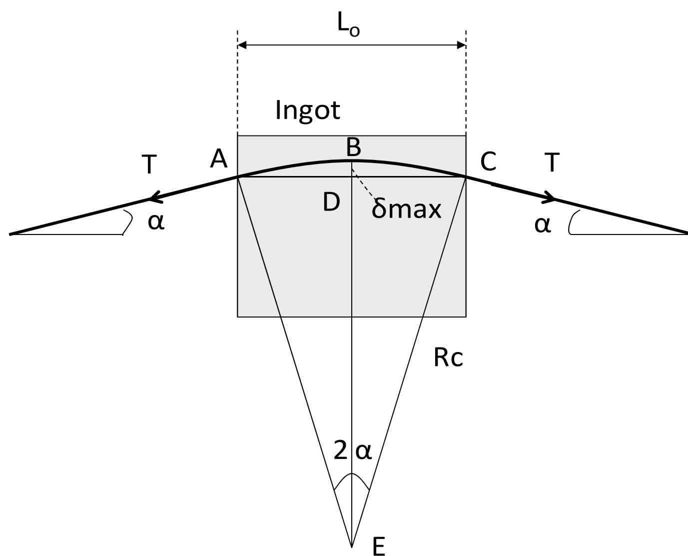


Fig. 3.3. Wire bow angle and wire curvature in wire saw tests.

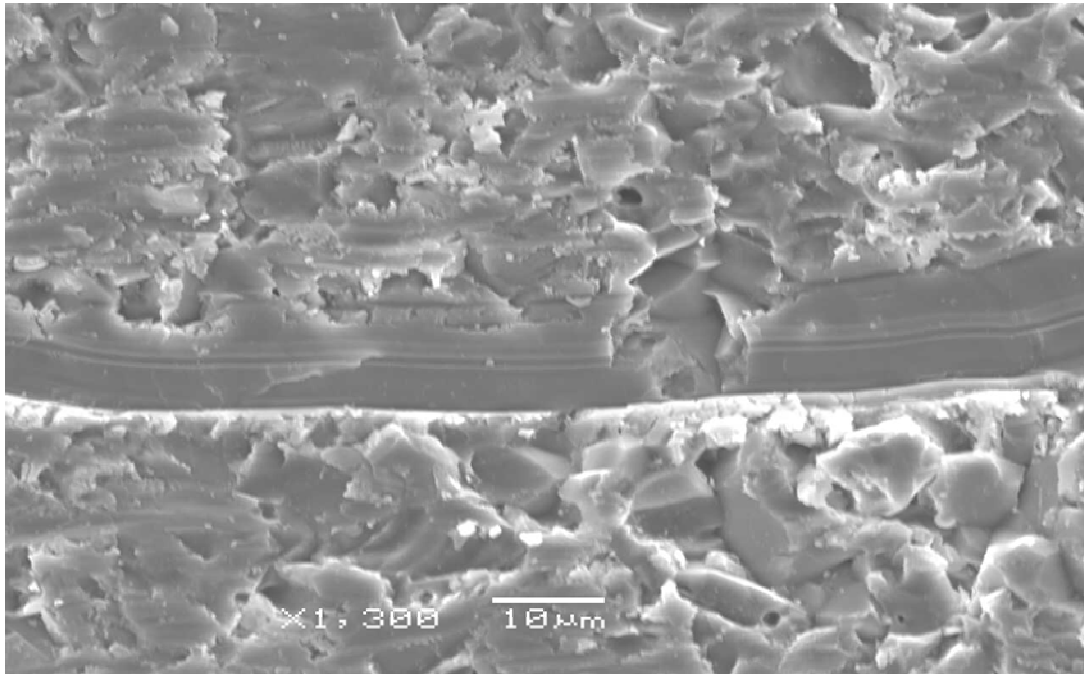


Fig. 3.4. The SEM image of a wire saw cut surface ($V_x$=1.3 m/sec, $V_z$= 5 μm/sec, $T$=13 N).

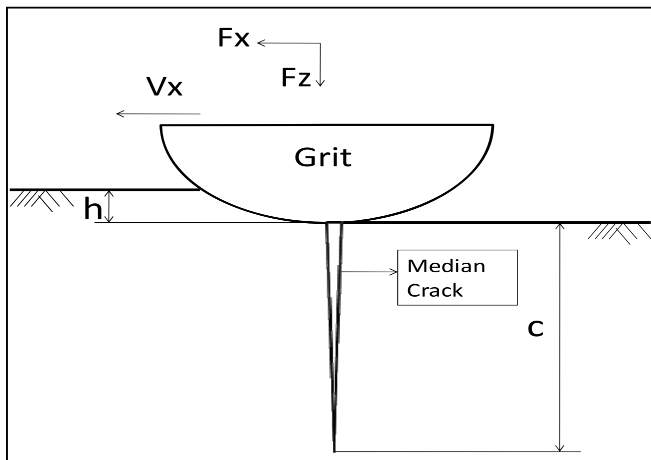


Fig. 3.5. Wire saw roughness damage model showing ductile material removal and brittle fracture.

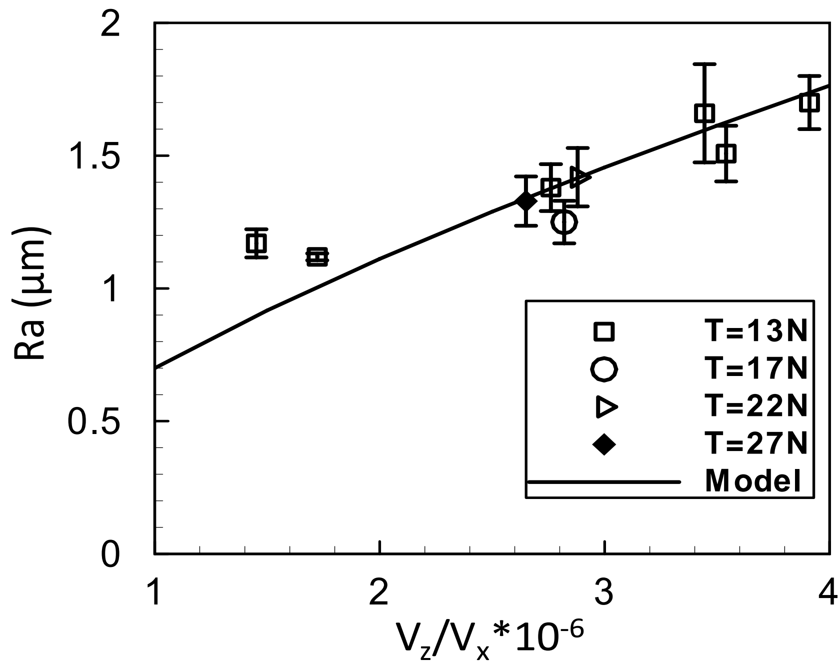


Fig. 3.6. Comparison of wire saw roughness damage model with respect to experimental results.

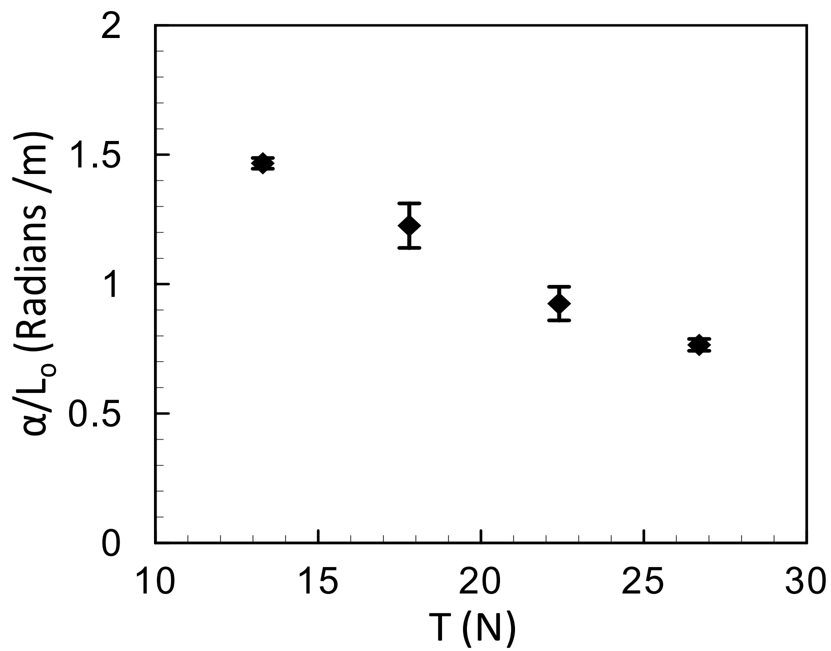


Fig. 3.7. The variation of wire bow angle per unit cut length $\alpha/L_o$ as a function of wire tension $T$ ($V_x$=1.8 m/sec, $V_z$= 5 µm/sec).

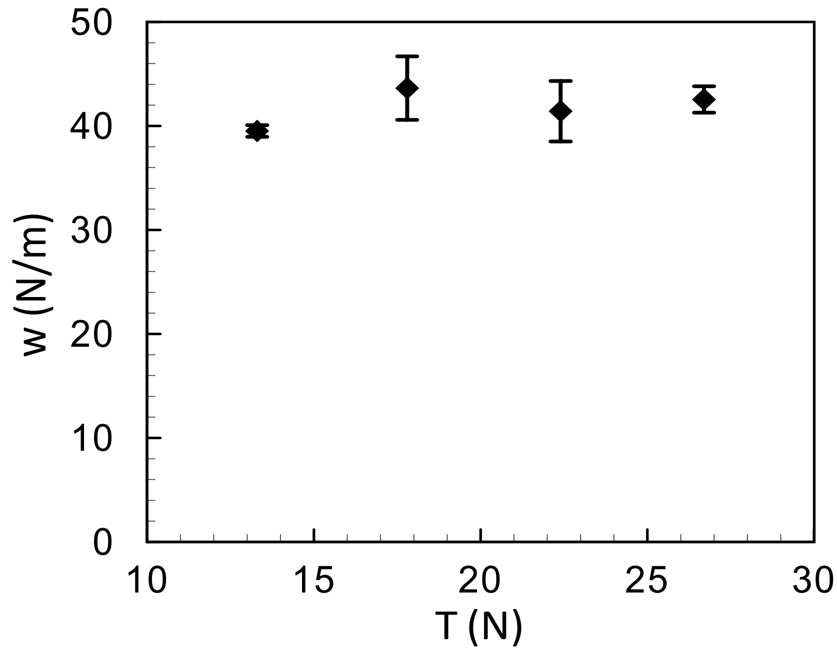


Fig. 3.8. The variation of distributed load $w$ as a function of wire tension $T$ ($V_x$=1.8 m/sec, $V_z$= 5 μm/sec).

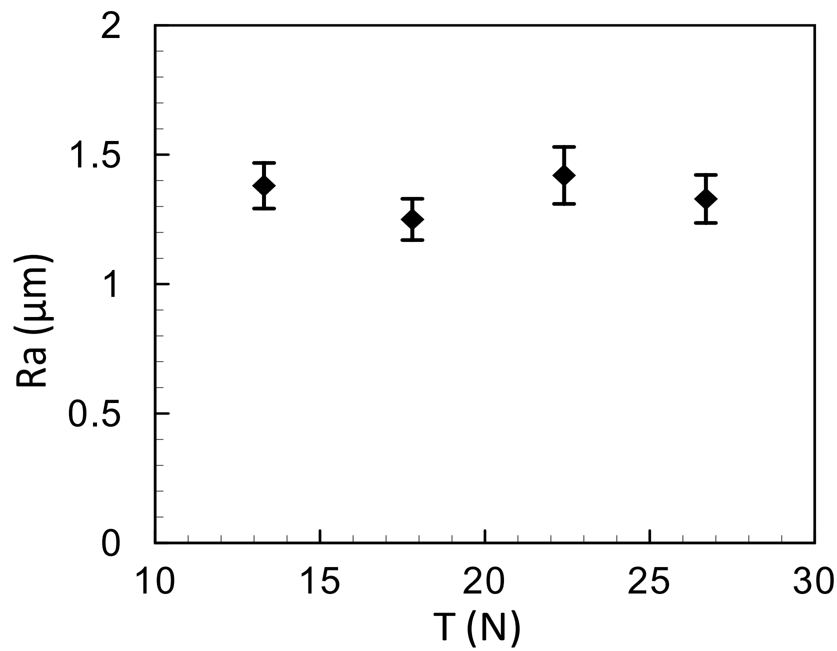


Fig. 3.9. The variation of surface roughness as a function of wire tension $T$ ($V_x$=1.8 m/sec, $V_z$= 5 μm/sec).

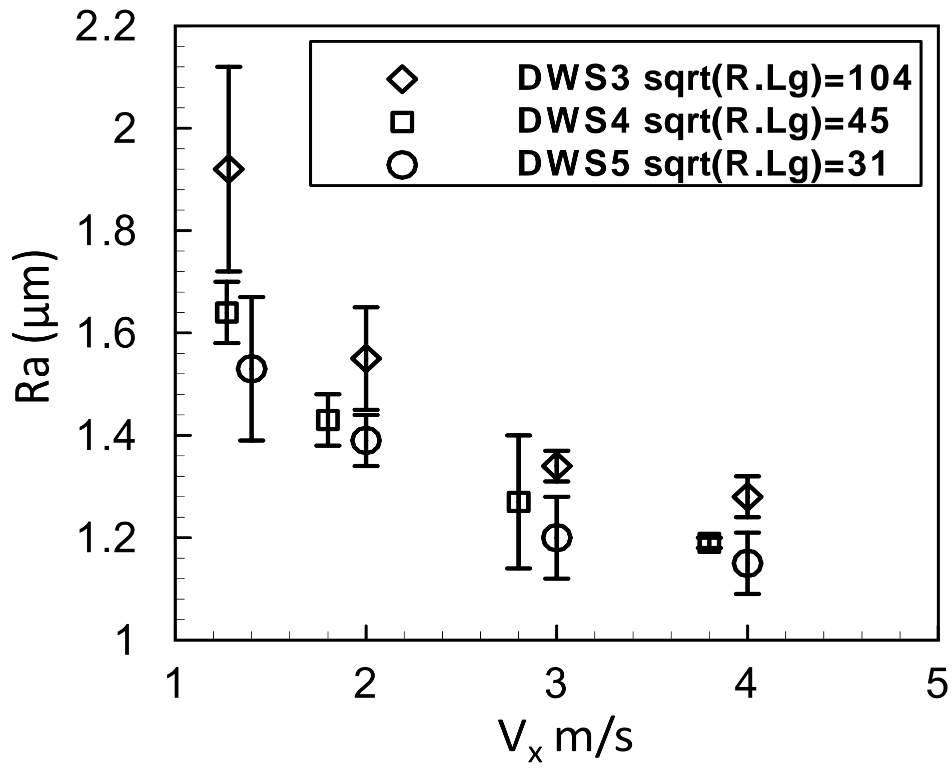


Fig. 3.10. The variation of surface roughness as a function of $V_x$ ($V_z$= 6.35 μm/sec, T=13N). The tests are done with different wires.

Table 3.1. Diamond wire properties.

| Wire Name | Diameter Dw (µm) | Grit Size Dg (µm) | Grit Radius R (µm) | Grit Spacing Lg (µm) | sqrt(R*Lg) (µm) | Note |
|---|---|---|---|---|---|---|
| DWS2 | 296 | 66 | 33 | 215 | 84 | Old wire |
| DWS3 | 304 | 78 | 39 | 280 | 104 | Well Inc. |
| DWS4 | 204 | 23 | 11.5 | 177 | 45 | Saint-Gobain Inc. |
| DWS5 | 252 | 27 | 13.5 | 69 | 31 | Saint-Gobain Inc. |

# CHAPTER 4. WIRE SAW PROCESS INDUCED LONG WAVINESS INVESTIGATION

A paper to be submitted to *The International Journal of Machine Tools & Manufacture*

**Egemen Teomete[1], Ashraf F. Bastawros[1,2], Abhijit Chandra[2,1]**
[1]Department of Aerospace Eng., [2]Department of Mechanical Eng., Iowa State University

## Abstract

Silicon wafers in photo voltaic and semi conductor industries are sliced using a wire saw process. The wire saw process is also used to machine almost all kinds of brittle materials where a high yield and low surface damage is desired. The wire saw process induces long waviness on the cut surfaces. The long waviness has to be removed by post process techniques including grinding and lapping, which increases costs. In this study, the long waviness induced by the wire saw process is investigated. An analytical model for long waviness generation is developed. Experimental work is conducted with different process parameters. The analytical model is capable of explaining the long waviness generation observed in experimental work. Process design recommendations with minimal waviness and high efficiency are presented.

## 4.1. Introduction

The wire saw process is widely used in slicing silicon wafers in the photovoltaic and microelectronics industries. The advantages of the wire saw with respect to inner diameter saw are high productivity, less wafer surface damage, and lower kerf loss [1]. The wire saw process can also be used to cut all kinds of brittle materials including sapphire, silicon carbide, lithium niobate, rocks, high density ceramics, and foam ceramics [1,2,3].

In the 1990s, the wire saw process was consisting of a bare steel wire and abrasive carrying slurry, resulting in free-abrasive machining using elasto-hydrodynamic forces [4,5]. In order to increase the efficiency and to cut harder materials, diamond impregnated wire, which leads to fixed-abrasive machining, was developed [4]. The diamond-impregnated wire saw process also eliminated the disposal of high amounts of hazardous slurry, which was an output of the abrasive-carrying slurry wire saw process [6].

The wire saw process makes up 30% of the total silicon wafer production cost, which affects the industry directly. The high cost of the process requires development of models relating process parameters with outputs [7].

There have been three main topics in wire saw literature: material removal mechanisms, kinematics of wire, and parametric studies between the process inputs and outputs.

The materials removal rate of the abrasive-carrying slurry wire saw process, which leads to free-abrasive machining, has been studied by different researchers [5,7]. Materials removal mechanisms for bead-impregnated wire saw cutting of rock is a Hertzian type fracture that occurs due to tensile field due to sliding bead [8].

Wire vibration characteristics have been studied with respect to process parameters [1,9,10]. The influence of process parameters on slurry film pressure and thickness has been studied for the free-abrasive wire saw process [1,5].

Experimental parametric studies relating surface damage with process parameters for cutting various materials have also been conducted [2,6,11]. Rigorous efforts have been devoted to removing wire saw induced waviness by post processing [12-17].

In this study, the long waviness generation due to the wire saw process is investigated. An experimental study is conducted to explore the effects of process parameters. An analytical model for waviness generation is developed. The experimental process is presented in section 4.2, the model is presented in section 4.3, and results and discussion are presented in section 4.4. The conclusion is presented in section 4.5.

## 4.2. Experimental Design

Wire saw experiments are conducted on alumina ceramic. The wire bow angle, wire axial speed, $V_x$, and feed rate, $V_z$, are measured during the wire saw cutting tests. The surface waviness of cut surfaces is also measured. The equipment used in these measurements and the process parameters are presented in this section.

### 4.2.1 The Wire Saw Process and Wire Bow Angle Measurement

A wire saw machine[1] is used in the experiments. This spool-to-spool wire saw machine with rocking motion of the wire can be controlled by the wire speed, $V_x$, down-feed speed, $V_z$, and wire tension, $T$. The tension is controlled by wire tension pulleys powered by air pressure, while the rocking motion is controlled by wire guide pulleys as can be seen in Fig. 4.1. The cut length of wire, which is used during the cutting, is 310 ft (94.5 m). Thus, at every direction reversal, 310 ft of wire is transferred from one spool to the other.

The wire speed is a function of spool diameter as the machine controls the speed via the angular frequency of the spool. In order to get the actual average speeds, a Strobex Systems 236 model stroboscope[2] is used. The down-feed speed, $V_z$, is measured by tracking the position of a grid, which is on the yoke of the machine, with respect to a stationary point on the frame of the machine. As the yoke goes down, the grid moves relative to the fixed point on the frame of machine. The time to travel 5 mm grids is measured during the tests.

Diamond-grit-coated steel wire, a product of Well Diamond Wire Saws Inc., is used in the experiments. The wire is manufactured by mechanically impregnating the diamond grits into the steel wire. The impregnation process might be successful for some grits, while others just leave an indentation mark on the wire and could not be affixed as seen in Fig. 4.2.

[1] Millennium model wire saw machine produced by Diamond Wire Technology in Colorado, Springs.

[2] Product of Chadwick-Helmuth Inc., California.

[3] Product of Synthetic Lubricants, Inc.

Alumina ceramic samples having a tensile strength of $\sigma_{fr}$=300 MPa, Poisson's ratio of $v$=0.22, fracture toughness $K_{IC}$ =4 MPam$^{1/2}$, Young's modulus of $E$=370 GPa [18], and hardness of $H$=22 GPa [19] are used in the cutting tests. The cut length of the samples is $L_o$ =25 mm and the height is between $H_s$ =60-90 mm. Three tests are done with the process parameters presented in Table 4.1.

A Kodak Easy Share DX 7630 6.1 megapixel digital camera is used to measure the wire bow angle as seen in Fig. 4.3. The images of the wire and sample are collected during the test and analyzed using the Matlab image-processing toolbox to obtain the angle, $\alpha$, between the wire and the horizontal. The average of the steady state wire bow angles, $\alpha$, is attained to the test as the steady-state wire bow angle of that test.

The Kodak digital camera is used also in getting the profile of the wire marks on the cut surface as seen in Fig. 4.4. The cut surface images are processed using the image-processing toolbox Matlab to obtain the wire-mark profile for each test.

### 4.2.2. Surface Waviness Measurements

The surface waviness of the cut surfaces are measured using an optical non-contact profilometer, Zygo New View 6000, manufactured by Zygo Corporation. A 2.5x lens with 2x zoom is used for the measurements. The profilometer has a vertical resolution on the order of 3 nanometer; the resolution in the horizontal plane is 8.83 µm, while the field of view used is 1.41×1.06 mm.

In a stitch measurement, the profilometer takes continuous measurements of 1.41×1.06 mm and stitches them together into one data set. Stitch measurements are applied in the direction of cutting at the center of the cut surface for each sample. After the measurements are taken, the data is processed using the software Metro Pro Version 8.1.5 developed by Zygo Co. The best fit plane is removed and a low pass filter is applied to get the waviness profile of the cut surface.

## 4.3. Wire Saw Process Induced Waviness Model

The wire bows in the plane of the cut (X-Z plane) and in the orthogonal (X-Y) plane. The definitions of the planes are presented in Fig. 4.5. The string deflection model is used to

explain the wire bow in the X-Z plane while energy competition between the oblique cutting, free standing, and wire tension is also used to explain the wire deflection in the X-Y plane.

### 4.3.1. The String Deflection Model

The deformation of a wire that is tensioned in both ends and subject to a distributed load per unit length, *w*, in the middle is presented in Fig. 4.6. An infinitesimal region of the loaded string is presented in Fig. 4.7. The horizontal and vertical equilibrium equations for force is obtained using Fig. 4.7 and presented in Eq. 4.1 and Eq. 4.2, respectively.

$$T_1 \cos\theta_1 = T_2 \cos\theta_2 = T \qquad (4.1)$$

$$T_2 \sin\theta_2 + w(x)\Delta x = T_1 \sin\theta_1 \qquad (4.2)$$

Solving Eq. 4.1 for $T_1$ and $T_2$ and inserting into Eq. 4.2 yields Eq. 4.3.

$$T(\tan\theta_2 - \tan\theta_1) = -w(x).\Delta x \qquad (4.3)$$

The string deflection is $\delta(x)$ as seen in Fig. 4.6. The slope of the string at any point can be written as in Eq. 4.4.

$$\tan\theta = \frac{d\delta(x)}{dx} \qquad (4.4)$$

Eq. 4.3 can be updated using Eq. 4.4.

$$T\left[\frac{\frac{d\delta(x)}{dx}\Big|_2 - \frac{d\delta(x)}{dx}\Big|_1}{\Delta x}\right] = -w(x) \qquad (4.5)$$

In the limit of $\Delta x$ approaches to zero, Eq. 4.5 can be written as in Eq. 4.6.

$$T\frac{d^2\delta(x)}{dx^2} = -w(x) \tag{4.6}$$

The distributed load per unit length on the wire is presented in Eq. 4.7.

$$w(x) = \begin{bmatrix} 0, & 0 \le x < \frac{L-L_o}{2} \\ w, & \frac{L-L_o}{2} \le x \le \frac{L+L_o}{2} \\ 0, & \frac{L+L_o}{2} < x \le L \end{bmatrix} \tag{4.7}$$

Using the boundary conditions $\delta(0)=0$, $\delta(L)=0$ and continuity of slope and deflection of wire, Eq. 4.6 can be solved. The wire deflection is presented in Eq. 4.8 [20]. The displacement at the mid span of the wire is presented in Eq. 4.9. The maximum wire bow deflection in the X-Z plane in the cut length seen in Fig. 4.6 is presented in Eq. 4.10. The $w$ is the distributed load, $L_o$ is the cut length of the sample where the distributed load is applied, $T$ is the wire tension, and $L$ is the span of the wire between guide pulleys, as seen in Fig. 4.6.

The wire deflection model presented in Eq. 4.8 will be compared to the experimentally obtained wire bow in the X-Z plane in the results and discussion section.

$$\delta(x) = \frac{wL_o}{T}\begin{cases} \frac{1}{2}x & 0 \le x < \frac{L-L_o}{2} \\ -\frac{x^2}{2L_o} + \frac{Lx}{2L_o} - \frac{1}{2L_o}(\frac{L-L_o}{2})^2 & \frac{L-L_o}{2} \le x \le \frac{L+L_o}{2} \\ \frac{1}{2}(L-x) & \frac{L+L_o}{2} < x \le L \end{cases} \tag{4.8}$$

$$\delta(\frac{L}{2}) = \frac{wL_o}{8T}(2L - L_o) \tag{4.9}$$

$$\delta_{\max} = \delta(\frac{L}{2}) - \delta(\frac{L - L_o}{2}) = \frac{wL_o^{\ 2}}{8T} \tag{4.10}$$

### 4.3.2. The Lateral Deflection Model in (X-Y) Plane

The string model presented in Eqs. 4.8-4.9-4.10 is upper bound for the wire deflection in the X-Y plane. The wire deflection in the X-Y plane is controlled by the energy competition between the oblique cutting forces, wire tension, and free-standing wire loaded with a distributed load. The wire saw cutting occurs due to each individual grits' cutting action in the cut length. Energetically, the cutting action of each grit is oblique cutting, which leads to divergence of the wire in the X-Y plane and forms the long waviness. The total oblique load, $w_y$, acting on the wire is related to the normal load, $w_z$, with a proportionality factor, $\beta$, as in Eq. 4.11.

$$w_y = \beta \times w_z \tag{4.11}$$

Experimental observations showed that the deflection in the X-Y plane, $\delta_y$, increases up to a limit as the cut depth, $z$, increases. As the deflection in the X-Y plane occurs due to oblique cutting action, the proportionality between the deflection in the X-Y plane, $\delta_y$, and the cut depth, $z$, has the same constant of proportionality between the lateral oblique force, $w_y$, and normal force, $w_z$, as in Eq. 4.12.

$$\delta_y(L/2, z) = \beta \times z \tag{4.12}$$

The value of the proportionality factor, $\beta$, will be determined from the surface profiles of each test using Eq. 4.12.

#### 4.3.2.1. The Energy Terms for Surface Waviness Generation

The long waviness occurs due to wire drifting in the X-Y plane. The oblique cutting forces drifts the wire out of the cutting plane (X-Z), while the wire tension is applying a recovery work on the wire to bring the wire into the cutting plane (X-Z). The limiting energy for the maximum deflection can be found using the work done by the free-standing wire under oblique load, $w_y$. Three energetic terms governing the behavior of the wire are introduced in this section.

##### 4.3.2.1.1. Work Done by Free Standing Wire ($WD_{fsw}$)

The upper bound of the work done by the free standing wire is calculated at maximum lateral deflection of wire in the X-Y plane, as in Eq. 4.13. The maximum deflection of the wire at mid span in Eq. 4.9 is used to calculate the final result in Eq. 4.13.

$$WD_{fsw} = \int_{\frac{L-L_o}{2}}^{\frac{L+L_o}{2}} w_y \delta_y^*(x)dx = \frac{w_y^2 L_o^2}{8T}(2L - L_o) \qquad (4.13)$$

##### 4.3.2.1.2. Work Done by Oblique Cutting Forces ($WD_{obl}$)

The work done by the oblique cutting force drifts the wire in the X-Y plane. The work done by the oblique cutting force is calculated using lateral distributed load, $w_y$, minus the lateral reaction, $R(z)$, applied by the wall of the sample to the wire. The lateral reaction on the wire, $R(z)$, changes with depth of cut as seen in Fig. 4.8. The lateral reaction has its maximum value at the beginning of the cut and diminishes to zero at maximum lateral deflection, $\delta_y$,* obtained at the cut depth, $z_1$. The lateral reaction is presented in Eq. 4.14. The work done due to oblique cutting is presented in Eq. 4.15. Using the Eq. 4.12 and Eq. 4.15, Eq. 4.16 is obtained for work done by oblique cutting.

$$R(z) = w_y(1 - z/z_1) \qquad (4.14)$$

$$WD_{obl}(z) = \int_0^{L_o} \left[ w_y - R(z) \right] \delta_y(x,z) dx = \left[ w_y - R(z) \right] L_o \delta_y(L/2, z) \qquad (4.15)$$

$$WD_{obl}(z) = \beta L_o w_y z^2 / z_1 \qquad (4.16)$$

#### 4.3.2.1.3. Work Done by Wire Tension ($WD_T$)

The work done by the wire tension, $T$, to deflect wire back to the undeformed position in the X-Y plane is presented in Eq. 4.17.

$$WD_T = \int_0^{\theta_f} 2T \sin\theta \frac{L}{2} d\theta = TL \int_0^{\theta_f} \sin\theta d\theta = TL(1 - \cos\theta_f) \qquad (4.17)$$

The angle, $\theta_f$, is between the wire and the horizontal line in the X-Y plane as seen in Fig. 4.6. The angle, $\theta_f$, is a function of wire length and mid-span deflection as presented in Eq. 4.18. The work done by wire tension can be written using Eq. 4.12, Eq. 4.17, and Eq. 4.18, as in Eq. 4.19.

$$\cos\theta_f = \sqrt{\frac{L^2}{L^2 + 4\delta_y^{\ 2}(L/2, z)}} \qquad (4.18)$$

$$WD_T = TL \left[ 1 - \frac{L}{\sqrt{L^2 + 4\beta^2 z^2}} \right] \qquad (4.19)$$

#### 4.3.2.2. The Mechanisms Effecting Long Waviness

The mechanisms effecting the long waviness formation via the energetic terms presented in the previous section are presented in this section.

#### 4.3.2.2.1. Mechanism 1

Mechanism 1 occurs when the oblique cutting forces drifts the wire in the X-Y plane until the critical cut depth, $z_1$, is achieved. The work done by oblique, $WD_{obl}$, cutting increases with depth of cut until critical cut depth, $z_1$, at which the $WD_{obl}$ is equal to the work done by the free standing wire, $WD_{fsw}$ as presented in Eq. 4.20 and Fig. 4.9. At cut depths greater than $z_1$, the wire will continue with the same lateral deflection until a process disturbance will change the oblique cutting conditions and drifts the wire back into cutting plane X-Z, as seen in Fig. 4.10. The rate of work done by oblique cutting is greater than the rate of work done by wire tension as presented in Eq. 4.21. The Mechanism 1 occurs when the wire tension is low which leads to a flexible wire. Mechanism 1 leads to tapered edges and high frequency roughness in the middle of the cut surface as seen in Fig. 4.10.

$$WD_{obl} = WD_{fsw} \tag{4.20}$$

$$\frac{\partial WD_{obl}}{\partial z} > \frac{\partial WD_T}{\partial z} \tag{4.21}$$

#### 4.3.2.2.2. Mechanism 2

Mechanism 2 occurs when the oblique cutting forces drifts the wire in the X-Y plane until reaching the cut depth, $z_3$, at which the work done by the oblique cutting is equal to work done by wire tension as seen in Eq. 4.22 and in Fig. 4.11. Work done by wire tension will reverse the oblique cutting direction, drifting the wire back into cutting plane X-Z and forming waviness as seen in Fig. 4.12. The repetition of this process will lead to waviness with a wavelength of $4.z_3$ as presented in Fig. 4.12. The rate of work done by oblique cutting is smaller than the rate of work done by wire tension as seen in Eq. 4.23. Mechanism 2 occurs when the wire tension is high, which leads to a stiff wire. The amplitude of the waviness obtained in mechanism 2 will be smaller than the amplitude of the wire drift in mechanism 1.

$$WD_{obl} = WD_T \tag{4.22}$$

$$\frac{\partial WD_{obl}}{\partial z} < \frac{\partial WD_T}{\partial z} \tag{4.23}$$

**4.4. Results and Discussion**

The upper bound for the wire deflection in the cutting plane X-Z and oblique plane X-Y is derived using the string model. A lateral deflection model, including oblique cutting of abrasive grits, energetic terms effecting wire deflection, and the mechanisms based on the energetic terms and governing the surface profile, is derived.

The profile of the wire marks obtained from the cut surfaces in X-Z plane are presented in Fig. 4.13. The discrete data points are measurements obtained from the cut surfaces of each test, while the continues curves are the string model predictions. The distributed load on the wire is obtained using Eq. 4.24. The wire bow angle, $\alpha$, is measured from the images captured during the test. The $T$ is the wire tension and $L_o$ is the cut length. The distributed load, wire tension, cut length, and span length are inserted in Eq. 4.8 to obtain the string model predictions for the wire bow, as presented in Fig. 4.13. The string model estimations for the wire profile in the X-Z plane are satisfactory.

$$w = \frac{2T\sin\alpha}{L_o} \tag{4.24}$$

The increase of tension two times decreases the wire bow amplitude almost by half, while increasing the feed speed increases the wire bow amplitude as seen in Fig. 4.13. These trends are captured by the string model very well, as seen in Fig. 4.13.

The surface profiles obtained from profilometer measurements for each test are presented in Fig. 4.14, Fig. 4.15, and Fig. 4.16, respectively. The proportionality factor, $\beta$ in Eq. 4.11 and Eq. 4.12 is determined from the slopes of the dashed lines representing the out-of-plane deflection of the wire due to oblique forces, as presented in Fig. 4.14, Fig. 4.15, and Fig. 4.16. The average of the slopes of these lines is attained as the factor $\beta$=0.0123. The energy plots of the tests are presented in Fig. 4.17, Fig. 4.18, and Fig. 4.19, respectively. All

of the energy plots show Mechanism 1 behavior, in which work done by oblique cutting is limited by the work done by the free standing wire, as in Fig. 4.9. Although all of the energy plots show Mechanism 1 behavior, the increase of wire tension or feed speed has a marked effect on the long waviness, which can still be explained by the waviness model. The increase of wire tension will lead to a stiff wire, which will lead to Mechanism 2, a wavy surface, while the increase of feed speed will increase the oblique cutting forces, which will lead to Mechanism 1. All the tests in this work have Mechanism 1 type energy plots as presented in Fig. 4.9. However, the increase of wire tension decreases the difference $z_2$-$z_1$ which will drive the system towards Mechanism 2 and, ultimately, when $z_2$-$z_1$ =0, Mechanism 2 will be obtained energetically, as in Fig. 4.11. There is not a strict boundary between the Mechanism 1 and Mechanism 2. While a system is energetically in Mechanism 1, because of high wire tension the $z_2$-$z_1$ difference will reduce, driving the system towards Mechanism 2 as in Fig. 4.20 for TC21 with respect to TC20. Increase of feed speed will increase the oblique cutting forces, driving the system towards Mechanism 1 and increasing the $z_2$-$z_1$ difference as seen in Fig. 4.20 for TC22 with respect to TC21.

The test TC20 is done with wire tension $T$=13.3 N, while TC21 is done with $T$=26.7 N; both tests have the same wire speed, $V_x$, and feed speed, $V_z$. The increase of wire tension decreases the difference $z_2$-$z_1$ for TC21 with respect to TC20, driving the TC21 towards Mechanism 2, as seen in Fig. 4.20. Test TC20, being closer to Mechanism 1, has a step-like surface, as in Fig. 4.14, which complies with the expectations for a step-like surface for Mechanism 1 as presented in Fig. 4.10. Test TC21, being closer to Mechanism 2 with respect to TC20, has a wavy surface as presented in Fig. 4.15. The peak-to-valley ($PV$) value, which is the height difference between the highest and lowest points on a surface profile, is also affected by the change in wire tension. Experiment TC20, having a lower wire tension of $T$=13.3 N, has a higher $PV$=199 µm, while experiment TC21, having a higher wire tension of $T$=26.7 N, has a lower $PV$=69 µm. The increase of wire tension, $T$, decreases the $PV$ value, which is expected as Mechanism 1 creates a high amplitude step, while Mechanism 2 creates lower amplitude waviness.

The test TC21 is done with a feed speed of $V_z$=6.4 µm/s, while the TC22 is done with a feed speed of $V_z$=12.7 µm/s; both have the same wire speed and tension. The increase of

feed speed increases the oblique cutting forces, driving the TC22 towards Mechanism 1. The increase of feed speed increases the difference $z_2$-$z_1$ for TC22 with respect to TC21, driving the TC22 towards Mechanism 1, as seen in Fig. 4.20. The peak-to-valley (*PV*) value is also affected by the change of feed speed. Experiment TC21, having a lower feed speed of $V_z$=6.4 µm/s, has a lower *PV*=69 µm, while experiment TC22, having a higher feed speed of $V_z$=12.7 µm/s, has a higher *PV*=86 µm. The increase of feed speed increases the *PV* value, which is expected as Mechanism 1 creates a high amplitude step, while Mechanism 2 creates lower amplitude waviness.

Fig. 4.20 shows that as the difference, $z_2$-$z_1$, increases, the peak-to-valley, *PV*, value increases for all three experiments and system evolves towards Mechanism 1, while decreasing difference, $z_2$-$z_1$, leads to Mechanism 2. High wire tension will reduce the peak-to valley-value, while high feed rate will increase the *PV* value. The increase of peak-to-valley value will lead to more post grinding and polishing of the cut surface and an increase in expenses. In order to increase the efficiency without increasing the *PV* value, the wire tension can be increased proportional to feed speed.

### 4.5. Conclusion

The wire-saw process induced long waviness on the cut surface is investigated in this study. Experimental work including different wire tensions and feed speeds is conducted. The string model is used to model the bow of the wire marks on the cut surface and satisfactory results are obtained. The increase of tension decreases the wire bow amplitude, while increases in feed speed increases the wire bow amplitude, which is predicted by the string model and observed in the experiments.

The long waviness formation is explained with energetic terms that define two mechanisms leading to different surface profiles. The defined mechanisms are used to explain the evolution of the surface profile and peak-to-valley value with respect to process parameters. The increase of wire tension will lead to a wavy surface with a lower peak-to valley-value, while decreasing wire tension will lead to a step-like surface with a high peak-to-valley value. The increase of feed speed will lead to a high peak-to-valley value. The increase of peak-to-valley value will lead to more post grinding and polishing of the cut

surface and increases in expenses. In order to increase the efficiency without increasing the peak-to-valley value, the wire tension can be increased proportional to feed speed.

### 4.6. Acknowledgement

This work is supported by US-National Science Foundation NSF through grant No. DMII-0355536.

### 4.7. References

[1] L. Zhu, I. Kao, Galerkin Based modal analysis on the vibration of wire-slurry system in wafer slicing using a wiresaw, Journal of Sound and Vibration 283 (2005) 589-620.

[2] W.I. Clark, A.J. Shih, C.W. Hardin, R.L. Lemaster, S.B. McSpadden, Fixed abrasive diamond wire machining – Part II: experiment design and results, International Journal of Machine Tools and Manufacture 43 (2003) 533-542.

[3] P.Q. Ge, L. Zhang, W. Gao, Z.C. Liu, Development of endless diamond wiresaw and sawing experiments, Materials Science Forum 471-472 (2004) 481-484.

[4] W.I. Clark, A.J. Shih, C.W. Hardin, R.L. Lemaster, S.B. McSpadden, Fixed abrasive diamond wire machining – Part I: process monitoring and wire tension force, International Journal of Machine Tools and Manufacture, 43 (2003) 523-532.

[5] M. Bhagavat,V. Prasad, I. Kao, Elasto-hydrodynamic interaction in the free abrasive wafer slicing using a wiresaw: modeling and finite element analysis, Transactions of ASME, Tribology Division, 122 (April 2000) 394-404.

[6] C.W. Hardin, J. Qu, A.J. Shih, Fixed abrasive diamond wire saw slicing of single-crystal silicon carbide wafers, Materials and Manufacturing Processes, 19 (2) (2004) 355-367.

[7] J.H. Moller, Basic mechanisms and models of multi–wire sawing, Advanced Engineering Materials 6 7 (2004) 501-513.

[8] B.C. Liu, Z.P. Zhang, Y.H. Sun, Sawing trajectory and mechanism of diamond wire saw, Key Engineering Materials, 259-260 (2004) 395-400.

[9] S. Wei, I. Kao, Analysis of stiffness control and vibration of wire in wiresaw manufacturing process, Proceeding of ASME, Manufacturing Science and Engineering Division, (1998) 813-818.

[10] S. Wei, I. Kao, Vibration analysis of wire and frequency response in the modern wire saw manufacturing process, Journal of Sound and Vibration, 231 (5) (2000) 1383-1395.

[11] J.F. Meng, J.F. Li, P.Q. Ge, R. Zhou, Research on endless wire saw cutting of $Al_2O_3$/TiC Ceramics, Key Engineering Materials 315-316 (July 2006) 571-574.

[12] W.J. Liu, Z.J. Pei, X.J. Xin, Finite element analysis for grinding and lapping of wire-sawn silicon wafers, Journal of Materials Processing Technology, 129 (2002), 2-9.

[13] Z.J. Pei, X.J. Xin, W. Liu, Finite element analysis for grinding of wire-sawn silicon wafers: a designed experiment, International Journal of Machine Tools & Manufacture 43 (2003) 7–16.

[14] Z.J. Pei, S. Kassir, M. Bhagavat , G. R. Fisher, An experimental investigation into soft-pad grinding of wire-sawn silicon wafers, International Journal of Machine Tools & Manufacture 44 (2004) 299–306.

[15] X. J. Xin, Z. J. Pei, W. Liu, Finite element analysis on soft-pad grinding of wire-sawn silicon wafers, Journal of Electronic Packaging, 126 (JUNE 2004) 177-185.

[16] X.Sun, Z.J. Pei, X.J. Xin, M. Fouts, Waviness removal in grinding of wire-sawn silicon wafers: 3D finite element analysis with designed experiments, International Journal of Machine Tools & Manufacture 44 (2004) 11–19.

[17] Yue Jiao, Z. J. Pei, Shuting Lei, E. Stanley Lee, Graham R. Fisher, A Fuzzy Adaptive Network Model for Waviness Removal in Grinding of Wire-Sawn Silicon Wafers, Journal of Manufacturing Science and Engineering, Transactions of the ASME, 128 (2006) 938-943.

[18] Material Property Data, http://www.matweb.com/index.aspx, (accessed March 2008).

[19] R.F. Cook, G.M. Pharr, Direct observation and analysis of indentation cracking in glasses and ceramics, Journal of American Ceramic Society, 73 (4) (1990) 787-817.

[20] A.F. Bastawros, A. Chandra, A. Shih, Analysis of surface waviness during wire saw cutting of ductile materials, Proceedings of 2006 NSF Design Service and Manufacturing Grantees and Research Conference, St. Louis, Missouri.

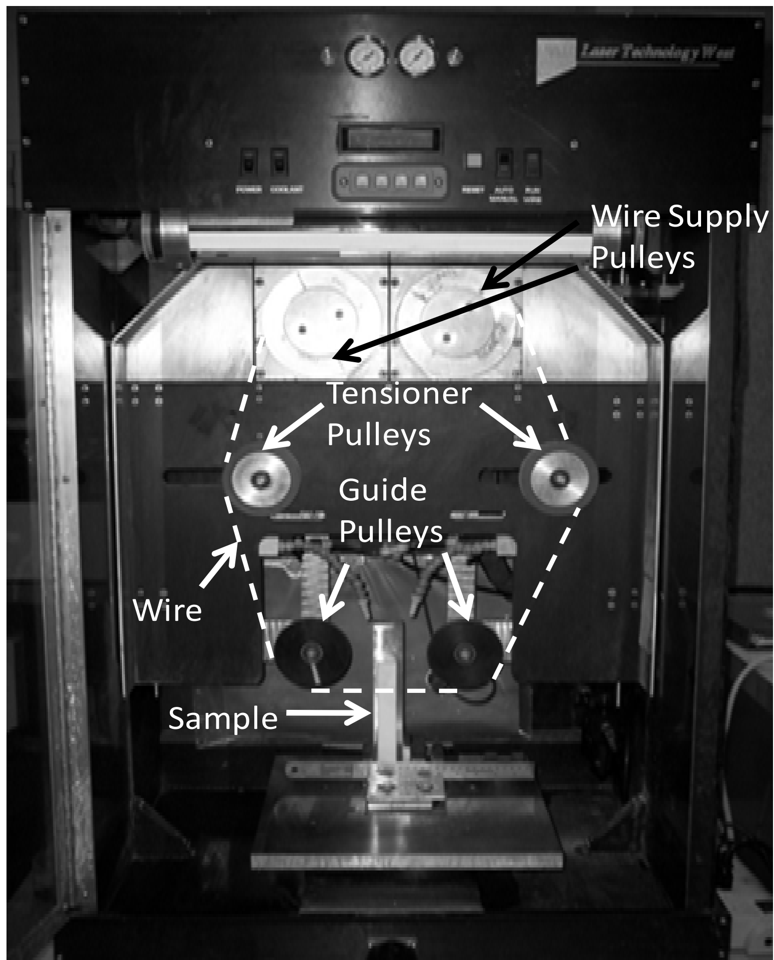


Fig. 4.1. Single wire, spool-to-spool wire saw machine (DWT Inc., Millennium Model) used in waviness tests. The wire track is marked by the dashed line.

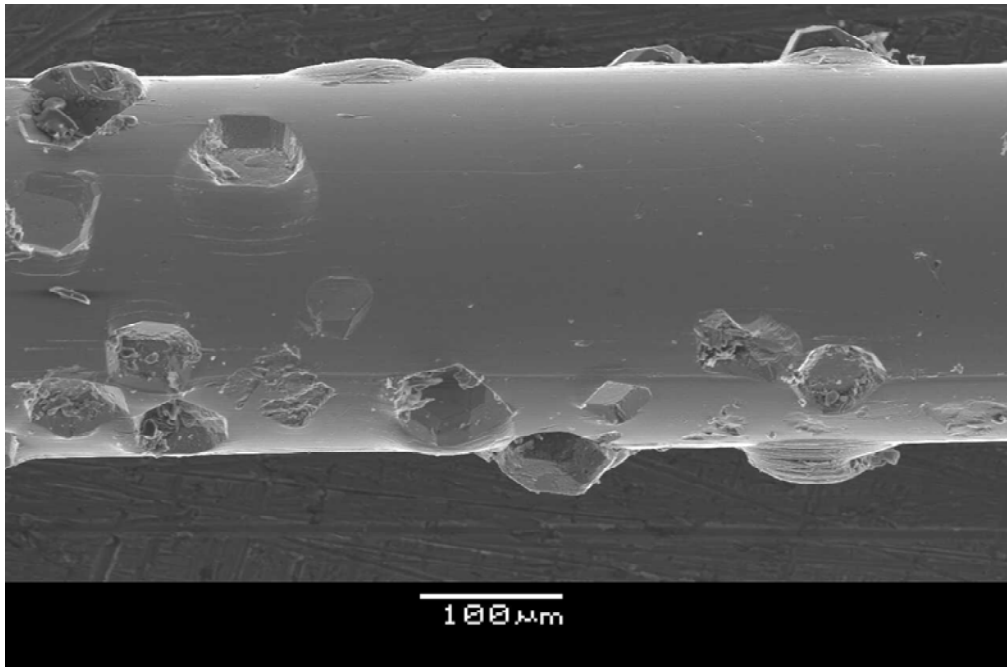


Fig. 4.2. SEM images of diamond impregnated wire.

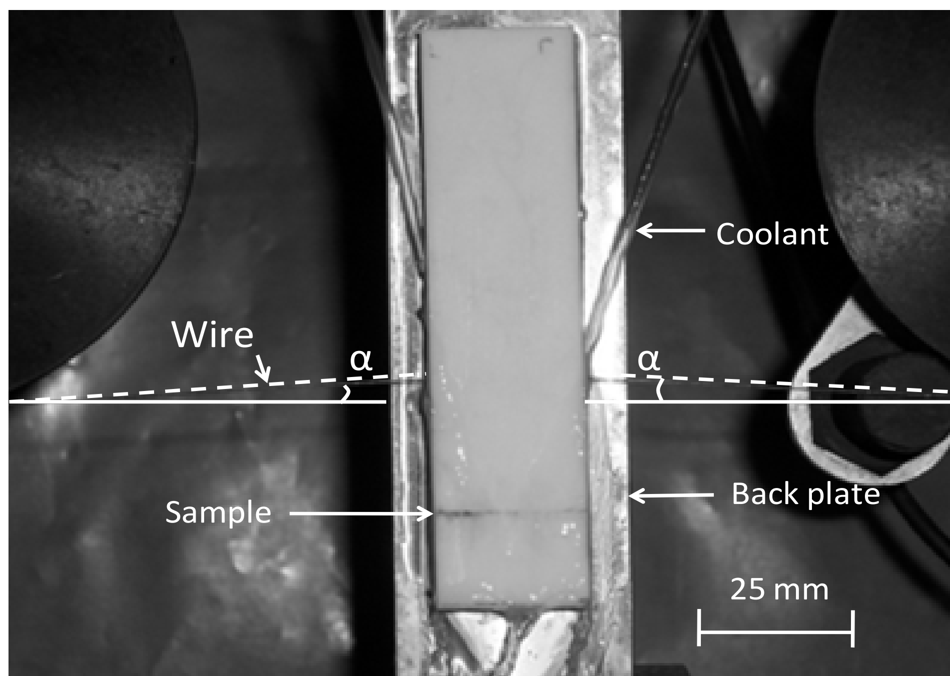


Fig. 4.3. Optical image showing the wire inclination angle with the cutting direction at the entrance and exit from the specimen for a waviness test.

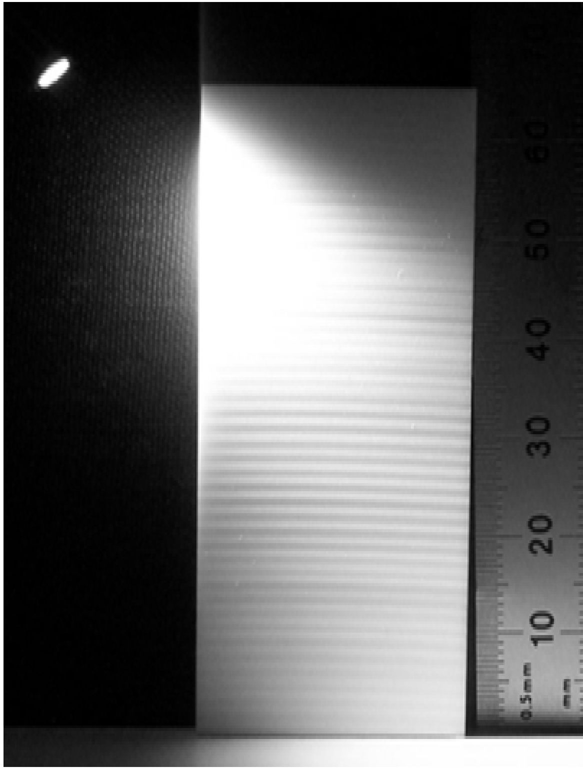


Fig. 4.4. Wire marks on a wire saw cut surface (TC22 Vx=2 m/s, Vz=12.7 μm/s, T=26.7 N).

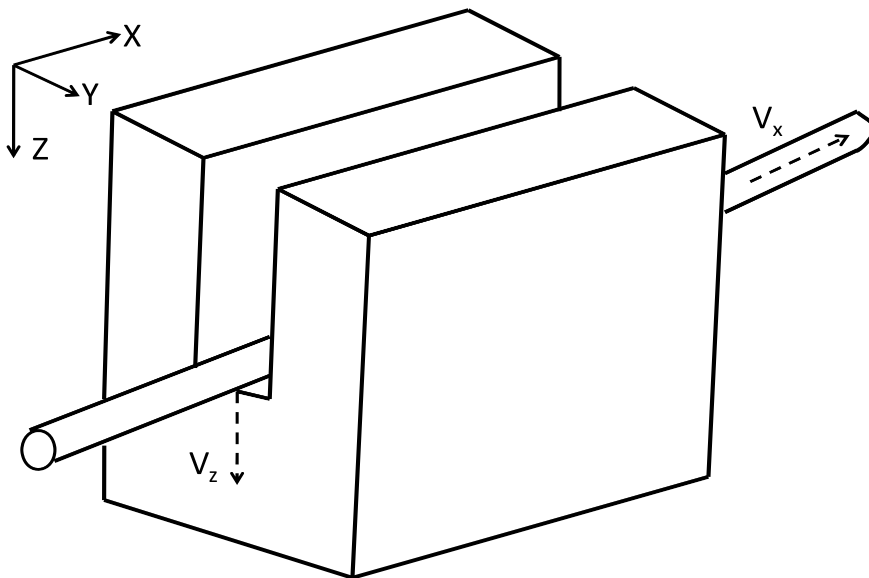


Fig. 4.5. The coordinate system defined for analyses of wire saw process.

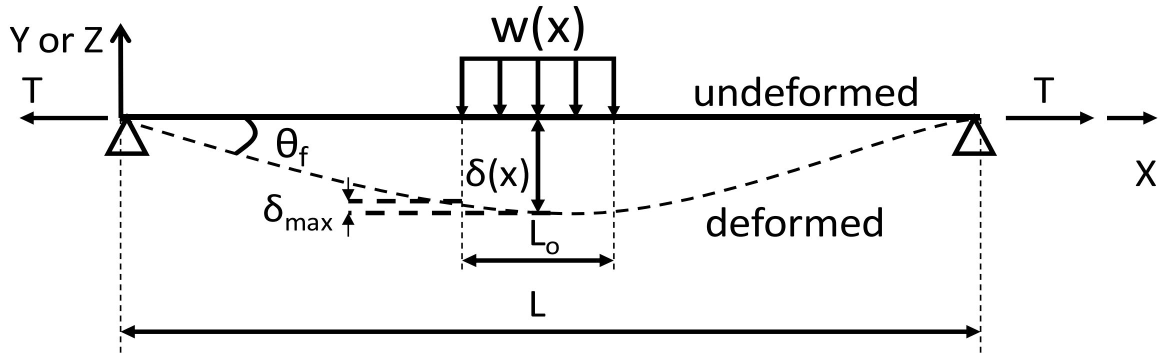


Fig. 4.6. The model of a wire under tension and distributed load.

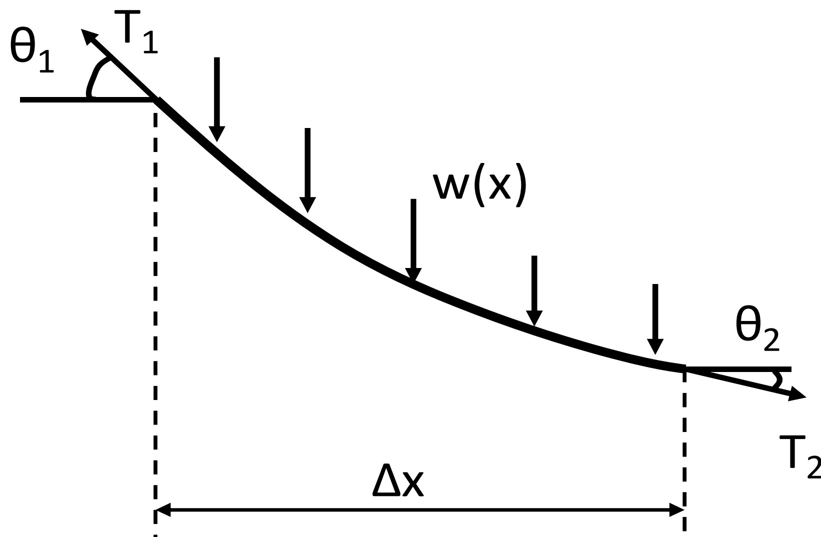


Fig. 4.7. The forces acting on an infinitesimal string element.

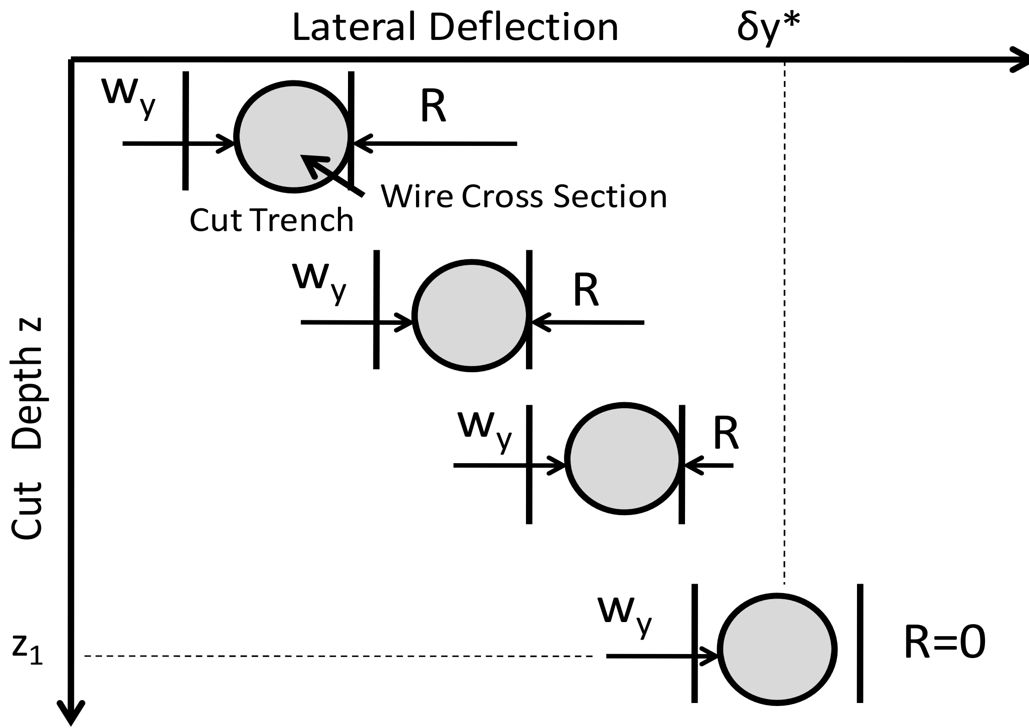


Fig. 4.8. Variation of lateral reaction with cut depth.

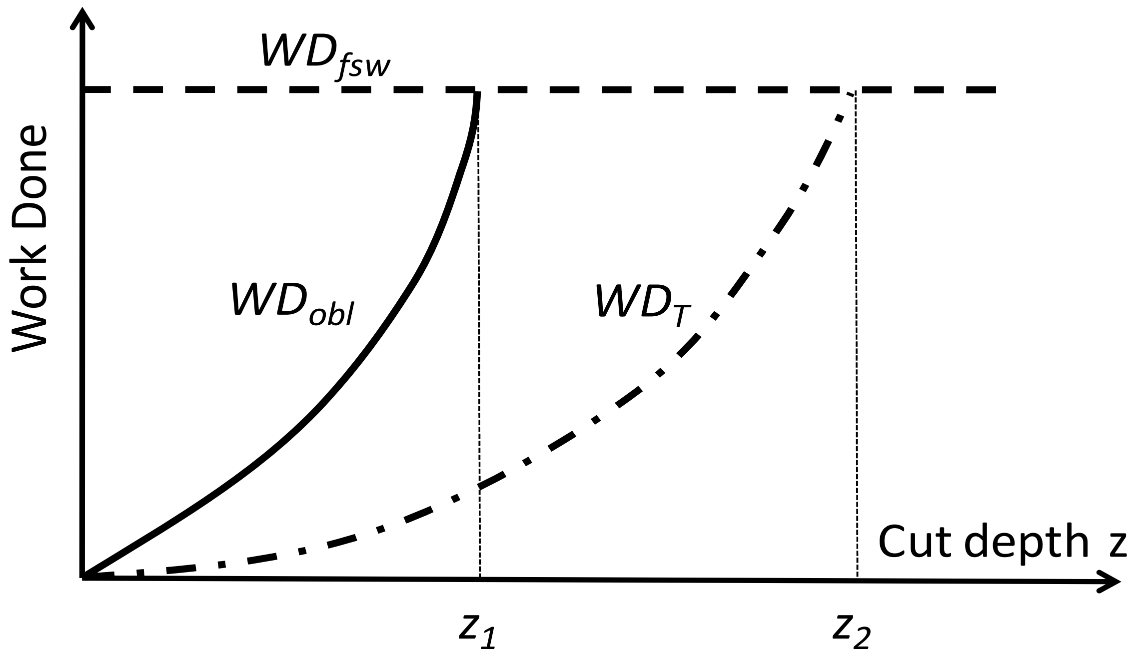


Fig. 4.9. Mechanism 1 energy plots.

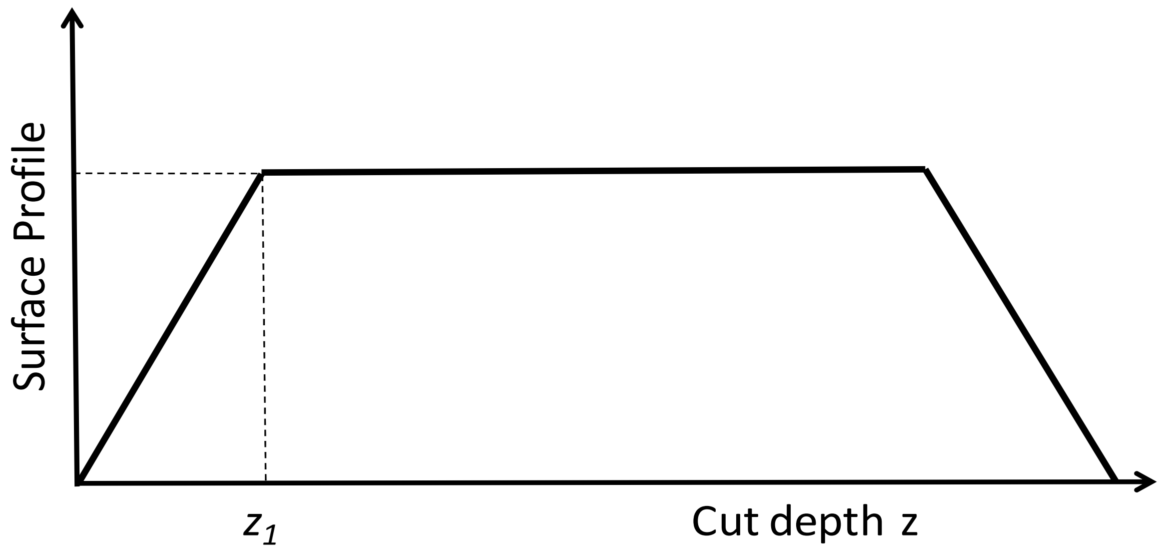


Fig. 4.10. Surface profile due to mechanism 1.

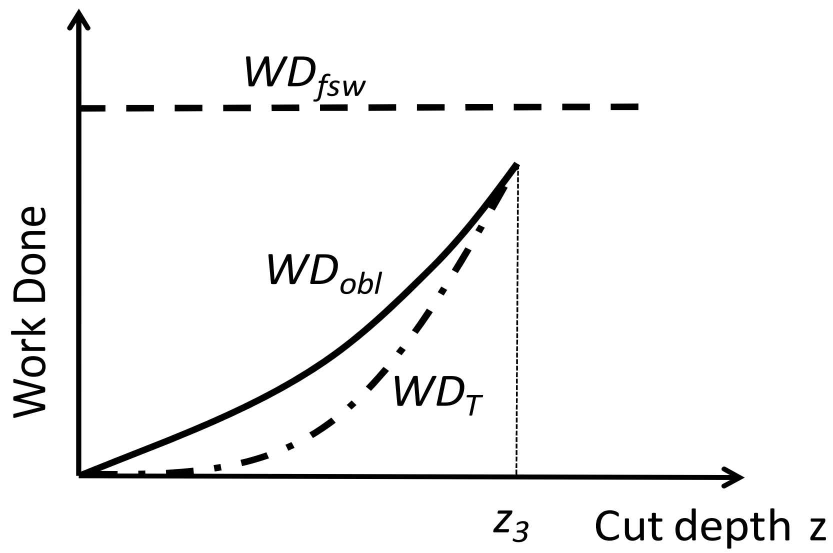


Fig. 4.11. Mechanism 2 energy plots.

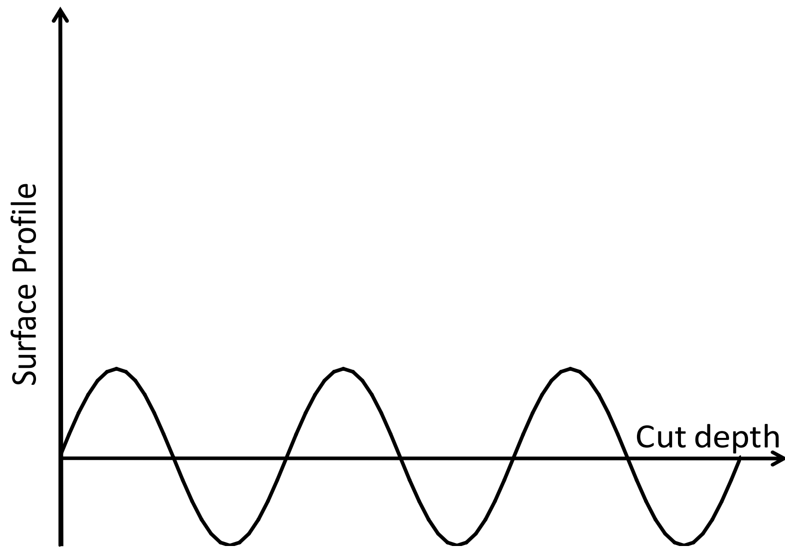


Fig. 4.12. Surface profile due to mechanism 2.

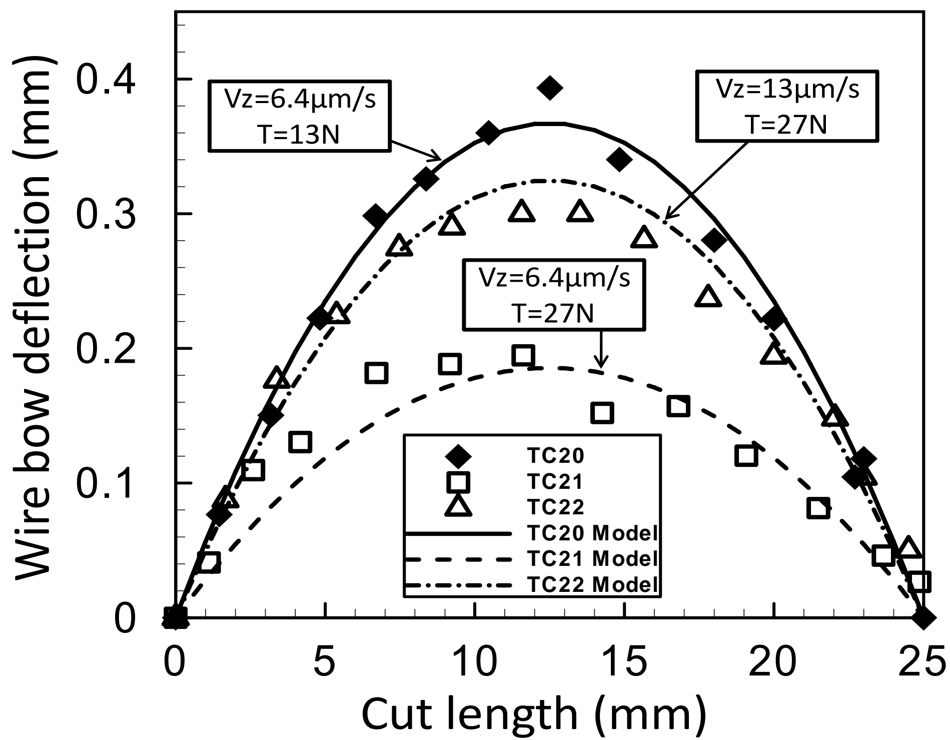


Fig. 4.13. Variation of wire bow as a function of wire tension and feed speed in cut plane X-Z.

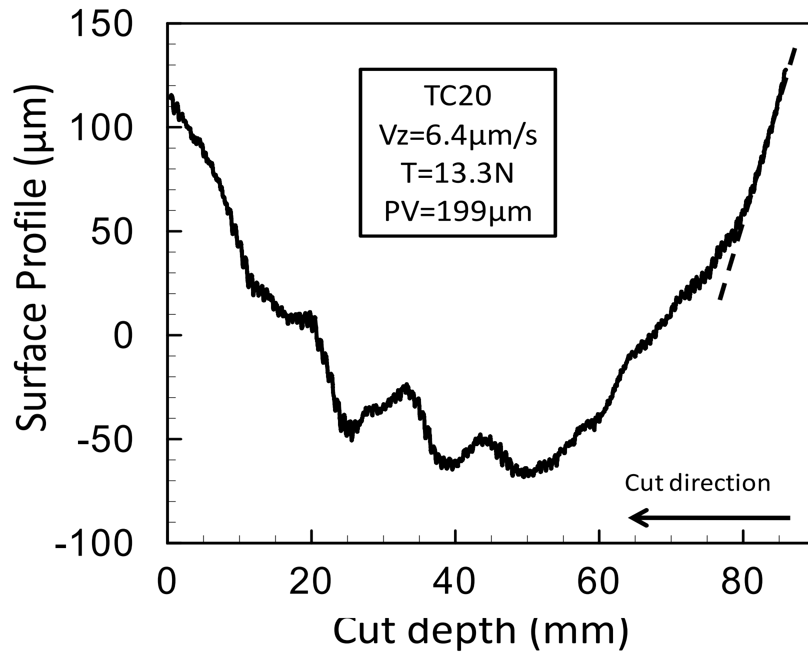


Fig. 4.14. Surface long waviness profile of TC20 test.

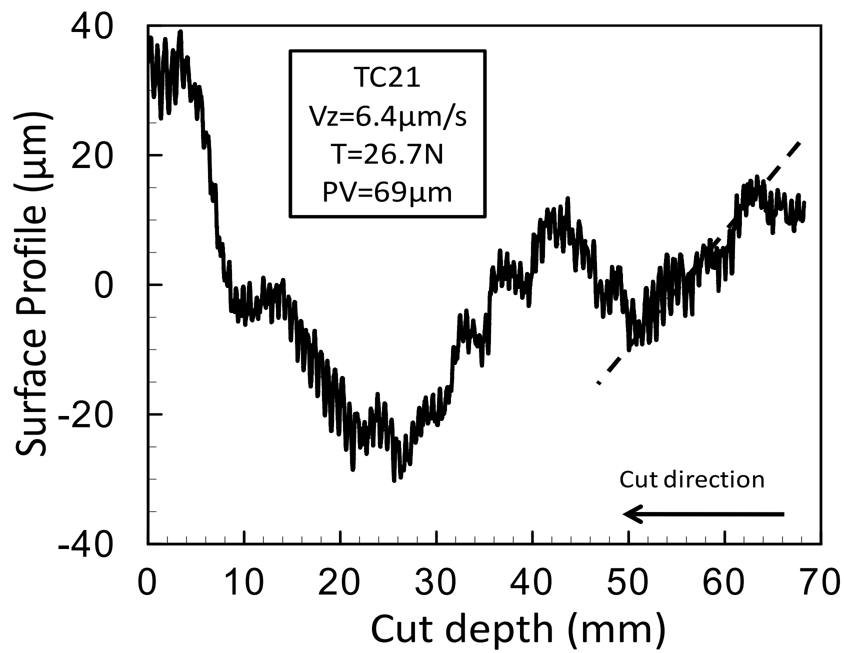


Fig. 4.15. Surface long waviness profile of TC21 test.

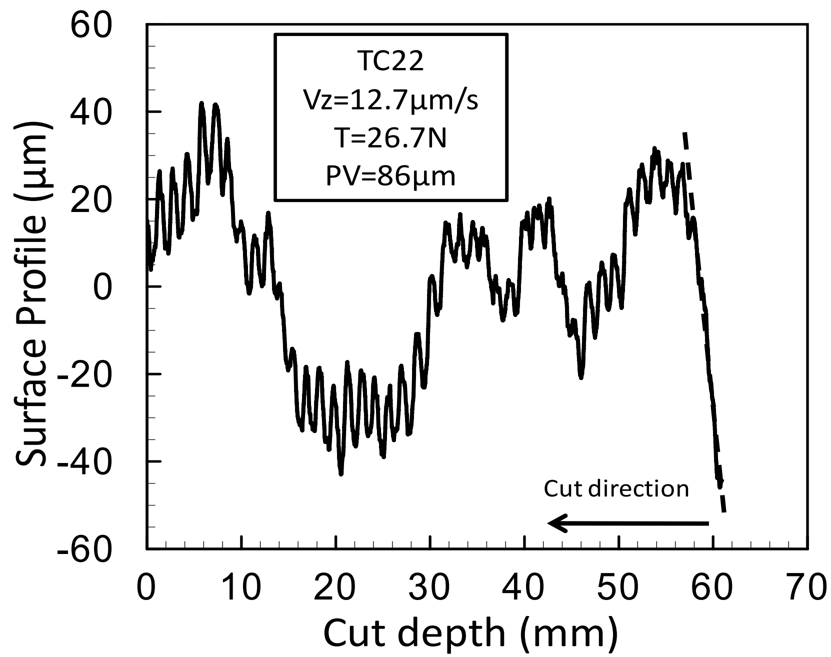


Fig. 4.16. Surface long waviness profile of TC22 test.

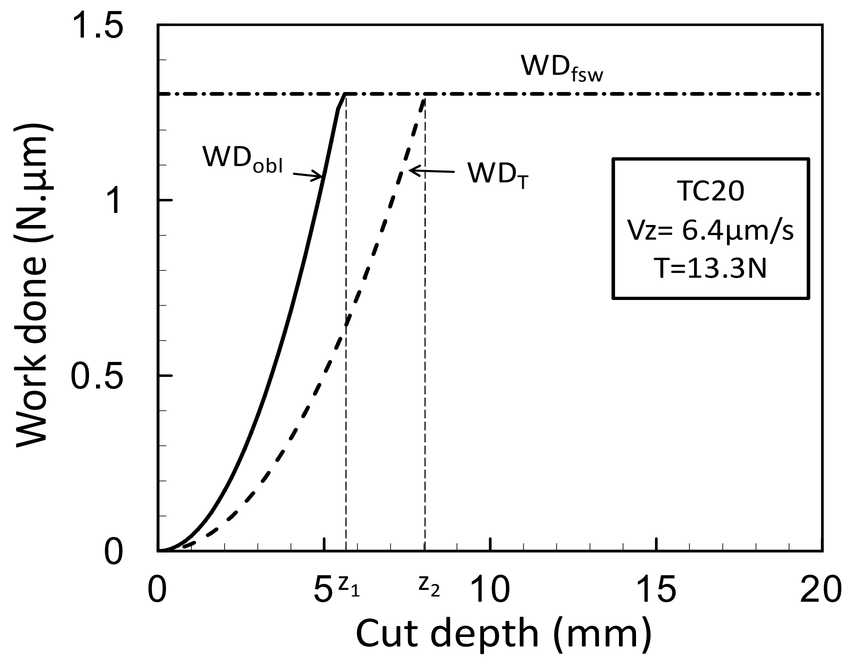


Fig. 4.17. Energy plots of TC20 test.

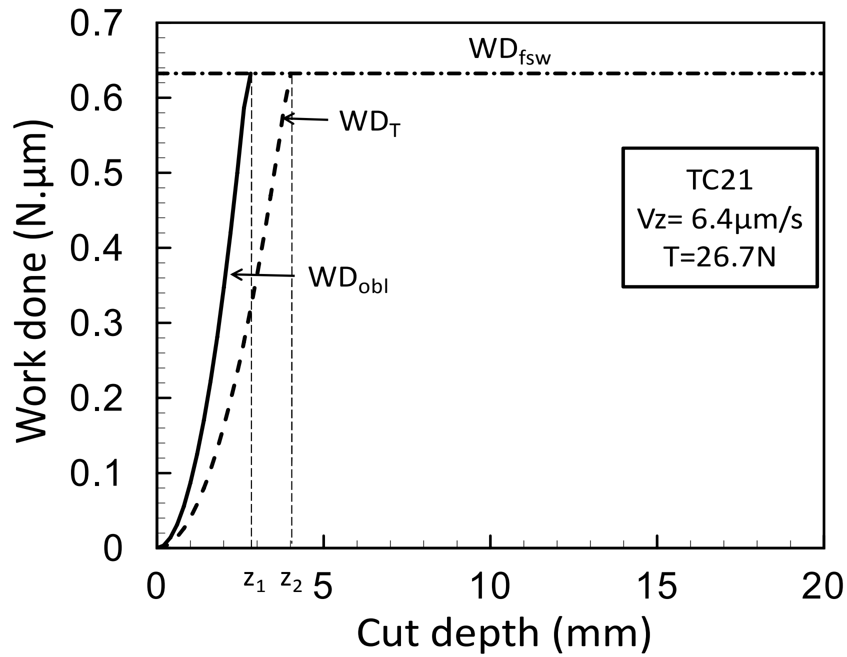


Fig. 4.18. Energy plots of TC21 test.

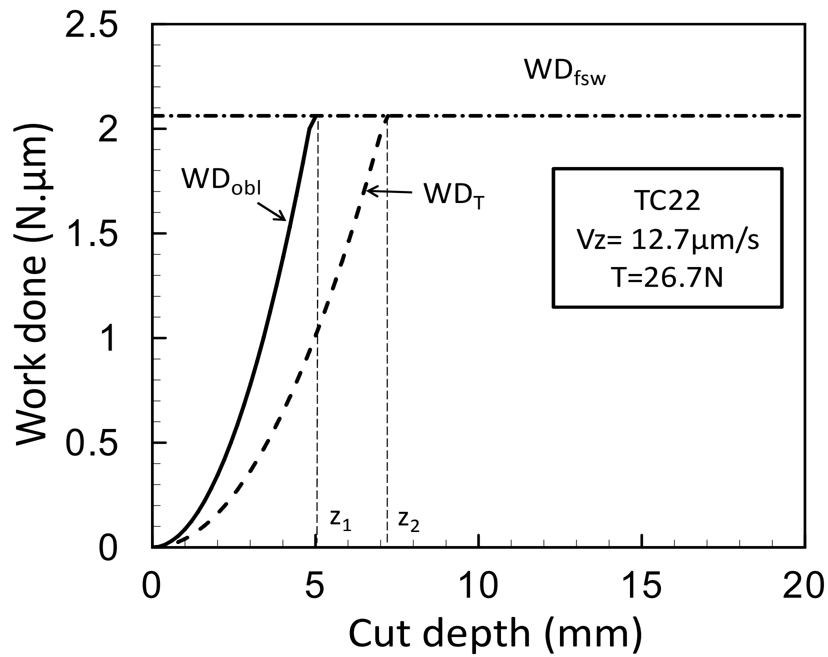


Fig. 4.19. Energy plots of TC22 test.

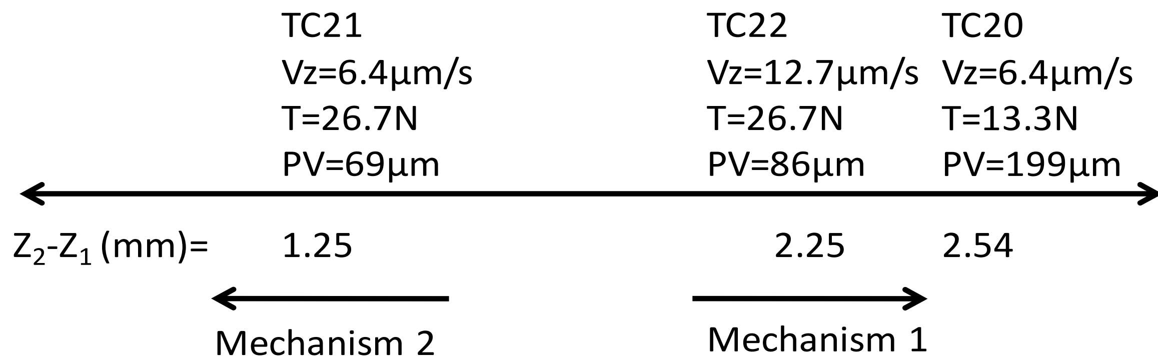


Fig. 4.20. Domains for long waviness mechanisms.

Table 4.1. The long waviness experiments parameters.

| | Vx (m/s) | Vz (μm/s) | T (N) | Lo (mm) | $w_z$ (N/m) | wy = β*$w_z$ (N/m) | WD1 (Nμm) | $z_1$ (mm) | $z_2$ (mm) | $z_2$-$z_1$ (mm) |
|---|---|---|---|---|---|---|---|---|---|---|
| TC20 | 2 | 6.35 | 13 | 25 | 62.5 | 0.77 | 1.30 | 5.51 | 8.05 | 2.54 |
| TC21 | 2 | 6.35 | 27 | 25 | 61.7 | 0.76 | 0.63 | 2.71 | 3.96 | 1.25 |
| TC22 | 2 | 12.7 | 27 | 25 | 111.4 | 1.37 | 2.06 | 4.89 | 7.14 | 2.25 |

# CHAPTER 5. WIRE SAW CUTTING INDUCED SURFACE DAMAGE AND DESIGN SPACE EXPLORATION

The wire saw process induced surface and subsurface damage is explored, utilizing a bonded sample configuration, as a function of the process parameters (wire speed, down-feed speed, and wire tension). The developed insight is used in combination with the long-waviness investigations, explored in Chapter 4, to explore the limits of the possible working range of the wire saw process.

## 5.1. Wire Saw Process Induced Surface Damage Depth Investigation

The damage induced by the wire saw process decreases the quality of the cut surface. The cutting process poses reliability concerns; it is the finishing process of the device (e.g actuators and sensors). Or, it may require additional post-processing steps that require additional capitals and result in additional scrap, which is the case for silicon wafers used in the semiconductor and photovoltaic industries. Post processes including grinding, lapping, polishing, and chemical etching to remove the wire saw induced damage and planarize the cut surface. There is a need to relate the process parameters to wire saw induced damage in order to improve the cutting process performance.

In the wire saw process, the material removal is primarily in the ductile mode. Surface damage arises from brittle cracking that extends beyond the plastic zone below the abrasive particle, as discussed in Chapter 3. The extent of surface damage and cracking sets the depth of material to be removed during post processing, in order to remove all the damage induced by the wire saw process.

Hardin et al. [1] used a Scanning Acoustic Microscope to measure the subsurface damage, but the interference of surface damage was a problem for truly identifying the extent of the subsurface damage. Xu and Jahanmir [2] used the bonded-interface sectioning (BIS) technique to examine the subsurface damage in scratching of alumina ceramics. The bonded-

interface sectioning technique is used to measure the surface damage depth in this study. The experimental work is presented in section 5.1.1, and the results are presented in section 5.1.2.

### 5.1.1. Experimental Setup

A single-wire, spool-to-spool wire saw machine[1] is used in the current investigation. A diamond-impregnated wire (DWS4) having a diameter of $D_w$=204 μm is used in the wire-saw cutting. The actual wire speed is measured by a stroboscope (Strobex 236)[2]. A Kodak digital camera (2856 × 2142 pixel) is used to obtain the wire bow images during the tests. A Scanning Electron Microscope (SEM) is used to obtain the surface damage depth. The details of these equipments are presented in Chapter 2.

Coolant having water to lubricant Sawzit[3] ratio of 50/1 is used during cutting tests. The cut length of wire used is 310 ft. Thus, at every direction reversal of wire, Lw=310 ft (94.5 m) of wire is transferred from one spool to the other.

Two rectangular alumina ceramic samples are used for the tests. The mechanical properties of alumina ceramic are introduced in Chapter 2. The two-section polished surfaces, having initial roughness of 1.5 μm, are bonded together by crystal bond. The laminated sample is glued to an aluminum holding post as shown in Fig. 5.1. The test matrix is presented in Table 5.1. Different wire speeds of 2, 3 and 4 m/sec are utilized. A combination of down-feed speed of 6.35, 9 and 12.7 μm/sec and wire tension of 13.3, 18 and 26.7 N are utilized at constant wire speed to explore the process domain.

After the wire saw cutting tests, the samples are debonded by pickling in acetone. The interface surfaces of the samples are coated with 10 nm gold sputtered layer as seen in Fig. 5.2. The sides of the cut trenches are investigated by SEM for wire saw process related surface damage.

[1] Millennium model wire saw machine produced by Diamond Wire Technology in Colorado, Springs.

[2] Product of Chadwick-Helmuth Inc., California.

[3] Product of Synthetic Lubricants, Inc.

The surface damage depth is measured by processing the SEM images using the image-analysis toolbox of Matlab.

### 5.1.2. Results and Discussion

The results of BIS will be presented in this section. The extent of the surface damage, $D_d$, is shown in Fig. 5.3 as the craves generated by dislodgement of an entire grain due to grain-boundary cracking. The variation of the intrinsic process parameters (normalized wire bow angle, $\alpha/L_o$, and wire loading per unit length, $w$, and surface damage depth, $D_d$, with the change of explored process control parameters are presented in the next sections.

#### 5.1.2.1. Variation of the Intrinsic Process Parameters

The variation of the intrinsic process parameters (which have been previously presented in Chapter 2) with the process control parameters ($V_x$, $V_z$, and T) are summarized again here for the set of samples utilized in the current BIS experiment. The test results are in agreement with the previously observed trends, wherein the normalized wire bow angle, $\alpha/L_o$, decreases as $V_x$ increases (Fig. 5.4a), which results in reduction of the wire loading per unit length, $w$, at constant tension (Fig. 5.4b). However, as the down feed, $V_z$, increases, the wire bow angle and the corresponding loading on the sample increases, as shown in Fig. 5. The role of the wire tension is shown in Fig. 6. Increasing the wire tension would increase the effective stiffness of the wire, and, thereby, the wire bow angle, $\alpha/L_o$, would decrease as shown in Fig. 5.6(a). However, $T$ has a compounding effect on $w$ ($w = 2T \sin \alpha / L_o$); therefore, Fig. 5.6(b) shows an initial drop of $w$ and then saturation as $T$ increases.

#### 5.1.2.2. Variation of the Surface Damage Depth

The surface damage depth, $D_d$, is expected to follow the trend of the imported force on the sample. Figs. 5.7-8-9 show such a trend. $D_d$ decreases with increasing $V_x$ due to the reduction of the cutting feed per individual abrasive grit (Fig. 5.7). As expected, $D_d$, increases with $V_z$ due to the increase in the effective feed/grit (Fig. 5.8). The interesting result is that the wire tension showed no effect on the extent of $D_d$ (Fig. 5.9). Such a result is very

significant when trying to minimize other damage modes, such as the long surface waviness discussed in Chapter 4.

### 5.1.3. General Trend

The experimental results show that the surface-damage depth decreases with increasing wire speed, increases with increasing feed speed, and is independent of tension. These results have the same trend of the surface roughness test results, presented in Chapter 3. The measured surface-damage depth, $D_d$, is thus equivalent to the reported surface roughness. Recalling the damage model discussed in Chapter 3, the surface damage depth, $D_d$, has a similar functional dependence of Eq. 3.6 on the process parameters as seen in Eq. 5.1. The proportionality constant, $\eta$, is introduced to achieve equality as in Eq. 5.2 and calibrated by fitting to a single experimental data point. In order to present the results in nondimensional form, a normalization parameter is defined in Eq. 5.3. A nondimensional damage index, $I_d$, is defined in Eq. 5.4, which is used to obtain the experimental values of the damage index. Eq. 5.5, which defines the dependence of damage index to process parameters, is obtained using Eq. 5.2, Eq. 5.3, and Eq. 5.4. The experimental results of the damage index obtained from Eq. 5.4 and the model estimation of Eq. 5.5 are presented in Fig. 5.10.

$$D_d \approx \left[\frac{\sigma_y R L_g}{K_c}\right]^{\frac{2}{3}} \left[\frac{V_z}{V_x}\right]^{\frac{2}{3}} \tag{5.1}$$

$$D_d = \eta \left[\frac{\sigma_y R L_g}{K_c}\right]^{\frac{2}{3}} \left[\frac{V_z}{V_x}\right]^{\frac{2}{3}} \tag{5.2}$$

$$D_n = \left[\frac{\sigma_y R L_g}{K_c}\right]^{\frac{2}{3}} \tag{5.3}$$

$$I_d = \frac{D_d}{D_n} \tag{5.4}$$

$$I_d = \eta\left[\frac{V_z}{V_x}\right]^{\frac{2}{3}} \tag{5.5}$$

As it has been shown earlier in Chapter 3, the velocity ratio is a key parameter for reducing the surface damage. In order to increase the efficiency of the process without increasing the damage, $V_z$ and $V_x$ should be increased proportionally such that their ratio remains unchanged. Tension does not affect the surface-damage depth.

## 5.2. Design Space Exploration

In many industries, including microelectronics, photovoltaics, and transducers, there is a strong demand to achieve the best possible surface quality, while reducing further processing and ingot waste. In order to achieve this demand, models that relate the process parameters to process-induced damage are of interest. In this study, roughness damage models that relate the process parameters with the surface roughness are developed. Also, a waviness-damage model that explains the evolution of long waviness with process parameters is derived. The models are verified with experimental results. In this section, the results of derived models will be distilled to explore the design space for minimal process-induced damage.

The increase of feed speed increases surface roughness, while increases in wire speed decrease surface roughness. The surface roughness can best be associated with feed speed-to-wire speed ratio. As feed speed-to-wire speed ratio increases, surface roughness increases as presented in Fig. 5.11. In order to increase the efficiency of the process without increasing the surface roughness, the wire speed should be increased proportionally with feed speed. The surface roughness is independent of wire tension.

The amplitude of long waviness increases with increasing feed speed, while the increase of wire tension decreases the long waviness amplitude as seen in Fig. 5.12.

The overall design space is presented in the flow chart in Fig. 5.13. The effect of process parameters on the process outputs, which are process-related damage, is presented in a global view.

## 5.3. References

[1] C.W. Hardin, J. Qu, A.J. Shih, Fixed abrasive diamond wire saw slicing of single-crystal silicon carbide wafers, Materials and Manufacturing Processes, 19 (2) (2004) 355-367.
[2] H.H.K. Xu, Jahanmir S., Microfracture and material removal in scratching of alumina, Journal of Materials Science, 30 (1995), 2235-2247.

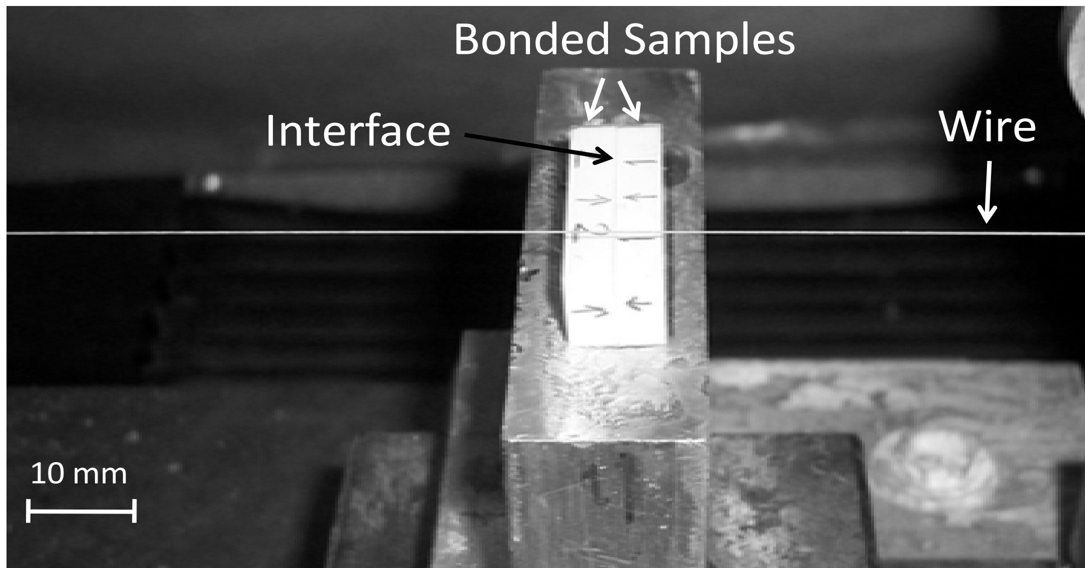


Fig. 5.1. Bonded-interface section wire saw test setup.

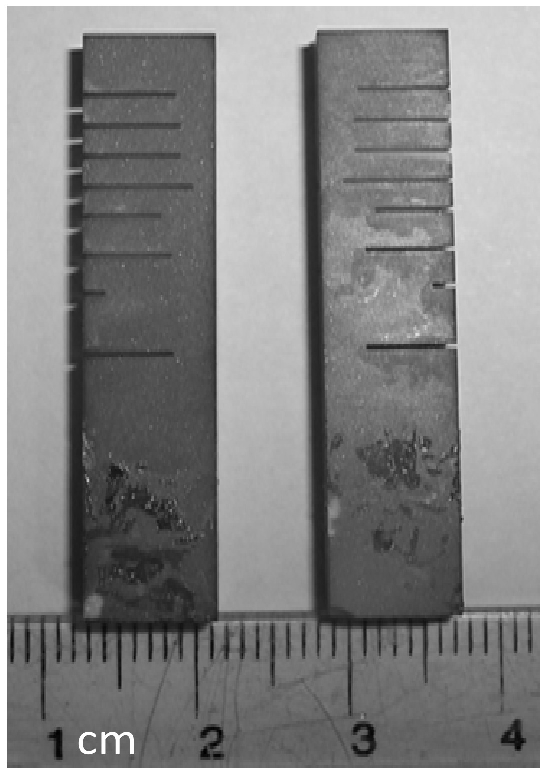


Fig. 5.2. Bonded-interface section test samples coated with gold sputtering for SEM imaging.

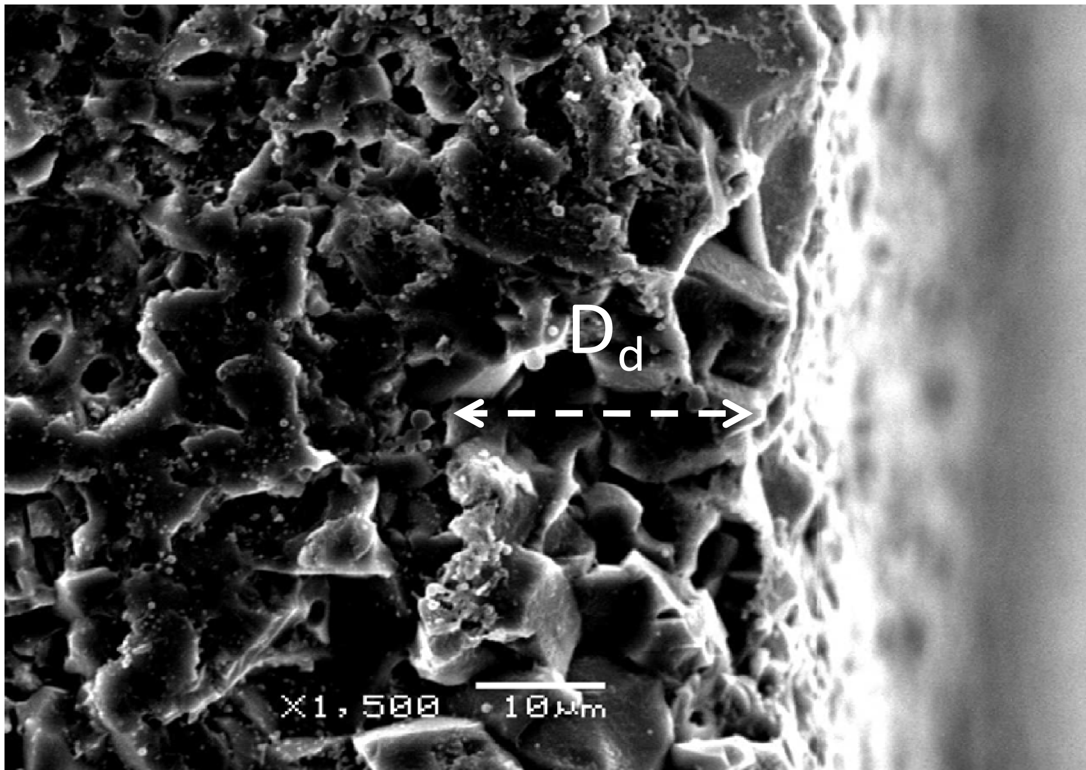


Fig. 5.3. SEM image showing surface damage depth of bonded-interface section (BIS) wire saw test ($V_x$ = 2 m/s, $V_z$= 6.4 μm/sec, $T$=18 N).

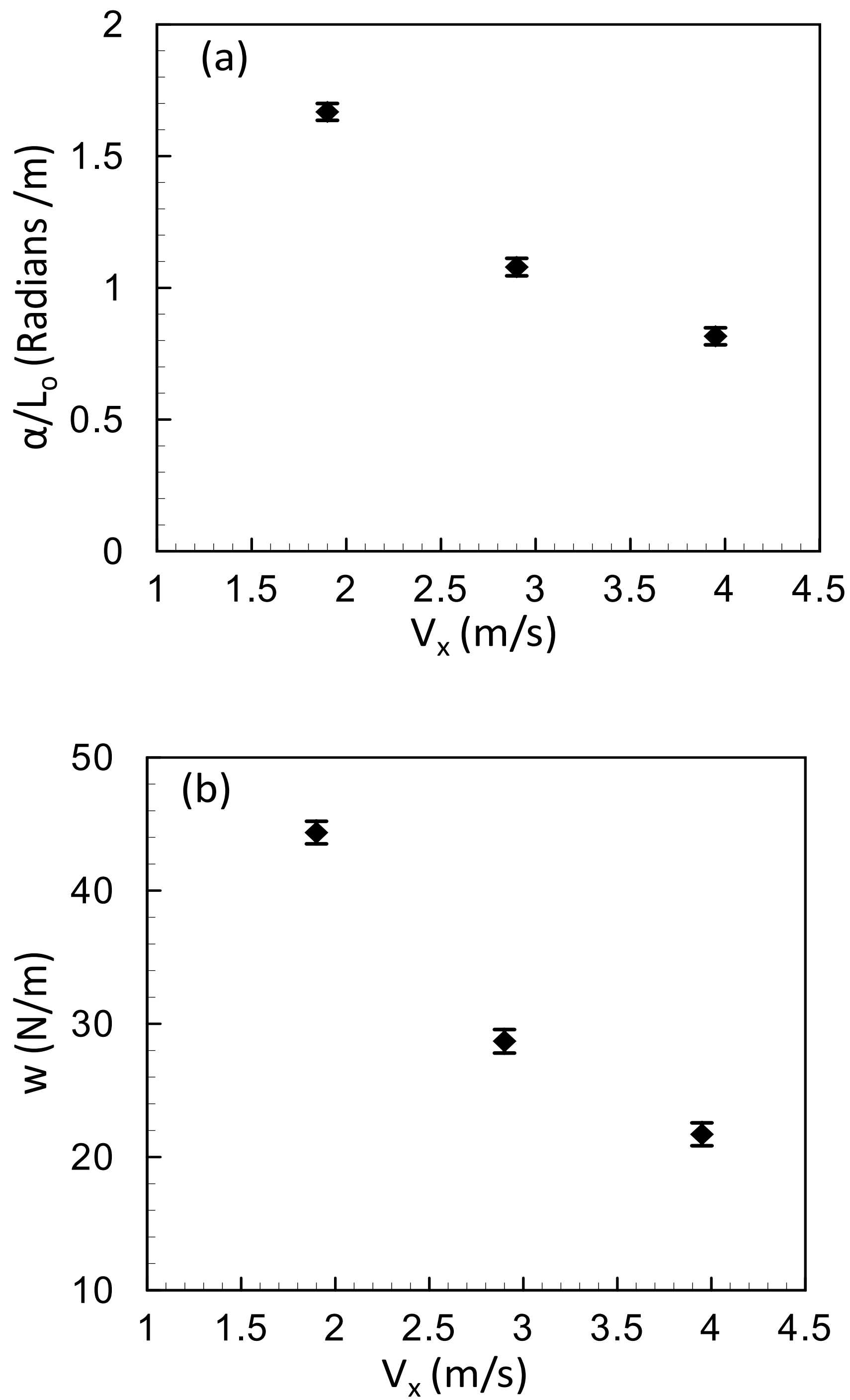


Fig. 5.4. Variation of wire (a) bow angle ($\alpha/L_o$) and (b) wire loading $w$, as a function of wire speed $V_x$ for BIS tests ($V_z$= 6.4 μm/sec, $T$=13 N).

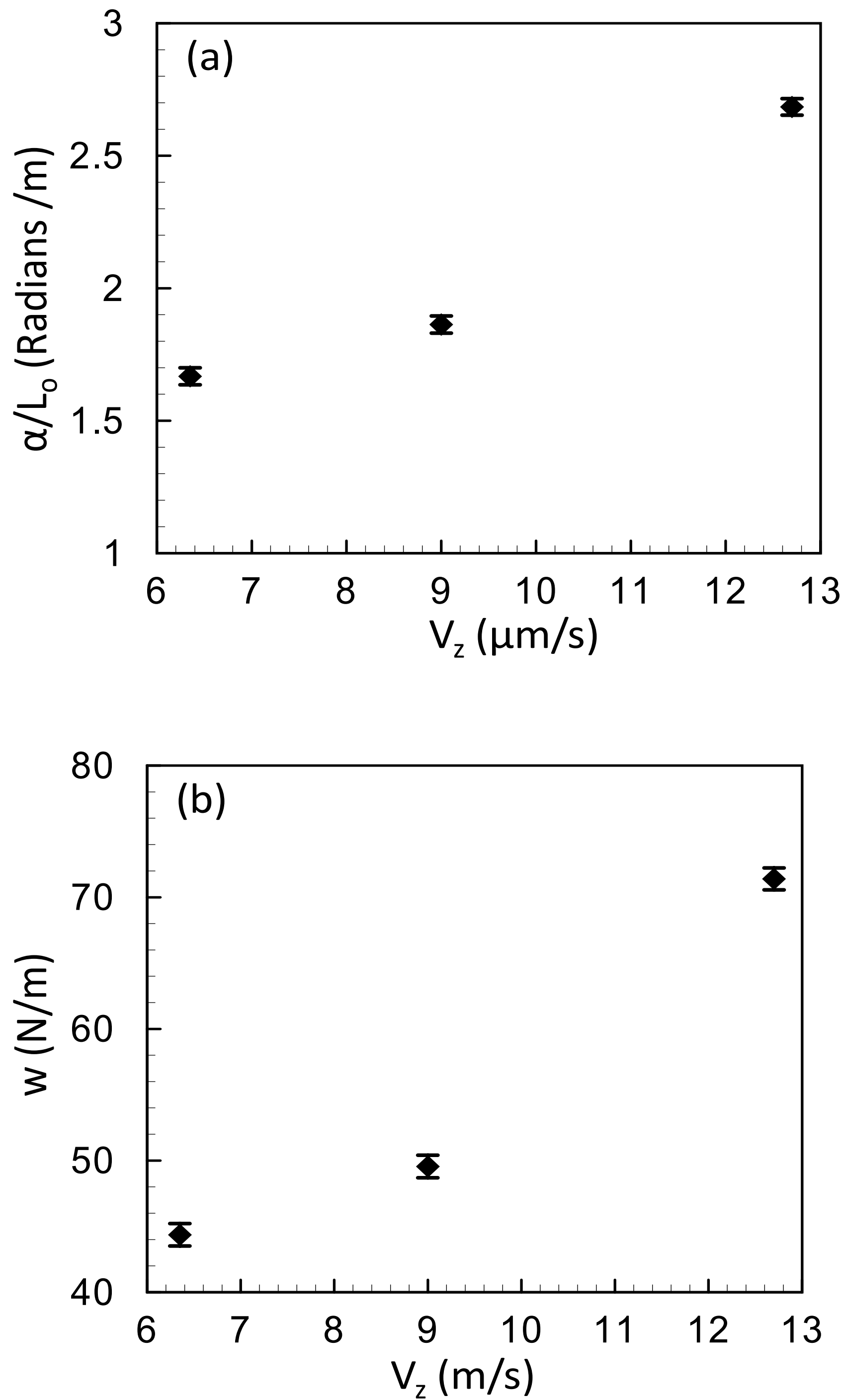


Fig. 5.5. Variation of wire (a) bow angle ($\alpha/L_o$) and (b) wire loading $w$, as a function of feed speed $V_z$ for BIS tests ($V_x$= 2 m/sec, $T$=13 N).

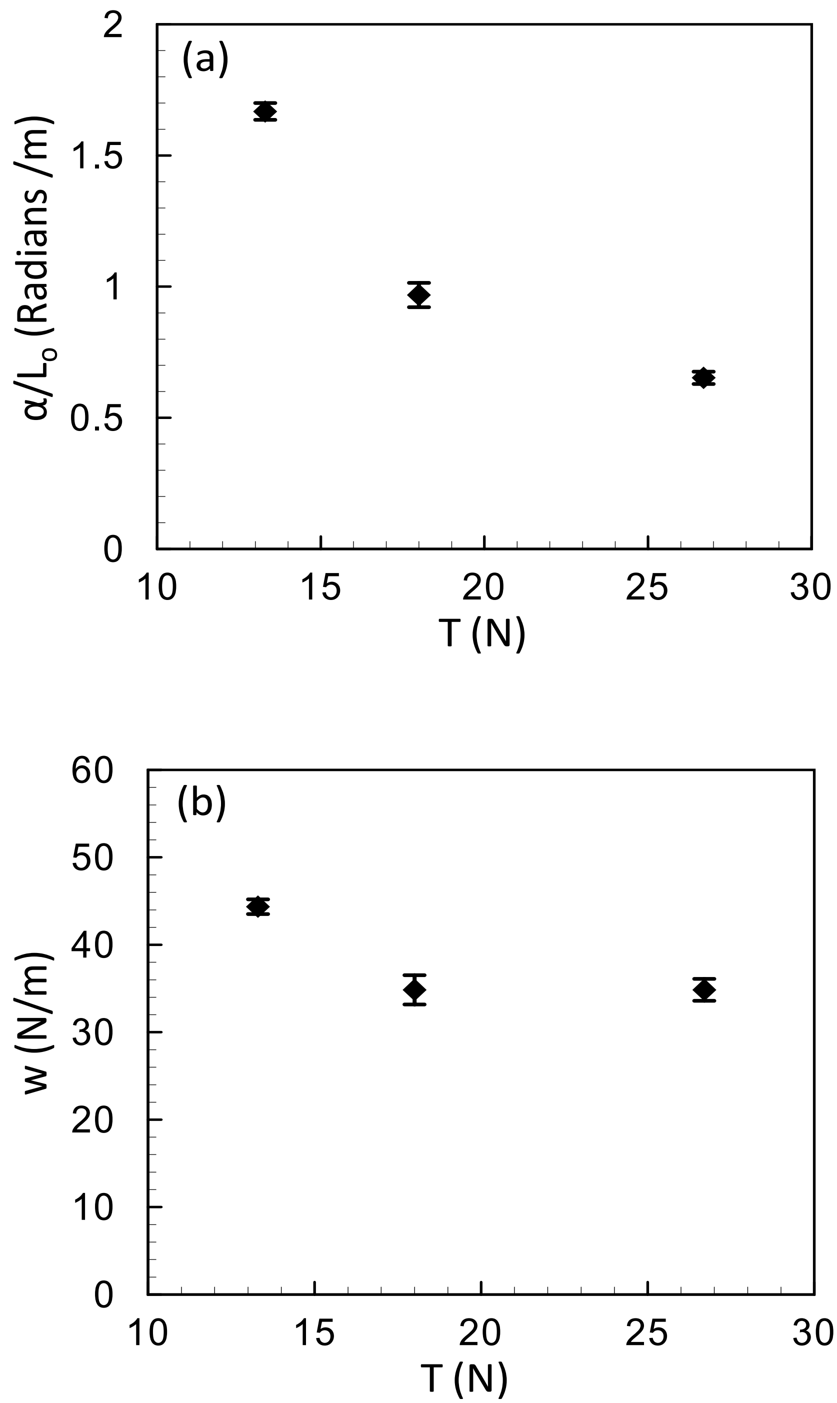


Fig. 5.6. Variation of wire (a) bow angle ($\alpha/L_o$) and (b) wire loading $w$, as a function of wire tension $T$ for BIS tests ($V_x$= 2 m/sec, $V_z$= 6.4 μm/sec).

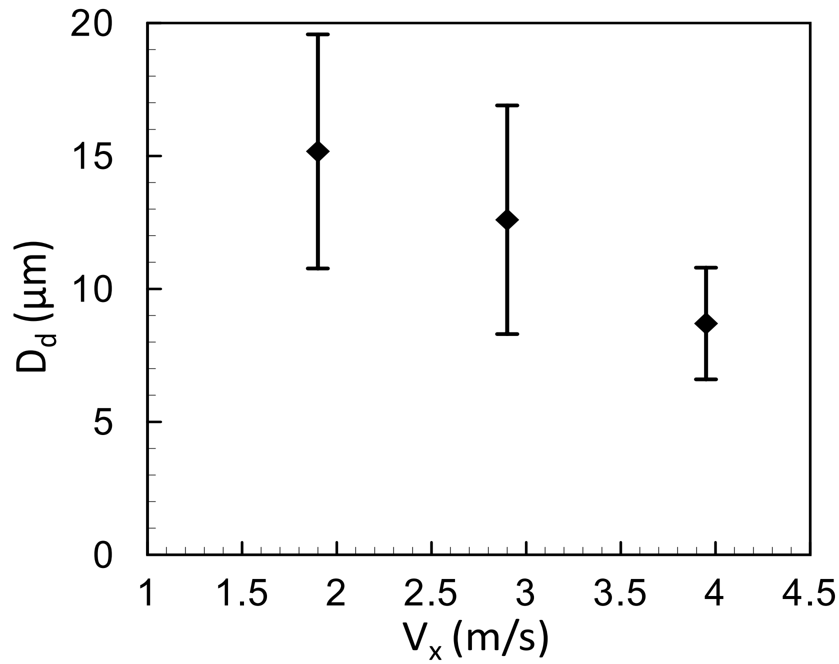


Fig. 5.7. Variation of surface damage depth $D_d$ as a function of wire speed $V_x$ for BIS tests ($V_z$= 6.4 μm/sec, $T$=13 N).

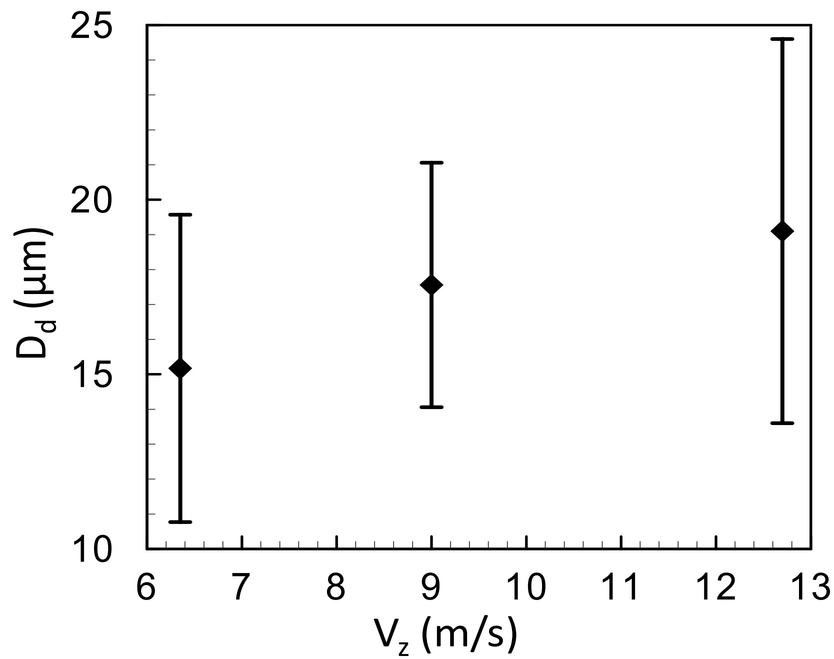


Fig. 5.8. The surface damage depth $D_d$ as a function of feed speed $V_z$ for BIS tests ($V_x$= 2 m/sec, $T$=13 N).

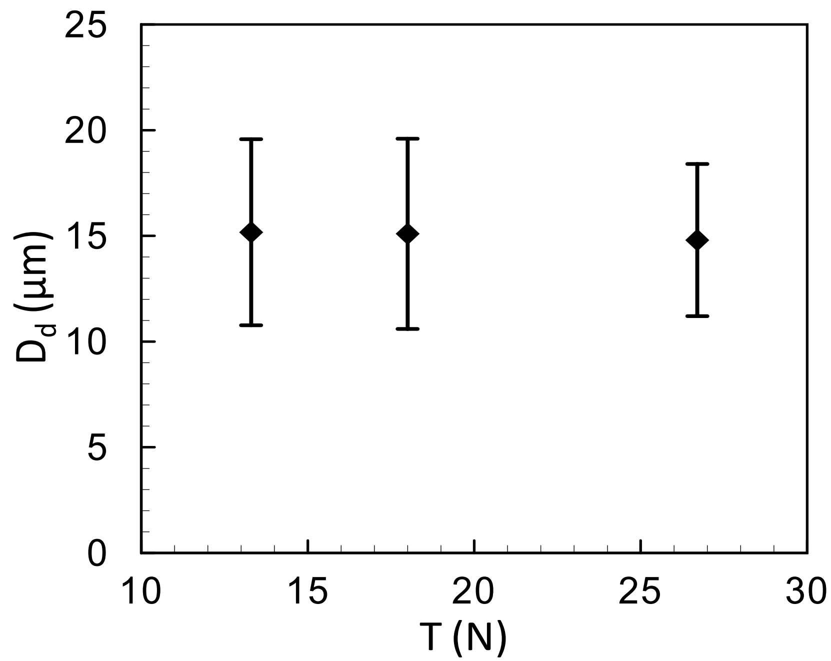


Fig. 5.9. Variation of surface damage depth $D_d$ as a function of wire tension $T$ for BIS tests ($V_x$= 2 m/sec, $V_z$= 6.4 μm/sec).

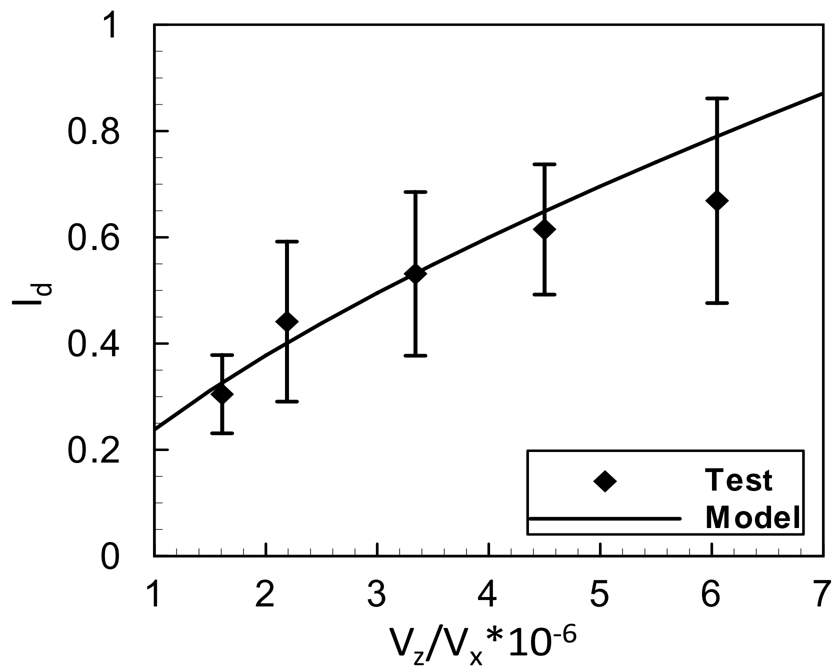


Fig. 5.10. The variation of damage index $I_d$ as a function of $V_z/V_x$ for BIS tests (T= 13 N).

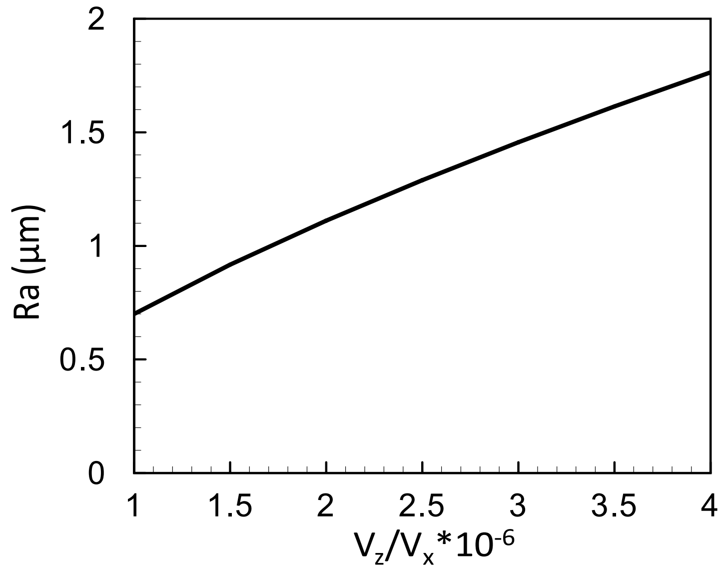


Fig. 5.11. The variation of surface roughness as a function of feed speed to wire speed ratio.

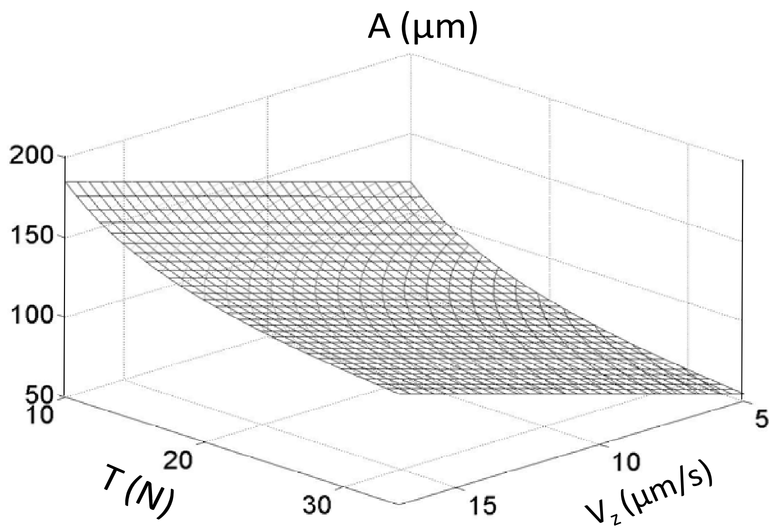


Fig. 5.12. The variation of long waviness amplitude as a function of feed speed and wire tension.

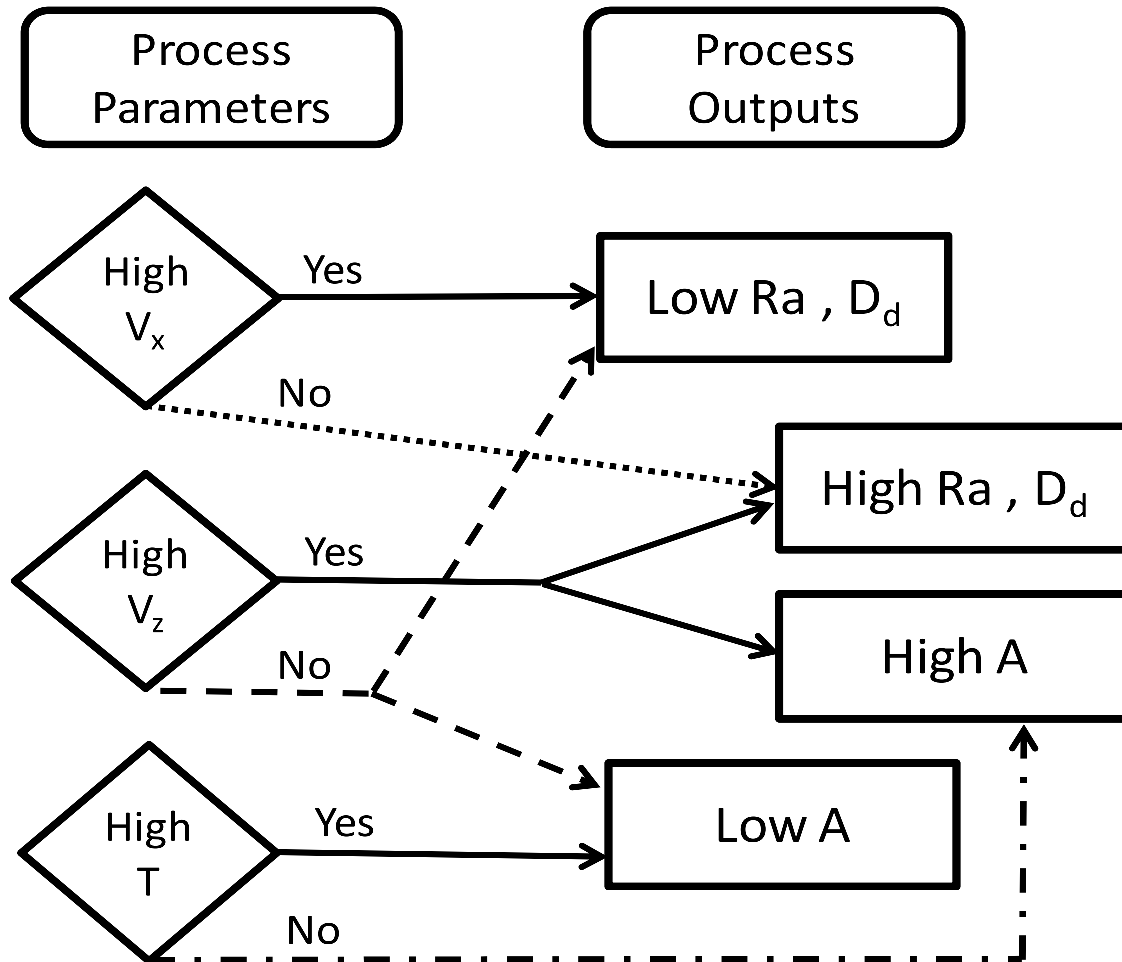


Fig. 5.13. Design space for wire saw process: Effects of wire speed, feed speed and wire tension on surface roughness *Ra*, surface damage depth $D_d$ and long waviness amplitude *A*.

Table 5.1. Bonded-interface section wire saw tests parameters and measured surface damage depth.

| | $V_x$ m/sec | $V_z$ μm/sec | Tension N | Vz/Vx*10^-6 | Dd μm | STD Dd μm |
|---|---|---|---|---|---|---|
| TC32 | 1.9 | 6.4 | 13.3 | 3.3 | 15.2 | 4.4 |
| TC33 | 2.9 | 6.4 | 13.3 | 2.2 | 12.6 | 4.3 |
| TC34 | 4.0 | 6.4 | 13.3 | 1.6 | 8.7 | 2.1 |
| TC35 | 2.1 | 12.7 | 13.3 | 6.0 | 19.1 | 5.5 |
| TC36 | 2.0 | 6.4 | 18.0 | 3.2 | 15.1 | 4.5 |
| TC37 | 2.0 | 6.4 | 26.7 | 3.2 | 14.8 | 3.6 |
| TC38 | 2.0 | 9.0 | 13.3 | 4.5 | 17.6 | 3.5 |

# CHAPTER 6. CONCLUSIONS and FUTURE WORK

## 6.1. Conclusions

The wire saw process is widely used to slice many ceramic crystals that are utilized in a wide range of engineering applications, from silicon wafers in the microelectronics and photovoltaic industries to piezo-crystals for actuators and sensors applications. The process has a higher yield, lower kerf loss, and lower surface damage in comparison to inner diameter saws. The wire saw process allows higher diameter and thinner wafer cutting. The process is also used in cutting almost all brittle materials including ultra-hard carbides, high density or foam ceramics, glasses, sapphire, and rocks. Cutting wood with wire saws is also a potential area that has been introduced in research.

In this work, parametric experimental study is conducted on a model wire saw to correlate the process parameters to quality of the machined surface. An automated single wire saw machine that can allow the variation of the down feed speed, wire speed, and wire tension is utilized. Detailed analysis of the cut-surface topology is carried out using a surface profilometer and SEM imaging. The detailed parametric study is rationalized in several models that describe the relation between the process parameters and the process induced surface damage. The developed correlation is used to explore the limits of the design space and aid in planning and optimization of the process performance.

The SEM surface analysis of bonded interface samples as well as the cut surfaces showed that the material removal is in ductile mode, while there is brittle fracture in the form of grain removal. Stress based and fracture mechanics based damage models are derived for roughness damage induced by the wire saw process. Both models compare well with the experimental trend. It is found that the surface damage is controlled by two ratios. The first is the velocity ratio ($V_z/V_x$), and the second is the yield stress to fracture stress multiplied by grit spacing and radius $D_n=(\sigma_y.R.L_g/K_c)^{2/3}$. Surface roughness is proportional to both ratios. It is found that the major parameter that affects the surface quality is the wire speed, $V_x$. The increase of the wire speed will reduce the effective feed/abrasive grit and, thereby, reduce the

surface damage. Increasing feed speed will increase the surface roughness. A higher feed speed and, thereby, improved material removal rate can be achieved if the wire speed can be increased to keep the velocity ratio constant. It is found that the wire tension has no effect on the surface and subsurface damage.

The role of abrasive diameter and loading is further investigated by examining the performance of three different wires with different grit size and spacing as a function of the process parameters by conducting four tests with each wire. The abrasive grit radius and spacing are measured from SEM imaging of the wires. The experimental results showed that the roughness damage increases with increasing grit radius and spacing, and the roughness damage models are verified. The wire properties have a marked effect on the roughness damage. Wires with smaller grit radius and spacing will lead to smaller roughness damage. High-grit density wires with small grits are beneficial for surface quality.

For the long-wavelength waviness, the process is described based on the competing cutting energy on the specimen and the wire elastic strain energy, employing a string model representation for the wire. It is found that the long-wavelength waviness is bounded by the competition between the oblique cutting energy and the stored elastic strain energy of the wire. By controlling the relative magnitude of each of the these two energy buckets in relation to the stored strain energy of a free standing wire as the limiting case, a reasonable control on the surface waviness can be attained. When the work done by oblique cutting forces is bounded by the work done by the free standing wire, a large peak-to-valley amplitude would arise with big step-like surface features. On the other hand, if the work done by oblique cutting forces is bounded by the work done by wire tension, a wavy surface having a lower peak-to-valley value will arise.

The experimentally observed long waviness formation is explained with these energetic terms that define the mechanisms leading to different surface profiles. The defined mechanisms are used to explain the evolution of the surface profile and peak-to-valley value with respect to process parameters. The increase of wire tension will lead to a wavy surface with a lower peak-to-valley value, while decreasing wire tension will lead to a step-like surface with a high peak-to-valley value. The increase of feed speed will lead to a high peak-to-valley value. The increase of peak-to-valley value will lead to more post grinding and

polishing of the cut surface and increases in expenses. In order to increase the efficiency without increasing the peak-to-valley value, the wire tension can be increased proportional to feed speed.

## 6.2. Future Work

The dissertation focused on the wire-saw process induced surface roughness and a long waviness investigation. Experimental and analytical research is conducted to model the wire saw process induced damages. During the experiments, one of the main problems is the frequent wire breakage. In a lab type wire-saw machine, where there is only one wire running, the wire breakage leads to considerable loss of time until a new wire is winded and the set up is rearranged for a new test. In industrial applications, where several hundred wires are running in parallel, wire breakage will cause an important down time, which will increase costs. When the expensive wire is broken it generally cannot be used and has to be disposed. Moreover, the wire breakage can cause undesirable wafer breakage or, at least, scratches on the wafer surface. The wire in the saw process is under fatigue loading while running around the small diameter guide pulleys, in bending mode of loading. The wire tension is already on the order of wire tensile strength, which makes the fatigue loading detrimental. The multi-layer wire technology provides protection to the steel core, while propagation of fatigue cracks from coating to core is inevitable. Affixing abrasive grits creates initial defects that may propagate and cause failure during cutting. Future research can be done to improve the strength and durability of the fixed-abrasive wires.

Heat generation during the wire saw cutting can be harmful for the slender wafers. The effects of heat generated during the wire saw process and mitigation of the diverse effects of the heat can be studied experimentally using real-time temperature monitoring of wafer cutting experiments. Process design concepts can be improved to overcome the heating effects.